DELFT UNIVERSITY OF TECHNOLOGY

The Effect of Climate Variability on the Root Zone Storage Capacity

RESEARCH INTO THE EFFECT OF CLIMATE VARIABILITY ON THE ROOT ZONE STORAGE CAPACITY WITH A FOCUS ON THE MEUSE BASIN

BY

NIENKE TEMPEL

Student number:	4589556
Date:	April 13, 2023

Thesis committee:	Dr. Markus Hrachowitz	TU Delft
	Dr. Riccardo Taormina	TU Delft
	Eric Sprokkereef	Rijkswaterstaat
	Jasper Stam	Rijkswaterstaat
	Dr. Laurène Bouaziz	Deltares

TUDelft

Rijkswaterstaat
Ministerie van Infrastructuur en Milieu

The effect of climate variability on the root zone storage capacity

Nienke Tempel
Delft University of Technology

April 2023

Abstract

Hydrological models are commonly used to predict future streamflow. However, the assumption of stationary model parameters obtained through calibration on past conditions may not accurately represent non-stationarity in hydrological system characteristics. Evidence suggests that vegetation adapts its root zone storage capacity in response to changing climate, emphasizing the need to account for non-stationarity in hydrological models. This study examines the effects of long-term climate variability on root zone storage capacity and its consequences on hydrological response. By using the method of Fu (1981), we determine whether the root zone storage capacity has significantly changed and evaluate the sensitivity of hydrological model predictions to these changes. We explain the changes in root zone storage capacity and evaporation using various climate indicators. For two large sample datasets CAMELS GB and CAMELS USA, we confirm that the Fu method can be used with the same omega parameter when transitioning from one decade to the next, indicating small differences in root zone storage capacity. However, for hydrometeorological data from the Meuse basin in Northwest Europe, we observe a trend where the actual evaporation is smaller than expected. This suggests that caution should be exercised when applying the Fu-method. In four different scenarios, we have implemented historical changes in evaporation as altered root zone storage capacity in the wflow_flextopo model. The scenarios based on the evaporation trends observed in the Meuse data, result in less evaporation during the summer months (May, June, July) within a range of 0 to -22%, and an increase in streamflow during the autumn months (September, October, November) between 0 and +48%. On the other hand, the scenarios based on evaporation trends observed in all combined data (Meuse, CAMELS GB, CAMELS USA) result in changes around zero of evaporation during summer months between -7% and +5%, and of streamflow in autumn months between -11% and +10%. This study represents a step towards a more reliable and robust estimation of root zone storage capacity in hydrological modelling, thereby enhancing our ability to predict future streamflow.

1 Introduction

Vegetation continuously adapts to climatic and environmental changes to ensure sufficient and continuous access to water in order to overcome drought periods (Gao et al., 2014; de Boer-Euser et al., 2016). One of the processes involved is the adaptation of root systems as these determine the soil pore volume that is accessible for plants to extract water for transpiration. The accessible water is stored in the ground up to a maximum amount of root zone storage capacity $S_{r,max}$. This variable is important as it controls the partitioning of water into evaporative fluxes and drainage (Savenije and Hrachowitz, 2017). The root zone storage capacity $S_{r,max}$ is impossible to observe directly at the catchment scale and therefore is typically treated as a calibration parameter in hydrological models or obtained from known soil characteristics combined with estimates of the depths of the roots (Nijzink et al., 2016).

Hydrological models can be used to predict future streamflow. Future projections in combination with parameters for current-day conditions are often used, as there is little information on the future properties of the system (Parajka et al., 2015; Van Noppen, 2022). This means that despite the strong awareness of non-stationarity in hydrological system characteristics, model parameters are obtained through calibration on past conditions and assumed stationary (Ponds, 2022; Nijzink et al., 2016). The impact on simulated runoff of assuming time-invariant parameters can be very significant (Merz et al., 2011). To illustrate this, Merz et al. (2011) calibrated different parameters for a conceptual rainfall-runoff model for six consecutive 5-year periods over catchments in Austria. Different parameters show clear time trends if calibrated to different periods. There is an increasing trend for soil moisture storage, which can be related to an increase

in air temperature and potential evaporation.

For the root zone storage capacity, it is also common practice to calibrate hydrological models with the use of observed historical climate conditions, assuming parameters to remain constant in time, in contradiction to the root system that is actively adapting (Nijzink et al., 2016; Parajka et al., 2015). The consequences are uncertainties in modelled predictions of hydrological response (Bouaziz et al., 2021). To increase the reliability of long-term hydrological predictions, a time-variable model parameter describing the adaptation of root zone storage capacity to a changing environment is needed. Another way to reliably and directly estimate the root zone storage capacity is from long-term water balance data (de Boer-Euser et al., 2016; Bouaziz et al., 2022). The water balance or climate-based method derives the root zone storage capacity from the maximum annual water deficits that result from the difference between the cumulative daily precipitation and transpiration (Gao et al., 2014; Nijzink et al., 2016). In the determination of root zone storage capacity, it may initially appear reasonable to conduct ground-based measurements and assess the composition of soil in order to determine its value. However, natural heterogeneity can pose significant challenges to such an approach (Savenije and Hrachowitz, 2017). As noted by de Boer-Euser et al. (2016), climate-derived root zone storage capacities have greater explanatory power than those derived from the soil.

Catchment characteristics that are associated with root zone storage capacity include the aridity index, inter-storm duration, seasonality, and runoff ratio (Gao et al., 2014). Van Voorst (2020) demonstrated that the variance in root zone storage capacities between Canadian catchments can be described by a combination of long-term average variables such as the aridity index and runoff coefficient, and the coherence of seasonal and timing effects, as indicated by the seasonality timing index. The aridity index and runoff coefficient provide insights into the allocation of water for transpiration within a catchment, whereas the seasonality timing index explains the seasonal distribution of this water.

Previous research (Bouaziz et al., 2022; Van Noppen, 2022) used 2K global warming scenarios to look into the expected changes in the root zone storage capacity in the study area of the Meuse. 2K global warming scenarios are climate simulations that project how the Earth's climate could change in response to a global average temperature increase of 2 degrees Celsius above pre-industrial levels. The water balance method applied to a 2K global warming climate resulted in both studies in a larger root zone storage capacity. This larger root zone storage capacity results in strong seasonal changes in the hydrological response. Although this previous research has simulated the effects of global warming on the root zone storage capacity in the Meuse study area, it is important to note that these studies have not examined historical data to investigate changes in root zone storage capacity. These simulations of future climate change have demonstrated that global warming leads to an increase in root zone storage capacity. However, further research is needed to explore the extent to which changes in root zone storage capacity have occurred in response to historical climate variability. This study aims to address this gap in the literature by examining historical data on root zone storage capacity in both the Meuse study area and other available large sample datasets, and quantifying the potential impacts of changing root zone storage capacity on hydrological response. We also examine whether the changes can be explained by climate indicators. A change point analysis conducted by Tu et al. (2005) revealed that climate variability, rather than land use change, was the primary driver behind the increase in flood frequency observed in the Meuse basin. However, the research conducted by Fenicia et al. (2009) suggests that changes in land use may also have played a role.

The main aim of this research is to quantify the effect of long-term climate variability on the root zone storage capacity and resulting consequences on the hydrological response. We test the hypothesis that historically the root zone storage capacity has changed and caused significant changes in stream-

flow. In order to determine this, we need to (I) test if past climatic variability has resulted in changes in root zone storage capacity at decadal time scales (II) quantify differences in the sensitivity of changes in root zone storage capacity to climate characteristics, and (III) determine the consequences thereof on the hydrological response.

Initially, we calculate changes in the long-term hydrological distribution of evaporation and runoff utilizing the Budyko approach for both the Meuse data and large sample datasets. Then we try to explain the changes with climate indicators. Finally the changes in the evaporation are used in a process-based model to quantify the effect on the streamflow for the Meuse basin.

2 Study area

This study focuses on the Meuse river basin upstream of Borgharen (at the border between Belgium and the Netherlands), which spans an area of 21,300 km^2 in the northwest of Europe. Approximately 60% of the basin is used for agriculture, while 30% is covered by forests (Bouaziz et al., 2022). See Figure 1 for (a) the location of the basin in Europe and (b) the elevation range of in the basin.

The basin comprises different geological zones with distinct landscapes and rock types. Lorraine Meuse has wide floodplains and hilly landscapes composed of sedimentary consolidated rocks. Ardennes Meuse is characterised by narrow, steep valleys and metamorphic rocks, and relatively thin, impermeable soils. Dutch and Flemish Lowland is composed of unconsolidated rocks with wide floodplains and a low river gradient (De Wit et al., 2007; Bouaziz et al., 2022).

The Meuse is located in an area with the characteristics of a temperate climate. The Meuse is a rain-fed river with a response time of a couple of hours up to a few days. Snow has little impact on the streamflow, although it can be of significant importance in specific events (de Boer-Euser, 2017).

The streamflow has strong seasonality, with low summer flow and high winter flow, which is on average four times higher than the summer flow (De Wit et al., 2007). Precipitation is relatively constant throughout the year, so the seasonality of the streamflow is mainly caused by the seasonal differences of potential evaporation. The average annual precipitation, potential evaporation, and streamflow are respectively approximately 923 mm yr^{-1}, 610 mm yr^{-1}, and 402 mm yr^{-1}, as calculated from the data which will be discussed in Section 3.1.

3 Data

To provide a more comprehensive analysis of the effects of climate variability, we have analyzed not only the Meuse basin data but also large sample datasets. However, given that the data have been collected using different methods and merged in different ways, we have taken care to keep the results of different datasets separate. This is particularly important because the different datasets may have distinct drivers of changes in root zone storage capacity, which need to be observed separately. By doing so, we can gain a more nuanced understanding of the factors that contribute to changes in evaporation and root zone storage and ensure the reliability of our findings.

3.1 Meuse data

3.1.1 Observed historical climate data

The Meuse climate data have undergone preprocessing by Bouaziz et al. (2022) using the European daily high-resolution gridded dataset, E-OBS (v20.0) (Cornes et al., 2018). This dataset comprises historical climate data, including daily precipitation, temperature, and radiation fields, from 1980 to 2018 at a 25 km^2 resolution. The data were collected from station data compiled by the European Climate Assessment & Dataset (ECA&D) initiative. To downscale temperature, a digital elevation model and a fixed lapse rate of 0.0065 °Cm^{-1} were utilised, while potential evaporation was estimated using the Makkink method (Hooghart and Lablans, 1988). However, a
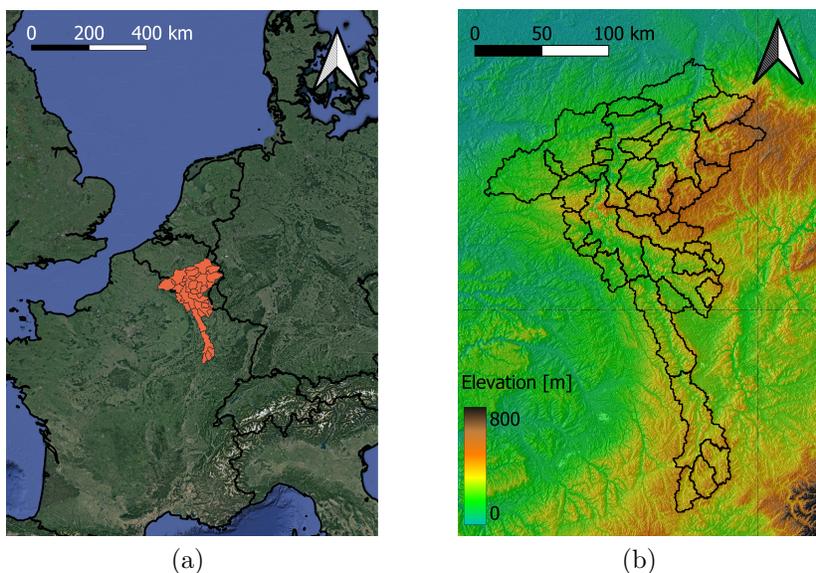
Figure 1: (a) The location of the Meuse basin in Europe, (b) The elevation range in the basin Meuse basin.

significant underestimation of precipitation (>20%) was observed when comparing to data provided by the Service Public de Wallonie (Bouaziz et al., 2020, 2022). To address this issue, a monthly bias correction factor is applied to the E-OBS precipitation in the center of the basin, resulting in a better representation of local precipitation data. The corrected dataset was used in subsequent analyses.

3.1.2 Streamflow

The time series data for streamflow in Belgium including Borgharen is readily accessible for the years 1999 to 2018 (SPW, 2018) (Rijkswaterstaat, 2022). The time series data for streamflow in France is available for the period from 1989 to 2018 (Ministère de l'Ecologie, du Développement Durable et de l'Energie, Banque Hydro). It is important to note that the streamflow data for Borgharen is not a direct measurement, but rather a constructed time series that combines the measured streamflow at St Pieter on the Meuse and at Kanne on the Albert Canal. This composite time series is used to estimate the total streamflow from the tributaries before some of it is diverted into the Albert Canal (De Wit et al.,

2007; Bouaziz et al., 2022).

3.2 Large sample datasets

The large sample datasets that are used are CAMELS USA and CAMELS GB. CAMELS stands for Catchment Attributes and Meteorology for Large-sample Studies.

3.2.1 CAMELS GB

The CAMELS-GB dataset (Coxon et al., 2020) comprises 671 catchments situated in Great Britain and has been carefully curated using strict criteria to ensure accuracy and reliability. The catchments were chosen from the UK National River Flow Archive (NRFA) Service Level Agreement (SLA) Network, which selects stations based on their hydrometric performance, the representativeness of the catchment, the length of record, and the degree of artificial disturbance to the natural flow regime (Dixon et al., 2013; Hannaford, 2004). The NRFA also subjected the catchments to an
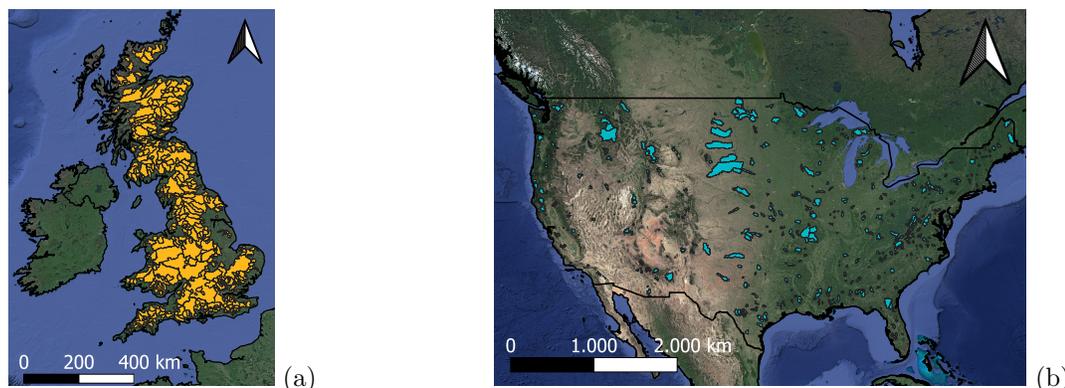
Figure 2: The locations of the catchments that are provided by the large sample datasets (a) CAMELS GB, (b) CAMELS USA.

additional level of validation to ensure the credibility of flows in the extreme ranges and the need to maintain complete time series (Coxon et al., 2020).

Daily meteorological time series are provided from October 1st, 1961 to September 30th, 2015. The following variables were used from these time series: precipitation, temperature, and incoming short-wave radiation. The daily precipitation data was sourced from the CEH Gridded Estimates of Areal Rainfall dataset (CEH-GEAR), which provides gridded estimates at a resolution of 1 km^2, derived from quality-controlled, observed precipitation data from the Met Office UK rain gauge network using natural neighbour interpolation (Keller et al., 2015; Tanguy et al., 2016). The temperature and incoming shortwave radiation data were obtained from the Climate Hydrology and Ecology research Support System meteorology dataset (CHESS-met), which provides daily gridded estimates at a resolution of 1 km^2 (Robinson et al., 2017; Hough and Jones, 1997; Thomson et al., 1981). The temperature was directly downscaled from the MORECS dataset, while the incoming short-wave radiation was calculated from the downscaled temperature, vapor pressure, and sunshine hours. Potential evaporation was estimated using the Penman-Monteith equation for FAO-defined well-watered grass (Allen et al., 1998).

3.2.2   CAMELS USA

The CAMELS USA dataset is a combination of hydro-meteorological time series from Newman et al. (2015) and catchment attributes from Addor et al. (2017). The dataset contains meteorological forcing and observed discharge data for the period between 1980 and 2010. The catchments are a subset of the Geospatial Attributes of Gages for Evaluating Streamflow (GAGES-II) from the United States Geology Survey (USGS) of 2011 (Falcone et al., 2010; Falcone, 2011). To be included, the gauges had to meet the following criteria: be active as of 2009 and have complete flow data for at least 20 years in the period between 1990 and 2009, be a GAGES-II reference gage, have less than 5% imperviousness as measured by the National Land Cover Database (NLCD-2011) (Jin et al., 2013), and pass a survey of human impacts in the basin conducted by local Water Science Center evaluators. In this way, the gauges are expected to best represent natural flow conditions.

The meteorological forcing data includes three datasets: NLDAS, Maurer, and Daymet. For this study, the Daymet dataset was selected because of its daily-gridded data and high spatial resolution of 1 x 1 km, following the work of Van Noppen (2022). The variables used from the dataset are daily maximum

Table 1: Segmentation of datasets by 10-year periods, with exception of the CAMELS USA which has two periods of 9 years. Note the extra time periods for the France Meuse river data, in comparison with the Belgium/Netherlands data.

Dataset	Data period (1st Jan. first year - 31st Dec. last year)				
Meuse Belgium and The Netherlands				1999 - 2008	2009 - 2018
Meuse France			1989 - 1998	1999 - 2008	2009 - 2018
CAMELS GB	1971 - 1980	1981 - 1990	1991 - 2000	2001 - 2010	
CAMELS USA		1981 - 1989	1990 - 1999	2000 - 2009	

and minimum temperature, precipitation, shortwave downward radiation, and day length. To provide the dataset with shortwave incoming radiation, the Mountain Climate Simulator (MT-CLIM) was used. Potential evaporation was estimated using the Priestley-Taylor equation. Observed discharge data were obtained from the USGS Water Information System server for the period between 1980 and 2010 (Newman et al., 2015).

3.3   Data correction

To ensure consistency across the datasets, a data correction was performed on the potential evaporation calculation by Van Noppen (2022). Originally, the CAMELS-USA dataset used the Priestley-Taylor equation to estimate potential evaporation while both the CAMELS-GB dataset and the observed historical E-OBS dataset used the Penman-Monteith and Makkink equations, respectively. In an effort to create more consistency across the datasets, we continue with Noppen's work by using the Makkink equation to compute the potential evaporation for the catchments of the large sample datasets. The Makkink equation uses the mean daily temperature and shortwave incoming radiation (Hooghart and Lablans, 1988). For the CAMELS-USA dataset, the incoming shortwave radiation was estimated using the daily number of sunshine hours (Hiemstra and Sluiter, 2011). However, since the CAMELS-GB dataset did not contain daily sunshine hours, a variation of the Makkink equation was used. For more information, see Appendix A.

3.4   Data segmentation

The datasets are divided into 10-year periods as these are an appropriate length to investigate changes in root zone storage capacity and other key climate variables impacted by climate variability. Please refer to Table 1 for the specific periods covered by each dataset. This approach enables us to observe and analyze changes in these variables over time and gain a better understanding of the effects of climate variability.

4   Methods

In Figure 3, a schematic overview is presented of the various steps undertaken in this research. The first part of the study involves I) estimating historical changes in root zone storage capacities. This is subdivided into step (1) to estimate changes in evaporation, which is discussed in Section 4.1.1. Step (2) is to calculate changes in root zone storage capacity based on these changes in evaporation, which is discussed in Section 4.1.2. The second part of the research involves II) relating changes in evaporative index (ΔEI) to climate indicators. Section 4.2 discusses how the climate indicators are calculated and how it is determined whether the climate characteristics have an impact on the error in EI (ΔEI). Finally, the third part of the study involves III) quantifying the effect of changes on streamflow in the Meuse, as discussed in Section 4.3.

I. Estimate historical changes in root zone storage capacity	II. Relate changes to climate indicators	III. Quantify effect of changes on streamflow in the Meuse
Use the Budyko framework to estimate historical errors from expected evaporation (ΔEI)	Relate the historical errors (ΔEI) to climate indicators and to change in climate indicators	Use the distributions of the errors in EI (ΔEI), to quantify the potential effects on the streamflow

(1a) Determine the average aridity index (AI) and evaporative index (EI) for every decade.

(1b) Calculate ω-value for every decade, using the Fu-equation (see, Eq. 1).

(1c) Calculate expected evaporation based on the ω-value of the previous decade.

(1d) Calculate the error (ΔEI) between the expected and the actual value for EI

(2) Calculate the expected $S_{r,max}$ based on the expected ΔEI and the error in $\Delta S_{r,max}$

$$EI = 1 + AI - (1 + (AI)^{\omega})^{1/\omega} \quad (1)$$

(1) Calculate climate indicators for every catchment, for both the whole time period as for every decade.

(2) Perform multiple linear regression, with ΔEI_t as dependent variable and climate indicators (v) and change in climate indicators (Δv) as explanatory variables.

(3) Divide catchments in
(a) climate indicators grouped over whole period (v)
(b) change in variables calculated for one decade on to the next (Δv).

(4) Perform statistical tests to see if there is a significant difference in ΔEI between different groups

(1) For every scenario, calculate the expected $S_{r,max}$ using the Fu-equation, assuming the error in EI (ΔEI) is zero – this is the reference run.

(2) For every scenario, calculate the expected $S_{r,max}$ using the Fu-equation but now change the expected evaporation based on the historical errors in EI (ΔEI_{Meuse} and ΔEI_{All}).

(3) For every scenario, compare the hydrological response between the reference run and the other runs.

v	Δv	Climate indicator names
AI	ΔAI	Aridity index
P_{annual}	ΔP_{annual}	Mean annual precipitation
$E_{p,annual}$	$\Delta E_{p,annual}$	Mean annual potential evaporation
T	ΔT	Mean temperature
SI	ΔSI	Seasonality index
ST	ΔST	Seasonality timing
Is_dur	Δis_dur	Interstorm duration

Figure 3: Overview of the methodological procedure.

4.1 Changing climate and vegetation

4.1.1 Estimating changes in evaporation

The Budyko relationship (Budyko, 1961) is a water balance of a catchment area based on the balance between precipitation, evaporation, and runoff. The relationship provides insight into how climate, expressed as the aridity index (AI), influences the evaporative index (EI) over the long term.

The Budyko space is bounded by the supply limit, where no more water can evaporate than what is available, and the demand limit, where long-term actual evaporation cannot exceed potential evaporation (Zhang et al., 2004; Budyko, 1961).

Fu (1981) introduced an additional parameter, omega (ω), to reflect the collective impact of climate, topography, soil, and vegetation on the relationship between the aridity index ($\overline{E}_P/\overline{P}$) and the evapo-

rative fraction ($\overline{E}_A/\overline{P}$) versus the runoff fraction ($\overline{Q}/\overline{P} = 1 - \overline{E_A}/\overline{P}$), as the original Budyko relationship does not explicitly consider these influences (Troch et al., 2013; Bouaziz et al., 2022; Ponds, 2022), see Equation 1.

$$\frac{E_A}{P} = 1 - \frac{Q}{P} = 1 + \frac{E_P}{P} - \left(1 + \left(\frac{E_P}{P}\right)^{\omega}\right)^{1/\omega} \quad (1)$$

The evaporative index (EI) and the aridity index (AI) are defined as Equation 2 and 3 respectively. From now these terms will be referred to as EI and AI.

$$EI = \frac{\overline{E_A}}{\overline{P}} \quad (2)$$

$$AI = \frac{\overline{E_P}}{\overline{P}} \quad (3)$$

We have derived Equation 4 by rewriting Equation 1, where we use the abbreviations EI and AI.

$$EI = 1 + AI - (1 + (AI)^{\omega})^{1/\omega} \quad (4)$$

Determining a generalized value for ω remains challenging because of the heterogeneity and interdependency of catchment-specific influences. Consequently, the relationship between changing vegetation dynamics and changed catchment-specific parameters is also assumed to be catchment-specific, meaning that one catchment has a specific value for ω (Jaramillo et al., 2018; Ponds, 2022; Bouaziz et al., 2022).

We can determine the value of omega by solving Equation 1 using observed climate and discharge data. Given that the value of omega is catchment-specific, the Fu-equation is often extrapolated based on historical data to make predictions about the expected distribution of the evaporative fraction and the runoff fraction, assuming no changes in land use (Bouaziz et al., 2022; Ponds, 2022; Zhang et al., 2004). The expected aridity index is then predicted based on climate model projections of temperature and precipitation. So in order to estimate the future value of the evaporative index, the expected aridity index is typically used. However, in this study, we use historical data. So instead of estimating the future value of the aridity index, we make predictions from one decade to another, using the Fu-equation to estimate the expected distribution of the evaporative fraction and the runoff fraction. We use the actual historical aridity index to make these predictions, rather than relying on projected values.

To determine if the amount of evaporation is changing due to climate change, we compare the solution of the Fu-equation for each decade. This involves solving the equation to find omega for each decade, and ΔEI is the difference between the actual EI of the subsequent century compared to the predicted value of the EI based on the omega value from the previous decade. See Figure 4 for a step-by-step approach. The first step (step (a) in Figure 4 and Equation 5) is to solve the Fu-equation for the first time period, $p1$, with historical data. This involves solving Equation 1, where the values for the evaporative index EI and the aridity index AI can be computed to obtain a value for ω.

(a)

(b)

(c)
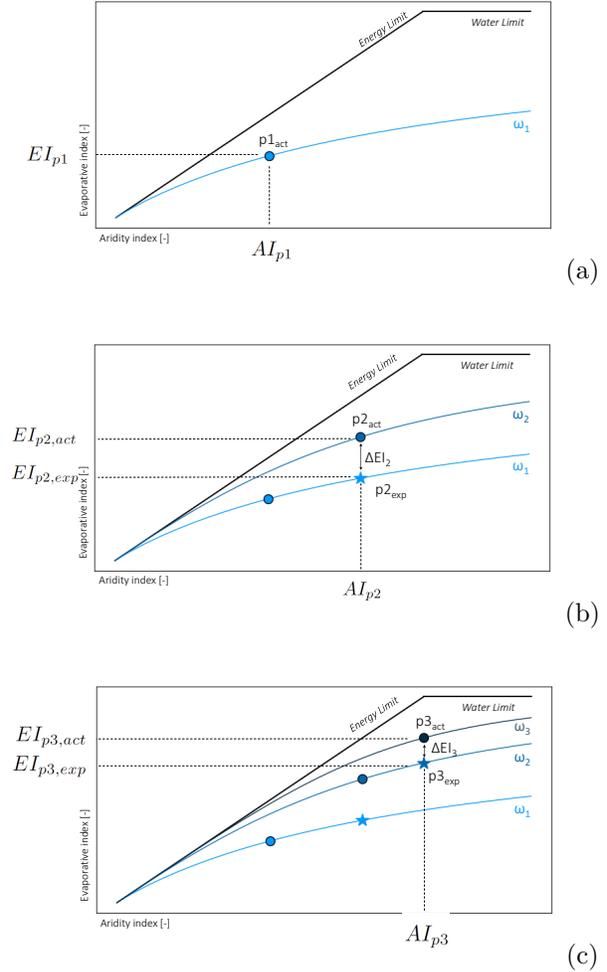
Figure 4: The step-by-step process for calculating the error in EI (ΔEI) using data with three decades as an example. In step (a), the evaporative index (EI) and aridity index (AI) are calculated for the first decade, resulting in $p_{1,act}$ and ω_1. Step (b) involves using ω_1 from $p1$ and the AI of $p2$ to estimate the expected EI and so $p_{2,exp}$, while $p_{2,act}$ represents the actual EI. The difference between $p_{2,exp}$ and $p_{2,act}$ is ΔEI_2. $p_{2,act}$ is used to calculate ω_2. In step (c), ω_2 is used to estimate the expected EI for $p_{3,exp}$ using the AI of p3. By comparing $p_{3,act}$ and $p_{3,exp}$, the value for ΔEI_3 can be determined.

$$EI_{p1} = 1 + AI_{p1} - \left(1 + (AI_{p1})^{\omega 1}\right)^{1/\omega 1} \qquad (5)$$

The next step ((b) in Figure 4 is to solve the equation again with the $(AI)_{p2}$ of the next decade while using the $\omega 1$ value from the previous century, assuming that we remain on the same ω line. The solution of this yields the expected evaporation, $(AI)_{p2,exp}$.

$$EI_{p2,exp} = 1 + AI_{p2} - \left(1 + (AI_{p2})^{\omega 1}\right)^{1/\omega 1} \qquad (6)$$

For this decade $(p2)$, we can also compute the actual observed value of EI using historical evaporation data with Equation 2. This is $(EI)_{p2,act}$. Ultimately, the error in evaporative index or ΔEI, is the difference between the expected value for EI and the actual value of EI. See Equation 7. This means that the sign is positive when the actual value is higher than the expected value and the sign is negative when the actual value is lower than the expected value.

$$\Delta EI_2 = EI_{p2,act} - EI_{p2,exp} \qquad (7)$$

To calculate ΔEI for the subsequent decade, i.e., p3 (step (c) in Figure 4), the same steps as in Equation 5, 6 and 7 can be repeated. But now the omega $\omega 2$ from $p2$ is used to calculated the expected evaporative index $EI_{p3,exp}$.

Figure 5 includes the definition of ΔEI, which is the difference between the expected value of EI based on the omega value from the previous century and the actual value of EI. Positive values of ΔEI indicate upward movement within the Budyko framework, while negative values indicate downward movement.

4.1.2 Estimating changes in the root zone storage capacity $S_{r,max}$

To calculate changes in the root zone storage capacity, we use the changes in evaporation as computed in Section 4.1.1, in conjunction with the calculation of the root zone storage capacity discussed in this Section.
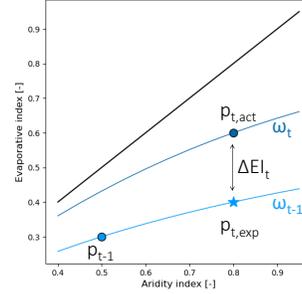
Figure 5: Budyko framework: The definition of the error in EI (ΔEI).

The root zone storage capacity can be calculated by combining long-term averages with time-dependent variables. The long-term water balance provides information on actual mean transpiration $\overline{E_t}$ (Gao et al., 2014; Nijzink et al., 2016; de Boer-Euser et al., 2016; Bouaziz et al., 2021, 2022; Hrachowitz et al., 2021). It should be noted that the term "transpiration" is used to refer to the combined processes of transpiration, and both interception and soil evaporation, as is not possible to make a clear and quantitative differentiation between these two fluxes at this scale.

The changes in storage and inter-catchment groundwater flows can be assumed to be zero, so the storage factor in the water balance equation can be eliminated.

$$\overline{P} - \overline{E_t} - \overline{Q} - \frac{dS}{dt} = 0 \qquad (8)$$

Hereafter, the long-term mean transpiration can be estimated with the remaining components of the long term water balance,

$$\overline{E_t} = \overline{P} - \overline{Q} \qquad (9)$$

where $\overline{E_t}$ is the long-term mean actual transpiration, $\overline{P}$ is the long-term mean precipitation and $\overline{Q}$ is the long-term mean catchment runoff. At this moment, there is no method to directly measure transpiration at catchment scale. Therefore, the actual mean transpiration $\overline{E_t}$ can be scaled with the ratio of long-term

mean daily potential evaporation $E_p(t)$ over the mean annual potential evaporation $\overline{E_p}$:

$$E_t(t) = \frac{E_p(t)}{\overline{E_p}} \times \overline{E_t}. \qquad (10)$$

Based on this, the cumulative deficit between actual transpiration and precipitation over time can be estimated by means of an "infinitive-reservoir". In other words, cumulative sum of daily water deficits, i.e. evaporation minus precipitation, is calculated between T_0, which is the time in which the deficit equals zero, and T_1, which is the time in which the total deficit returns to zero. The maximum deficit of this period then represents the volume of water that needs to be stored to provide vegetation with continuous access to water throughout that time:

$$S_{r,max} = \max \int_{T0}^{T1} (E_t - P_e)\, dt \qquad (11)$$

where S_R is the maximum root zone storage capacity over the time period between T_0 and T_1.

The series of annual maximum storage deficits can be fitted to a Gumbel distribution to derive the root zone storage capacity at catchment scale for different return periods. A return period of 20 years can be used, assuming that forests develop root systems to survive droughts with that return period. This method is used in various studies (Gao et al., 2014; Nijzink et al., 2016; de Boer-Euser et al., 2016; Bouaziz et al., 2022, 2021; Hrachowitz et al., 2021).

Having established the methodology for calculating root zone storage capacity, the subsequent step involves determining changes in the root zone storage capacity $S_{r,max}$. This is achieved by using the expected values for the evaporative index $\left(\frac{E_A}{P}\right)_{exp}$ obtained from Section 4.1.1.

First, we calculate the actual root zone storage capacity $S_{r,max,act}$ per decade, following the steps discussed in this Section with the actual evaporation data. Subsequently, we calculate the expected root zone storage capacity $S_{r,max,exp}$ using the expected EI derived from Equation 6 to replace the actual

evaporation term $\overline{E}_t$ from Equation 9.

For each decade, the difference between the expected root zone storage capacity $S_{r,max,exp}$ and the actual root zone storage capacity $S_{r,max,act}$ is then the error in the root zone storage capacity $\Delta S_{r,max}$, see Equation 12.

$$\Delta S_{r,max} = S_{r,max,act} - S_{r,max,exp} \qquad (12)$$

4.2 Relate changes to different climate indices

In order to explain the changes in evaporation, different climate indicators are calculated for each catchment. The climate indicators used in this study include precipitation, evaporation, temperature, aridity index, interstorm duration, seasonality index, and seasonality timing index. We calculate the values of these variables in the catchments over the entire available timeseries and also examine differences between the decades, in order to determine whether the error in EI (ΔEI from 4.1.1) can be associated with a change in the climate indicator. The groups for the climate indicators were formed in such a way as to represent different climates (Teegavarapu, 2019), and to be able to observe differences between the datasets.

4.2.1 Calculation of the different climate indicators

Firstly, the mean annual values for precipitation, evaporation, and temperature were calculated. Precipitation and evaporation were calculated by summing the total annual precipitation and evaporation for each year. For temperature, the yearly average was taken. Subsequently, the overall mean was computed over all the decades together per dataset.

The aridity index AI is an indicator that can be calculated using long-term averages. Specifically, the potential evaporation and precipitation are averaged over the entire period and divided by each other, as shown in Equation 3.

There are various indicators that can be calculated to account for seasonality. Seasonality is a critical factor that is associated with root zone storage capacity, since it can capture the seasonal differences between evaporation and precipitation (Gao et al., 2014; Van Voorst, 2020; Van Noppen, 2022).

One indicator linked to seasonality is the interstorm duration [days], which represents the maximum number of consecutive dry days in a given year. The interstorm duration is computed on an annual basis and then averaged over the entire period.

Another commonly used index to measure seasonality is the Seasonality Index (SI), which describes the distribution of precipitation over the course of a year. The SI can range from 0 to 11/6, where a value of 0 indicates that each month receives an equal amount of precipitation, and a value of 11/6 indicates that all precipitation falls in a single month (Guhathakurta and Saji, 2013). See Equation 13, where $\overline{P_m}$ is the mean monthly precipitation [mm].

$$SI = \frac{1}{\overline{P}} \sum_{m=1}^{m=12} \left| \overline{P_m} - \frac{\bar{P}}{12} \right| \qquad (13)$$

Another seasonality indicator is the Seasonality Timing Index (ST), which quantifies the timing of the peak and trough of the seasonal variability of precipitation, potential evaporation, and temperature. It describes whether the precipitation is in phase with the potential evaporation and temperature regimes. To calculate the Seasonality Timing Index, sinusoidal curves must be modeled for each variable, as shown in Equation 14, 15 and 16 (Berghuijs et al., 2014; Van Noppen, 2022).

$$P(t) = \overline{P} \left[1 + \delta_P \sin \left(2\pi \left(t - s_P \right) / \tau_P \right) \right] \qquad (14)$$

$$E(t) = \overline{E} \left[1 + \delta_E \sin \left(2\pi \left(t - s_E \right) / \tau_E \right) \right] \qquad (15)$$

$$T(t) = \overline{T} + \Delta_T \left[\sin \left(2\pi \left(t - s_T \right) / \tau_T \right) \right] \qquad (16)$$

Where t is the time [days], s is the phase shifts [-] and τ indicates the duration of the seasonal cycle, 1 year.

δ and Δ are dimensionless seasonal amplitudes. $P(t)$, $E(t)$, and $T(t)$ represent the rates of precipitation [mm/d], potential evaporation [mm/d], and temperature [C] as a function of time. The time-averaged mean values of these rates are given by $\overline{P}$, $\overline{E}$, and $\overline{T}$. The dimensionless seasonal amplitudes (δP, δE, and δT), and the phase shifts (s_P, s_E, s_T) have been determined using least squares optimization, following the method of Van Noppen (2022).

$$s_d = s_P - s_T \quad for \quad |s_P - s_T| \leq 0.5 \qquad (17)$$

$$s_d = -1 + (s_P - s_T) \quad for \quad s_P - s_T > 0.5 \qquad (18)$$

$$s_d = 1 + (s_P - s_T) \quad for \quad s_P - s_T < -0.5 \qquad (19)$$

The phase difference between the precipitation and the temperature regime (s_d) can be computed using the above equations. If $s_d = 0$, precipitation and temperature are in phase, where s_d = -0.5 indicates that the precipitation peaks before the temperature and s_d = 0.5 indicates the precipitation to peak after the temperature (Berghuijs and Woods, 2016; Van Noppen, 2022).

Using the parameters calibrated through least square error optimization, the Seasonality Timing Index (ST) can be calculated with Equation 20.

$$ST = \delta_P sgn \left(\Delta_T \right) \cos \left(2\pi \left(s_P - s_T \right) / \tau \right) \qquad (20)$$

The value for the Seasonality Timing Index can range from -1 to 1, where zero indicates uniform precipitation throughout the year. A value less than zero indicates an out-of-phase signal, with precipitation being strongly winter-dominant, while a value greater than 0 indicates that the precipitation is strongly summer-dominant (Berghuijs et al., 2014).

4.2.2 Multiple linear regression

The next step involves examining whether the error in Evaporative Index (ΔEI) can be explained by the grouping of catchments based on climate indicators or by the changes in climate indicators. To accomplish this, a multiple linear regression analysis is conducted using as dependent variable the error in EI (ΔEI) and as independent variables

the values of climate indicators ($\overline{P}_{\text{annual}}$, $\overline{E}_{\text{p,annual}}$, $\overline{T}$, AI, interstorm duration, SI, ST) and the change in those indicators ($\Delta\overline{P}_{\text{annual}}$, $\Delta\overline{E}_{\text{p,annual}}$, $\Delta\overline{T}$, ΔAI, Δinterstorm duration, ΔSI, ΔST).

Multiple linear regression is a statistical method that involves using multiple independent variables to estimate or predict the value of a dependent variable. The mathematical formulation for this technique is given in Equation 21, where y is the dependent variable, x_i are the independent variables, β_0 is the y-intercept, β_i are the regression coefficients for each of the independent variables and ϵ is the error.

$$y = \beta_0 + \beta_1 x_1 + \ldots + \beta_n x_n + \epsilon \qquad (21)$$

4.2.3 Grouping catchments by climate indicators and by changes in climate indicators

For the purpose of grouping, climate indicators were computed over the entire period of analysis, namely, 1971 - 2010 for CAMELS GB, 1981 - 2009 for CAMELS USA, 1989 - 2018 for the French catchments, and 1999 - 2018 for the Belgian and Dutch catchments. Several groups were constructed per indicator, and the catchments were assigned to a specific group. Each catchment is categorized in the same group across all periods.

Moreover, the analysis also aimed to determine the change in a climate indicator for each catchment going from one decade to the next. To achieve this, a change in indicators $\Delta indicator$ was established for each decade, by comparing with the previous decade. There are three distinct groups per indicator, namely, an increase in indicator ($\Delta indicator > 0$), a decrease in indicator ($\Delta indicator < 0$), and a small difference compared to the previous century ($\Delta indicator \approx 0$).

Statistical tests have also been performed to determine if there is a significant difference between the different groups for each dataset. The potential difference between two adjacent climate groups has been investigated. First, it needs to be determined whether the distributions of the errors in EI (ΔEI) are normally distributed. Depending on the normality of the distributions, we utilise either the Wilcoxon rank-sum test (non-normal distributions) or the t-test (normal distributions) to assess the statistical significance of the observed difference between the two groups. The Wilcoxon rank-sum test (also known as the the Mann–Whitney test or the Wilcoxon–Mann–Whitney rank-sum test) is a nonparametric test that compares the medians of two independent groups, while the t-test is a parametric test that assumes normally distributed data and compares the means of two independent groups (Helsel and Hirsch, 1992).

4.3 Hydrological modelling

4.3.1 wflow_wflow_flextopo: a process-based model

The third step is to quantify the historical changes in the evaporative index (ΔEI) in a process-based model to see the effects of the hydrological response. For this, we use wflow_flextopo (de Boer-Euser, 2017; Verseveld et al., 2022), a fully distributed process-based model designed to represent spatial variability in hydrological processes. The model uses flexible model structures for a selection of Hydrological Response Units (HRUs), which are delineated based on topography and land use. In this case, the three HRUs represent wetlands, hillslopes, and plateaus, connected through their groundwater storage. The HRUs were delineated using the MERIT hydro dataset at 60m by 90m resolution (Yamazaki et al., 2019), with a threshold of 5.9m for the height above the nearest drainage (HAND, (Rennó et al., 2008)) and a slope threshold of 0.129, following the methodology proposed by Gharari et al. (2011). The hillslopes are associated with forest and the plateaus with agriculture, using the CORINE land cover data (European Environment Agency, 2018), as they have high proportions of these land covers (Bouaziz et al., 2022). The areal fraction of each HRU was then derived for each cell at a model resolution of approximately 600m by 900m.

The wflow_flextopo model incorporates various components to simulate hydrological processes, including snow, interception, root zone, fast and slow storage, and actual evaporation from the root zone. The model is forced with precipitation, potential evaporation, and temperature data. The actual evaporation from the root zone decreases linearly as the storage falls below a certain threshold parameter. A kinematic wave approach is used to route streamflow through the upscaled river network at the model resolution, as described by Eilander et al. (2021).

4.3.2 Scenarios

The model is run using the Meuse dataset for the period during which data from both France, Belgium, and the Netherlands are available. This period is divided into two decades, p1: 1999-2008 and p2: 2009-2018. Using the omega value of one of these decades, we predict the evaporative index of the other decade. And with that predicted evaporative index, we can calculate the root zone storage capacities that are the changing variable within the model runs. The root zone storage capacity is adjusted based on historical errors in EI (ΔEI) that are found using the method described in Section 4.1.1. Four different scenarios are considered, namely A1, A2, B1, and B2. See Figure 6. Distinctions are made between scenarios in which historical errors in EI are based on either the Meuse dataset alone (A) or all datasets combined (B). The A-scenarios are based on changes in climate observed in the Meuse data. The B-scenarios are based on changes in climate from all datasets combined, including Meuse, CAMELS GB, and CAMELS USA.

Distinctions are also made based on which period is used to make a prediction about the other period (1 or 2). Scenario 1 is generated by utilising the omega value of the first decade (p1, 1999-2008) to predict the root zone storage capacity for the second decade (p2, 2009-2018). This implies that the model is executed for the period of 2009-2018. The reference run is the run where it is assumed that we are staying on the line with the same omega
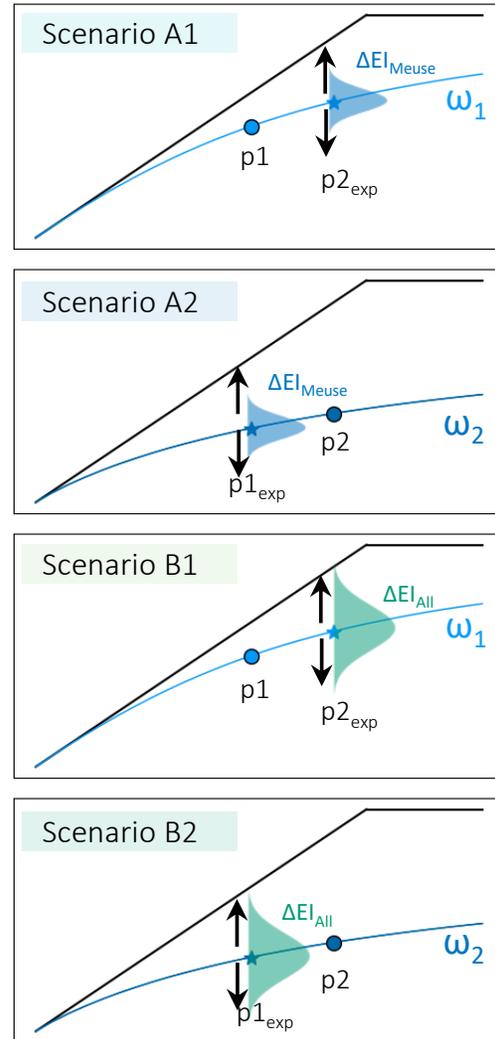
Figure 6: Overview of the scenario structure. p1 is the time period of 1999-2008 and p2 is the time period of 2009-2018.

value, so the error in EI ΔEI is equal to zero (see star in Figure 6). Other runs also utilise the omega value from the first decade (1999-2008) to make predictions, but now a sample of an error (ΔEI) is taken from the population (either Meuse or all data) to calculate the root zone storage capacity. Scenario 2 makes predictions by reversing time. The

omega value of the second decade (p2, 2009-2018) is used to predict the root zone storage capacity for the first decade (p1, 1999-2008), meaning that the model is executed for the period of the first decade (p1, 1999-2008). Samples of ΔEI are taken from the distributions (either Meuse only for A-scenarios or all data for B-scenarios) to calculate different root zone storage capacities. When sampling from the distribution in Scenario 2, the sign of ΔEI is reversed to move in the correct direction. Specifically, a negative value of ΔEI is made positive, while a positive value of ΔEI is made negative.

In each scenario the model is run multiple times, where each run is a prediction based on an error in evaporative index, ΔEI, sampled from the distribution. This process is repeated 100 times per scenario to generate a distribution of possible outcomes.

– *Scenario A1* uses the omega value of p1 with a sampled ΔEI from the distribution calculated from the Meuse data to make a prediction about the evaporation and root zone storage capacity of p2, 2009-2018.

– *Scenario A2* uses the omega value of p1 with a sampled ΔEI from the distribution calculated from the Meuse data to make a prediction about the evaporation and root zone storage capacity of p1, 1999-2008.

– *Scenario B1* uses the omega value of p1 with a sampled ΔEI from the distribution calculated from all the data (Meuse, CAMELS USA, CAMELS GB) to make a prediction about the evaporation and root zone storage capacity of p2, 2009-2018.

– *Scenario B2* uses the omega value of p1 with a sampled ΔEI from the distribution calculated from all the data (Meuse, CAMELS USA, CAMELS GB) to make a prediction about the evaporation and root zone storage capacity of p1, 1999-2008.

4.3.3 Model calibration

Bouaziz et al. (2022) performed the calibration of the model with a Monte Carlo strategy to explore the parameter space by sampling 10,000 realizations from uniform prior parameter distributions. This approach resulted in the identification of an ensemble of plausible parameter sets, from which this study uses one. To evaluate the model's ability to simulate outflow with this parameter set, hydrographs of observed and modeled streamflow for Borgharen are presented in Figure 7. Furthermore, several performance indicators, namely Nash-Sutcliffe efficiencies of streamflow, the logarithm of streamflow, and Kling-Gupta efficiency of streamflow, are shown in Figure 8 to assess the model's performance. Performance indicators are used to evaluate the accuracy of hydrological models in simulating streamflow. The three commonly used indicators are Nash-Sutcliffe efficiency (NSE), logarithmic Nash-Sutcliffe efficiency (NSE_{log}), and Kling-Gupta efficiency (KGE). NSE and **NSElog** measure the ratio of the model's mean square error to the mean square error of the observed data, with higher values indicating better model performance. KGE measures the correlation, variability, and bias between the observed and simulated streamflow, also with higher values indicating better performance.

The models in Scenario 1 performed well in most catchments with an average NSE of 0.59, average NSE_{log} of 0.68, and average KGE of 0.88. Similarly, in Scenario 2, the models showed comparable performance with an average NSE of 0.62, average NSE_{log} of 0.65, and average KGE of 0.83. However, catchments Modave and Jemelle exhibited poor model performance in both scenarios, with negative NSE and NSE_{log} values. The underlying geology of these catchments is complex, and they are likely experiencing groundwater losses, which is not accounted for in the wflow_flextopo model used here. (Bouaziz et al., 2018).
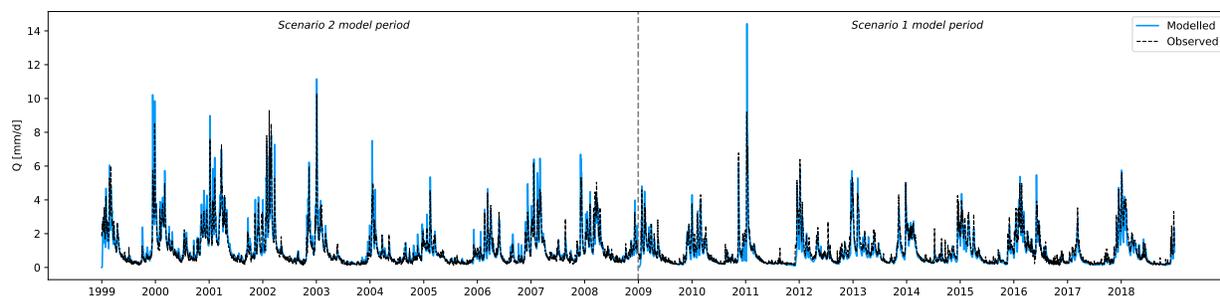
Figure 7: Hydrograph of modeled and observed streamflow in Borgharen, where for scenario 1 and 2 respectively the values for Nash-Sutcliffe efficiencies of streamflow are 0.85 and 0.81, Nash-Sutcliffe efficiencies of the logarithm of streamflow 0.71 and 0.63 and Kling-Gupta efficiency of streamflow 0.88 and 0.83.
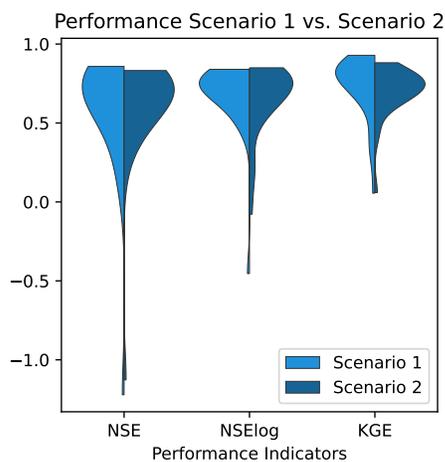
Figure 8: Performance indicators calculated for the time period of each scenario: Nash-Sutcliffe efficiencies of streamflow, the logarithm of streamflow, and Kling-Gupta efficiency of streamflow. The bandwidth of each violin represents the distribution of performance across different catchments.

5 Results

In this chapter the results will be discussed, for I) the historical changes in evaporation and the root zone storage capacity in Section 5.1, II) the relationship between the changes with climate indicators in Sec-

tion 5.2 and III) the quantification of the effect of the changes on the hydrological response in Section 5.3.

5.1 Historical changes in evaporation and the root zone storage capacity

5.1.1 Catchment selection

Several catchments were excluded from the analysis because they did not meet the water balance in every decade as they exceeded the energy limit ($EI > AI$). This means that the Fu-equation could not be solved, and the data is likely incorrect due to groundwater losses.

In addition, the following requirements were imposed on the catchments of the CAMELS datasets: there should be minimal human impact, and no more than 10% of the annual precipitation can be from snowfall. Catchments with too much snowfall are excluded because of the ability of snowfall to temporarily store water until it melts. In catchments that receive significant snowfall, the estimation of root zone storage capacity may be inaccurate because of the delayed input of water.

To identify catchments with climatic conditions similar to those of the present or future Meuse, carefully selected catchments were used. Specifically, following the methodology outlined by Van Noppen (2022), only catchments located on the East Coast

of the CAMELS USA dataset were considered. Also, some catchments were eliminated based on data availability (Van Noppen, 2022). After applying the selection criteria, a total of 286 catchments remained for analysis. These catchments comprised of 94 from the CAMELS GB dataset, 169 from the CAMELS USA dataset, and 23 of the Meuse.

5.1.2 Data visualisation in the Budyko framework

In Figure 9, the different datasets are plotted in the Budyko framework. This plot was generated using the long-term average values for the entire period of data analysis. The CAMELS USA dataset consists of catchments with considerably drier climates (higher aridity index), while the CAMELS GB dataset has catchments with a wetter climate (lower aridity index). The Meuse dataset falls somewhere in the middle, where both CAMELS datasets also have some catchments in the framework. The data points fall along a line, following the theories of Budyko (1961) and Fu (1981).
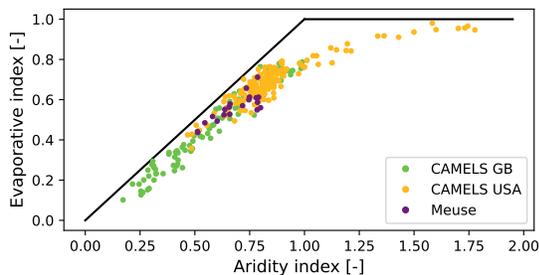
Figure 9: Illustration of the long-term average values for the entire period of data analysis. The evaporative index is calculated with Equation 2 and aridity index is calculated with Equation 3.

To provide an indication of how the root zone storage capacity relates to the Budyko framework, Figure 10 displays the values of root zone storage capacity, using a colour scale, for all catchments - Meuse, CAMELS USA, and CAMELS GB - within the framework. The root zone storage capacity was calculated using the method discussed in Section

4.1.2. There is a clear pattern where higher values of the evaporative index and aridity index are associated with larger root zone storage capacities. Conversely, catchments with lower values of the evaporative index and aridity index are associated with smaller values of the root zone storage capacity.
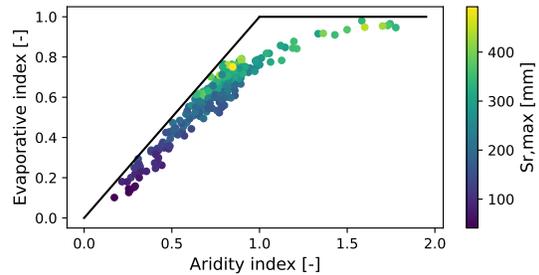
Figure 10: Root zone storage capacities ($S_{r,max}$) in the Budyko framework for Meuse, CAMELS GB, and CAMELS USA catchments.

5.1.3 Error in estimating the evaporative index (ΔEI)

Figure 11 shows the histograms of the error in predicting the evaporative index (ΔEI) per decade. The error in the evaporative index (ΔEI) can be calculated per catchment for every decade of which data is available, except the first decade, as a reference omega value is needed.

To assess whether there are differences in the distribution of errors in EI between decades of the same dataset, it is first necessary to test whether the distributions are normally distributed. To do this, QQ plots were created (Appendix C) and the Shapiro-Wilk test was performed (see Table 2). The Shapiro-Wilk test (Shapiro and Wilk, 1965) is a statistical test for normality. The test statistic, W, measures the deviation between the sample data and a normal distribution. A larger value of W indicates a greater deviation and lower likelihood of normality. The p-value is calculated from the W statistic, and if it is below a pre-specified significance level (e.g., 0.05), we reject the null hypothesis of normality.
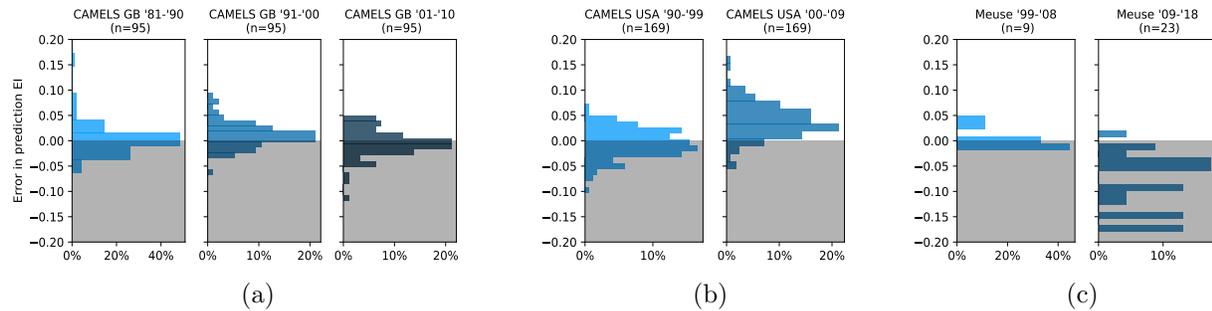
Figure 11: Error in estimating EI (ΔEI) for the different datasets. The white area of the histogram indicates positive values and the grey part of the histogram indicates negative values. For (a) CAMELS GB the median ΔEI for 1981-1990 is 0.00, the median ΔEI for 1991-2000 is +0.01 and the median ΔEI for 2001-2010 is 0.00. For (b) CAMELS USA the median ΔEI for 1990-1999 is -0.01, the median ΔEI for 2000-2009 is +0.04. For (c) the Meuse the median ΔEI for 1999-2008 is 0.00, the median ΔEI for 2008-2018 is -0.06.

For the Meuse, the results from the first decade (1999-2008) are significant, but caution should be exercised when drawing conclusions from these findings as the sample size for the Meuse is very small. The test suggests that for all decades of the CAMELS GB dataset, ΔEI is likely not normally distributed, as its p-value is below 0.05. On the other hand, the distributions for CAMELS USA may exhibit normality. Therefore, we proceed with the Wilcoxon rank-sum test for all datasets to be consistent. This test does not require the data to be normally distributed, and it can handle data where the two groups (in this case, decades) have unequal sizes, which is the case for the Meuse data.

The Wilcoxon rank-sum test is a non-parametric statistical hypothesis test that determines whether there is a significant difference between two unpaired samples. The test statistic is the sum of the ranks of one sample in the combined sample of both groups. A larger test statistic indicates a larger difference between the two samples. The p-value is the probability of observing the data under the assumption that the null hypothesis is true, where the null hypothesis is that there is no difference between the two samples. If the p-value is less than the threshold

Table 2: Shapiro-Wilk Test results for the normal distribution of the error in the evaporative index ΔEI, per decade and dataset. The p-values below the significance level (0.05) are bold.

Dataset & Decade	n	Test Statistic	p-value
CAMELS GB 1981-1990	95	0.66	**0.000**
CAMELS GB 1991-2000	95	0.96	**0.010**
CAMELS GB 2001-2010	95	0.95	**0.001**
CAMELS USA 1990-1999	169	0.99	0.442
CAMELS USA 2000-2009	169	0.99	0.104
Meuse 1999-2008	9	0.82	**0.038**
Meuse 2009-2018	23	0.94	0.148
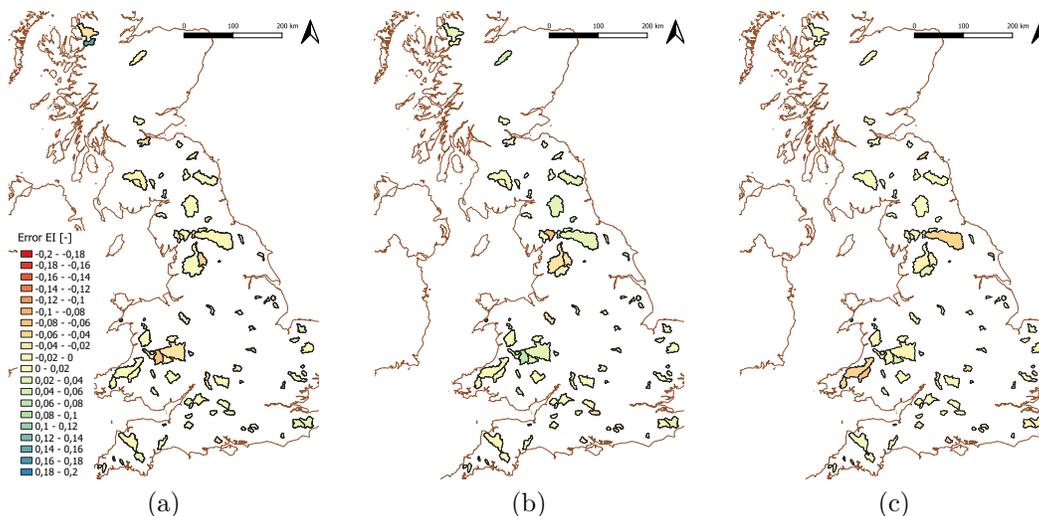
Figure 12: CAMELS GB - Errors in estimating EI for time periods (a) 1981-1990 (b) 1991-2000 (c) 2001 - 2010. The colours indicate the error in EI (ΔEI), ranging from -0.2 (red) to +0.2 (blue).

(< 0.05), it suggests that there is a significant difference between the two samples and the null hypothesis can be rejected (Helsel and Hirsch, 1992).

See Table 3 for the results of the Wilcoxon rank-sum tests. The p-values for all comparisons were found to be less than 0.05, indicating that there is a significant difference in the distribution of error in EI between the decades for each dataset. This suggests that the distribution of error in evaporative index (ΔEI) is not consistent over time.

The errors in EI (ΔEI) are geographically illustrated in Figures 12, 13 and 16, with the colour scheme indicated in the legend. There is no apparent geographical pattern in the errors observed for all datasets. For CAMELS GB, adjacent catchments display opposing error signs, with a positive and negative error adjacent to each other. Conversely, for the Meuse dataset, neighbouring catchments exhibit similar errors in close proximity to one another. In Figure 14, the found errors in evaporative index (ΔEI) of all data are combined and plotted per aridity index to gain an understanding of the magnitude of changes in the Budyko framework.

Table 3: Wilcoxon rank sum test results fordifferences in mean of errors in evaporative index ΔEI, between two decades of one dataset.

Decade 1	Decade 2	Test Stat.	p-value
CAMELS GB 1981-1990	CAMELS GB 1991-2000	3355	**0.002**
CAMELS GB 1991-2000	CAMELS GB 2001-2010	6103	**0.000**
CAMELS USA 1990-1999	CAMELS USA 2000-2009	4403	**0.000**
Meuse 1999-2008	Meuse 2009-2018	196	**0.000**

5.1.4 Error in estimating the root zone storage capacity

The discovered error in EI was used to calculate the error in $S_{\mathrm{r,max}}$ as discussed in Section 4.1.2. These errors are combined per dataset as can be seen in Figure 15. The relative error is calculated by dividing
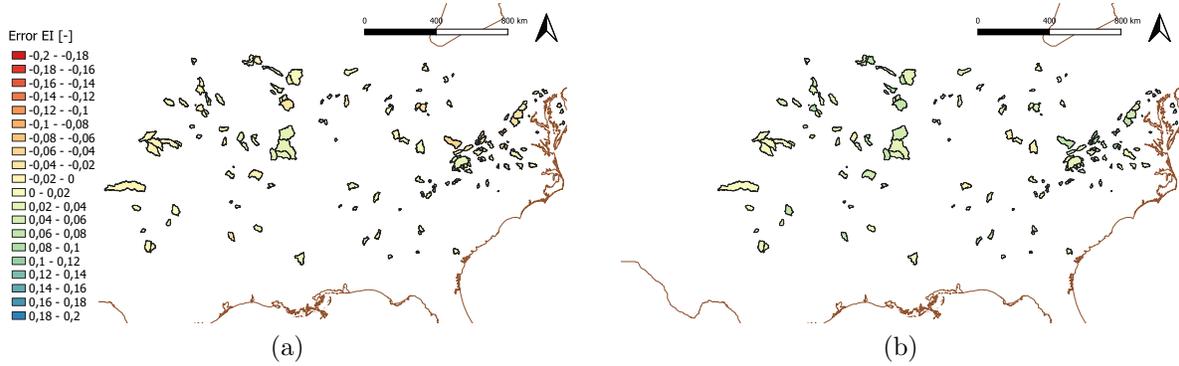
Figure 13: CAMELS USA - Errors in estimating EI for time periods (a) 1990-1999 (b) 2000-2009. The colours indicate the error in EI (ΔEI), ranging from -0.2 (red) to +0.2 (blue)
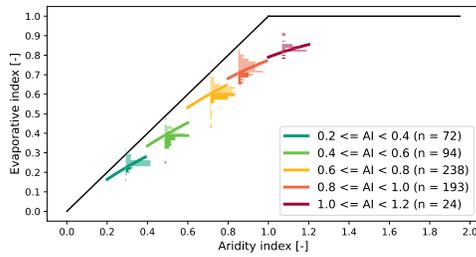
Figure 14: Errors in Evaporative index [-] plotted per aridity index in the Budyko framework, for all datasets combined.

the error in the root zone storage capacity by the actual value, see Equation 22.

$$\Delta S_{\text{r,max}}[\%] = \frac{S_{\text{r,max,act}} - S_{\text{r,max,exp}}}{S_{\text{r,max,act}}} \quad (22)$$

For both CAMELS datasets, the distribution is centered around 0, but for the Meuse dataset, there is often a negative error, indicating that the root zone storage capacity is often overestimated using this method and is therefore smaller than expected.

In Figure 17, the errors in $S_{\text{r,max}}$ for all decades and datasets are plotted in the Budyko framework. No clear trend is observed between the error size and the aridity index. However, the largest absolute positive errors in $S_{\text{r,max}}$, indicating underestimation,
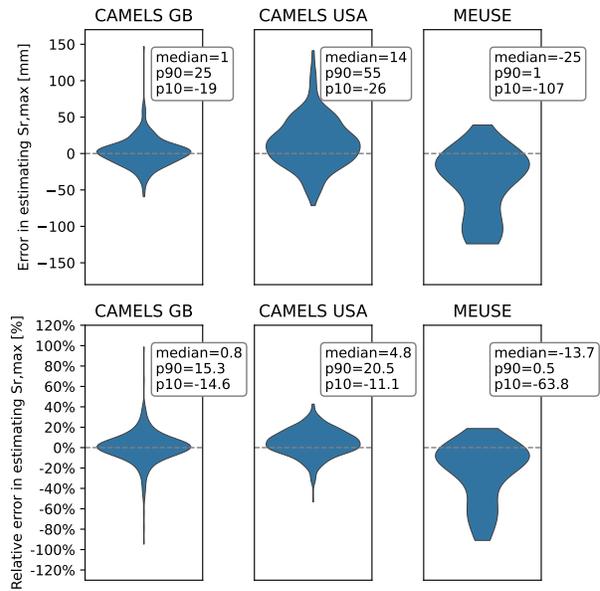
Figure 15: The absolute [mm] and relative error [%] in $S_{\text{r,max}}$ for each dataset. In the text boxes, the median and the 10th-90th percentiles are indicated.

are observed in the upper region of the Budyko framework. When examining the relative error, these errors are less significant in the upper region, which is reasonable given that Figure 10 showed that the largest root zone storage capacities are in
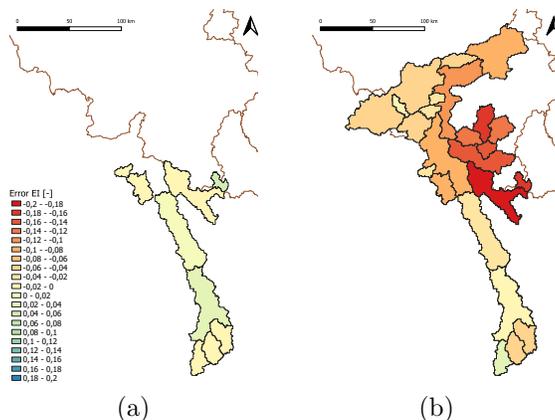
Figure 16: Meuse - Errors in estimating EI for time periods (a) 1999-2008 (b) 2009-2018. Note that for the first period, data is only available for the French section of the Meuse. The colours indicate the error in EI (ΔEI), ranging from -0.2 (red) to +0.2 (blue).

the upper region of the Budyko framework. The catchments with the largest negative error in $S_{r,max}$, indicating overestimation, are plotted furthest from the energy limit. This suggests that the actual evaporation is relatively lower than the potential evaporation in these catchments.

5.2   Linking to climate indicators

5.2.1   Multiple linear regression

Table 4 presents the key regression results of the multiple linear regression analysis, while all the regression results can be found in Appendix D. For CAMELS GB, the R-squared value is 0.076, indicating that 7.6% of the variance in ΔEI can be explained by the independent variables, i.e. the climate indicators and the change in indicators. This relatively low R-squared value suggests that there is still much unexplained variance in ΔEI for CAMELS GB. With a chosen significance level (alpha) of 0.05, we reject the null hypothesis when the p-value is less than 0.05. In this case, the p-value is 0.083, which is greater than 0.05, and hence, we cannot reject the null hypothesis. This means that we do not have sufficient evidence to conclude that there is a significant relationship between the independent variables and the dependent variable in
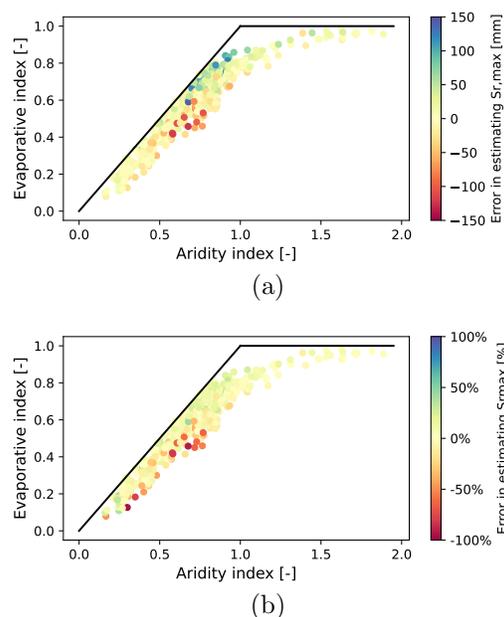
Figure 17: Error in estimating the root zone storage capacity ($S_{r,max}$) plotted in the Budyko framework by colour scale, (a) in absolute values [mm] and (b) in percentages [%]

Table 4: Summary results multiple regression, where the dependent variable is the error in EI (ΔEI).

	CAMELS GB	CAMELS USA	Meuse
R-squared	0.076	0.267	0.945
Adjusted R-squared	0.028	0.235	0.900
Probability (F-statistic)	0.083	0.000	0.000
Coefficient 1	SI: -0.247	ΔSI: -0.134	SI: 3.375
Coefficient 2	ΔAI: 0.199	ΔAI: 0.089	ΔAI: -2.228
Coefficient 3	ΔSI: 0.144	AI: -0.058	AI: 1.453
Coefficient 4	ST: 0.090	ΔT: -0.052	ΔSI: -1.257
Coefficient 5	ΔT: 0.039	ΔST: 0.047	ST: -0.867

the regression analysis for CAMELS GB.

For the other datasets, the significances are below the chosen alpha level, implying that the results are significant. For CAMELS USA with an R-squared of 0.267 and an adjusted R-squared of 0.234, we observe that the overall fit of the model is not very strong, meaning that there is again still much unexplained variance in ΔEI.

For Meuse, with an R-squared of 0.945 and an adjusted R-squared of 0.900, we see that the overall fit of the model is very strong, which means that a large part of the variance in the errors in ΔEI can be explained by the independent variables. Interpreting the results of a multiple regression analysis involves examining the coefficients and significance levels for each independent variable. The coefficients represent the magnitude of the effect of each variable on the dependent variable ΔEI, while the significance levels indicate the strength of the relationship between each independent variable and the dependent variable. We identified the significant independent variables if their significance level is 0.05 or lower. Furthermore, the order of the variables in the table reflects the magnitude of their coefficients, which represents their relative importance in predicting the dependent variable. A complete list of all coefficients and significances can be found in Appendix D.

We observe that seasonality, specifically seasonality timing index and seasonality index, aridity index, and change in temperature are important explanatory variables. We are excluding CAMELS GB from our analysis due to its low significance. We observe that the coefficients for CAMELS USA and Meuse do not always move in the same direction. While ΔSI is linked to a negative error in ΔEI for both datasets, ΔAI is associated with an increase in ΔEI for CAMELS USA, but a decrease in ΔEI for Meuse. Furthermore, a higher AI has a decreasing effect on ΔEI for CAMELS USA, but an increasing effect for Meuse. ΔST is accompanied by an increase in ΔEI for CAMELS USA, but a decrease for Meuse.

5.2.2 Grouping by climate indicators and by change in climate indicators

Grouped histograms of the error in EI can be found in Appendix E, and the results of the Wilcoxon signed rank tests and other descriptive statistics for the climate groups can be found in Appendix F. This section provides a detailed discussion of the significant differences observed for each climate indicator when grouping the variables based on their absolute value and grouping them based on their change per variable.

Precipitation When grouping the catchments based on average annual precipitation ($\overline{P}_{\text{annual}}$), we did not observe any significant differences among the groups. However, when grouping them based on changes in average annual precipitation ($\Delta \overline{P}_{\text{annual}}$), we obtained different results. For CAMELS GB, there was no significant difference between the group with a decrease in annual precipitation and the group with little change in precipitation. However, we did observe a significant difference between the group with an increase in precipitation

and the group with little change in precipitation. For CAMELS USA and the Meuse, we observed significant differences between all the groups of change in precipitation. The significant differences observed in both CAMELS datasets suggest that a decrease in precipitation is associated with a more positive error in EI, and vice versa. However, in the case of the Meuse catchment, a decrease in precipitation is associated with a more negative error in EI.

Potential evaporation When grouping the catchments based on the average potential evaporation value over the entire period $(\overline{E}_{p,annual})$, we did not observe any differences between the groups. However, when grouping based on changes in potential evaporation $(\Delta \overline{E}_{p,annual})$, we did observe a difference between the group with an increase in potential evaporation and the group with little change in the CAMELS GB and the Meuse catchments. An increase in potential evaporation is associated with a more positive error in EI.

Temperature When grouping the catchments based on the average temperature over the entire period $(\overline{T})$, we did not observe any differences between the groups. However, when grouping based on changes in temperature $(\Delta \overline{T})$, we did observe significant differences only for the CAMELS USA and the Meuse catchments. For CAMELS USA, an increase in temperature is associated with a less positive error in EI. Conversely, for the Meuse catchment, an increase in temperature is associated with a less negative error in EI.

Aridity index Upon grouping by aridity index over the entire period (AI), significant differences were observed only for the Meuse, where the group with a higher aridity index exhibited a less negative error in EI. Moreover, examining the differences in changes in aridity index (ΔAI), no significant differences were found for CAMELS GB. For CAMELS USA, differences were observed among all three groups, where an increase in AI was associated with a more positive error in EI, while a decrease in AI corresponded to a less positive error in EI. Contrasting, at the Meuse, differences were found between the group with little change in AI versus the group with an increase in AI, where the latter exhibited a more negative error in EI.

Interstorm duration When grouping by interstorm duration (interstorm duration) over the entire period, significant differences were observed only for the Meuse, where the group with a longer average interstorm duration exhibited a less negative error in EI. No significant differences were found when grouping by change in interstorm duration (Δinterstorm duration) for CAMELS GB. Significant differences were found between all groups for CAMELS USA and the Meuse. An increase in interstorm duration for CAMELS USA was associated with a more positive error in EI, while a decrease corresponded to a less positive error in EI. On the other hand, a decrease in interstorm duration for the Meuse was associated with a less negative error in EI.

Seasonality index Significant differences were found only for the Meuse data when grouping by seasonality index (SI), with catchments exhibiting a higher SI value showing a more negative error in EI. When grouping by change in SI (ΔSI), no significant differences were found between groups for CAMELS GB. However, for both CAMELS USA and the Meuse data, a significant difference was observed only between the group with a decrease in SI and the group with little change in SI. In both cases, a decrease in SI was associated with a more positive error in EI.

Seasonality timing index No significant differences were found between groups when calculating the seasonality timing index (ST) over the total period. However, differences were observed when examining the change in seasonality timing index (ΔST) for both the CAMELS USA dataset and the Meuse data. Specifically, a decrease in ST for CAMELS USA was associated with a less positive error in EI, while the opposite was observed for the Meuse, where a decrease in ST was associated with a less negative error in EI.

5.3 Effect on the streamflow of the Meuse

Figure 18 displays the distributions of the errors in EI that were used for the different scenarios. Figure 18 shows the distribution of errors observed in the Meuse dataset, which serves as the basis for the A-scenarios. and the distribution observed across all decades in all datasets, which serves as the basis for the B-scenarios.
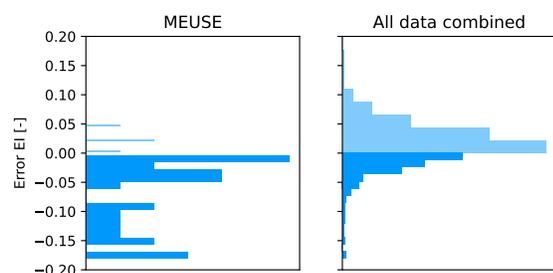
Figure 18: Error in evaporative index ΔEI used for the samples.

The average monthly streamflow for Borgharen is depicted in Figure 19, providing insight into the high and low flow months. This visualisation is included to interpret the seasonal effects of the change in streamflow. We see that the months with high flow are December to March and the months with low flow are June to September.
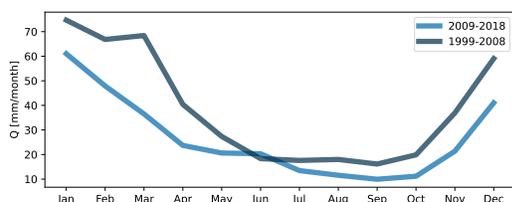
Figure 19: Monthly flow Borgharen [mm/month] for both model run periods based on the E-obs v20 data.

5.3.1 Seasonal changes in evaporation and streamflow

In Figure 20, (a) and (b), the changes in streamflow and actual evaporation for scenario A1 are displayed, respectively. For every run the streamflow and evaporation were compared to the reference run ($\Delta EI = 0$). The data from all years and catchments are aggregated and the percentiles are plotted. The results indicate a decrease in evaporation (up to 13%, median of 4%) during summer months in scenario 1A, which leads to an increase in streamflow in the months of September, October, and November (up to 48%, median of 12%). There is also a small decrease in the summer months (up to 5%, median of 1%). In scenario 2A (Figure 20, (c) and (d), we observe an opposite pattern compared to scenario 1A. This is expected since scenario 2A is the inverse of scenario 1A. Specifically, we observe an increase in evaporation during summer months (up to 22%, median of 6%), which results in a decrease in streamflow during winter months (up to 23%, median of 7%). There is a again a small increase in streamflow during summer months in this scenario (up to 14%, median of 2%).

The distribution of errors in EI (ΔEI) for all combined data is more symmetrical (see Figure 18), which leads to more symmetrical results for scenarios B1 and B2. However, the distribution does tend towards the positive side, which causes the median change in evaporation to be slightly above 0% for scenario B1 (see Figure 21 (a) and (b)), and the median change in streamflow to be slightly below 0%. Once again, the largest changes occur for evaporation during summer months (from -3% to 5% and -7% to +5%) and for streamflow during the autumn and early winter months, September to December (from -11% to +7% and from -5% to +10%). For scenario B2 (see Figure 21 (c) and (d), we observe the opposite of scenario B1, where the changes in evaporation and streamflow are relatively symmetrical. However, in this case, the median change in evaporation is slightly below 0 percent and the median change in streamflow is slightly above 0 percent.

The effect of climate variability on the root zone storage capacity
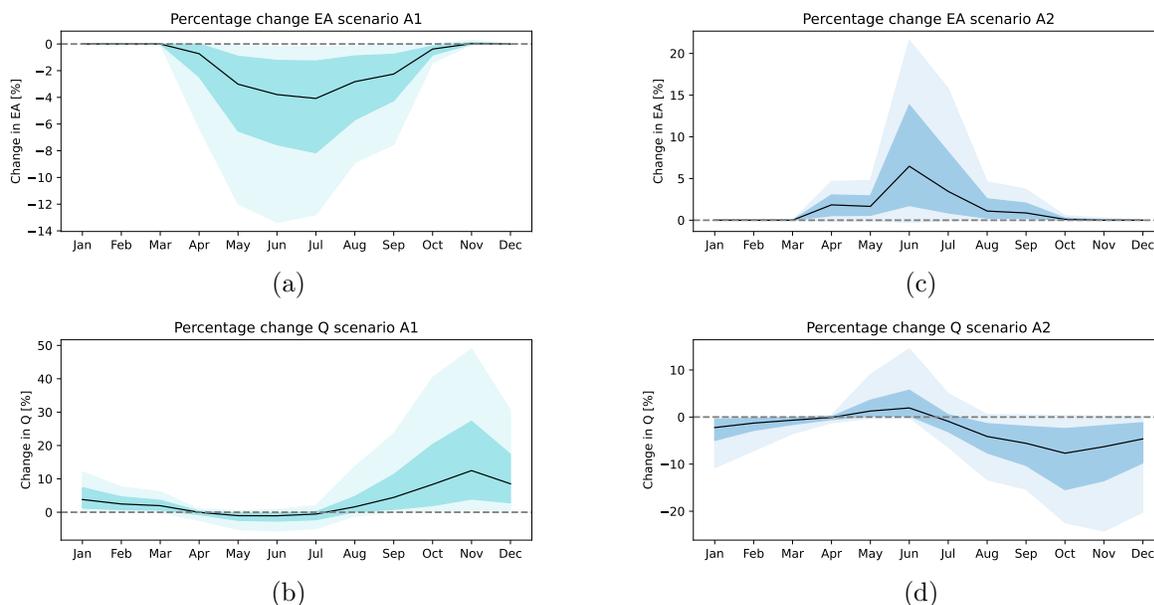
Figure 20: Change in evaporation and streamflow for scenario A1 and A2. The change is calculated for every run as the difference between the evaporation or streamflow with the reference run ($\Delta EI = 0$). The output for all years, catchments, and runs has been put together. The lightly shaded area represents the 90th and 10th percentiles, while the slightly darker shaded area represents the 25th to 75th percentiles. The black line represents the median.

5.3.2   Change in maximum flow ($Q_{\max}$) and minimum flow ($Q_{\min}$)

For each simulation run, the annual maximum flow ($Q_{\max}$) was calculated. As the maximum flow occurs around the turn of the year, the time period used for the calculations spanned from July of one year to June of the following year. In order to investigate changes in the magnitudes of high flows, the mean $Q_{\max}$ for each simulation run was compared to the mean $Q_{\max}$ of the reference run ($\Delta EI = 0$). The results of this analysis are illustrated in percentages of the $Q_{\max}$ in Figure 22 for all catchments combined [%]. The results per catchment in [mm/d] in can be found in Appendix G.

For the A-scenarios the change in $Q_{\max}$ have a median of +4.8% and -3.2% and for the B-scenarios these are -0.9% and +0.2%. Notably, certain sub-catchments such as Salzinnes, Huccorgne, La Meuse Goncourt, Le Mouzon Circourt-sur-mourzon, and Le Vair Soulesse sous Saint-Elophe exhibited higher sensitivity to changes in maximum flow, either in terms of increases or decreases.

The percentages of increase and decrease in $Q_{\max}$ are not as significant as those in streamflow. This can be attributed to the seasonal patterns presented in Figure 19, which indicate the months with high flow. The peak of the percentage increase in flow occurs around the autumn months, thereby having less impact than if this were to occur during the winter months. The timing of the $Q_{\max}$ was also examined, and the results are presented in Table 5. In Appendix H the change in timing for every catchment can be found. For the A2 scenario, the timing of the $Q_{\max}$ is on average one day later than in the reference run where $\Delta EI = 0$. For the other scenarios there
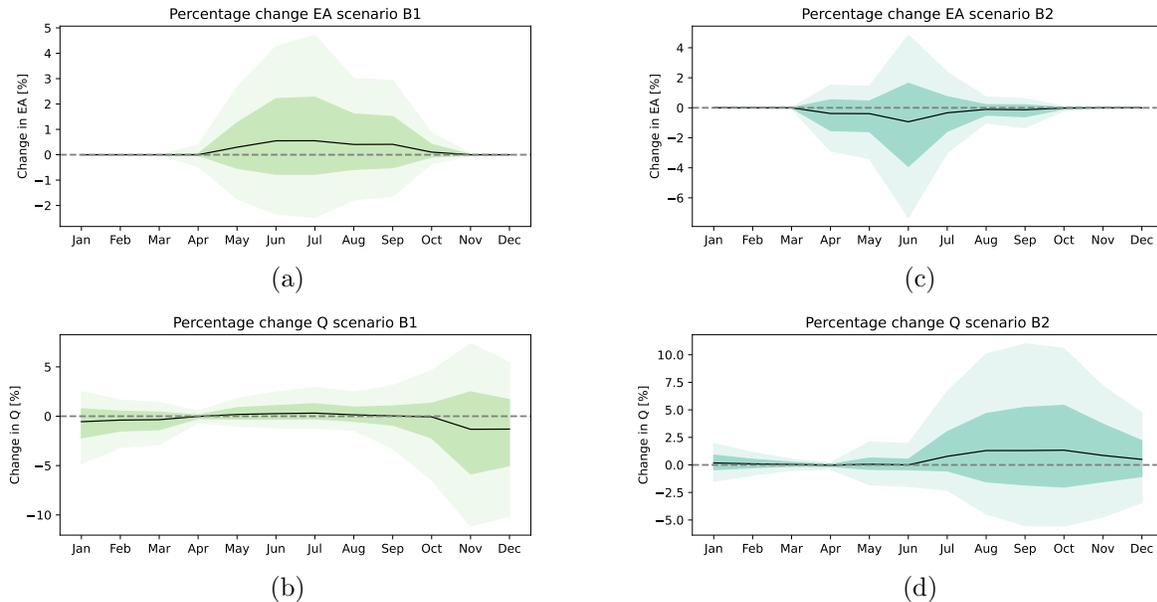
Figure 21: Change in evaporation and streamflow for scenario B1 and B2. The change is calculated for every run as the difference between the evaporation or streamflow with the reference run ($\Delta EI = 0$). The output for all years, catchments, and runs has been put together. The lightly shaded area represents the 90th and 10th percentiles, while the slightly darker shaded area represents the 25th to 75th percentiles. The black line represents the median.

is on average no change in timing of the AMF. Also the standard deviations are not very different from the standard deviation of the reference run.

To analyze the low flows (Q_{min}), we examined the minimum flow over a period of 7 consecutive days. Unlike the analysis of the high flows (Q_{max}), we considered the calendar year since low flows typically occur during the summer months. For each 7-day period throughout the year, the total flow was calculated using a moving window approach. The calculations were performed for all simulation runs for all years, and the resulting averages were compared to the average of the reference run ($\Delta EI = 0$). The results are presented in Figure 22 for all catchments combined [%]. See Appendix G for the results per catchment [mm/d]. It shows that again the A-scenarios exhibit relatively greater changes in low flow compared to the reference scenario. The

Table 5: Change in timing of Q_{max} per scenario. Ref. run Q_{max} is the timing of the Q_{max} for all catchments combined for the reference run. Also the standard-deviation of the Q_{max} is given. Δt is the average change in Q_{max} compared to the reference run ($\Delta EI = 0$), calculated for each scenario, with the standard-deviation. Unit of all columns is days.

	Ref. run AMF	Ref. run std	Scen. Δt	Scen. std
Scenario A1	01-12	38	0	34
Scenario A2	29-11	27	+1	26
Scenario B1	01-12	38	0	38
Scenario B2	29-11	27	0	28

median in the change in $Q_{\min}$ for the A-scenarios is -0.4% and +1.7%, and for the B-scenarios +0.5% and +0.34%.
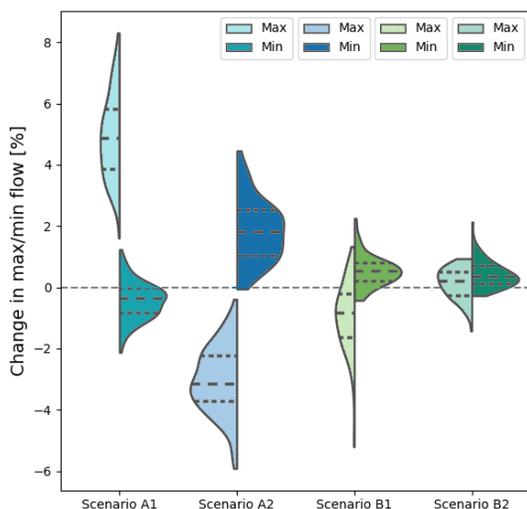
Figure 22: Change in maximum flow ($Q_{\max}$, left part of the violin) and 7-day minimum flow ($Q_{\min}$, right part of the violin), in percentage of the reference run. The quartiles are indicated with dashed lines. The median of the change in $Q_{\max}$ and $Q_{\min}$ per scenario are respectively A1: +4.8%, -0.4%, A2: -3.2%, +1.7%, B1: -0.9 %, +0.5%, B2: +0.2%, +0.3%.

6   Discussion

6.1   Limitations

6.1.1   Hydrological Data

Sufficiently long time series of data are essential for investigating the influence of climate variability as this enables us to analyse historical patterns and trends. Unfortunately, the availability of long-term data is limited. The restricted timeframe of the available data may impact the accuracy and reliability of the results. Although the availability of long-term data is limited in this research, significant efforts have been made to utilise the available data as efficiently as possible. Potential errors in the input data may also have impacted the accuracy of the water balance method and consequently the findings of this study. Hydrological data are subject to uncertainties typically ranging from 10% to 40%, which can arise from various sources such as measurement errors, data derivation, interpolation, scaling, and data management (McMillan et al., 2018). When constructing a large sample dataset, multiple sources of data are often combined. To ensure that the compared data reflect similar processes, catchments that are significantly affected by human activities or snow accumulation are excluded in this study (Van Noppen, 2022). Despite these measures, it is important to acknowledge that the utilisation of any dataset carries inherent uncertainty, which should be taken into account in the interpretation of the results.

Considering the potential for data inaccuracies, it is noteworthy that the Meuse presents a different outcome in contrast to the other datasets. To address this discrepancy, an additional analysis was conducted on the climate forcing variables of the Meuse, including precipitation, potential evaporation, and temperature. Results indicate a declining trend in precipitation. To confirm that this trend is not an artefact of the data, a comparison was made with alternative versions of the dataset, E-OBS v24 and E-OBS v25, as well as with a different dataset that is based on a climatological grid. Further details can be found in Appendix I. The analysis suggests

that the dataset used in this study, E-OBS v20, displays a slightly stronger declining trend, but this trend is also present in the other datasets, thereby confirming that it is not an artefact of the dataset.

Different methods were used to estimate potential evaporation in the catchments studied. The E-OBS meteorological data (Cornes et al., 2018) used the Makkink equation to estimate potential evaporation for the Meuse catchments, while the Priestley-Taylor equation and the Penman-Monteith equation were used by the CAMELS-USA and CAMELS-GB catchments, respectively. To ensure consistency across the datasets, the approach of Van Noppen (2022) was adopted where in the majority of datasets the Makkink equation was applied which is based solely on temperature and incoming short-wave radiation data. However, other factors such as relative humidity and wind speed can also impact potential evaporation rates. Consequently, this method may introduce a degree of uncertainty in the potential evaporation estimates.

6.1.2 Water balance method

The water balance method estimates root zone storage capacity by calculating the maximum annual water deficits, which are determined by the difference between cumulative daily precipitation and transpiration. Given the complexity of measuring transpiration at the catchment scale, this parameter is estimated based on long-term water balance calculations. Daily potential evaporation rates are used to generate daily transpiration values, thereby preserving the seasonal trends in transpiration while still adhering to mean transpiration amounts. Nonetheless, this approach fails to account for extreme events and inter-annual variability in transpiration, particularly during hydrological events characterised by limited or abundant water availability. This assumption implies that vegetation can extract water for transpiration from dry soils as easily as from wet soils. This introduces an element of uncertainty into the water balance method, and its impact is difficult to quantify given that the values cannot be validated against real-world

transpiration data. In addition to these limitations, the water balance method may not be suitable for regions where the water table is situated close to the surface and vegetation can extract water directly from groundwater, rather than relying on a buffer capacity (Fan et al., 2017; Bouaziz et al., 2022).

The water balance method is a conceptualization of reality, which disregards some processes. Firstly, interception is not taken into account. This process occurs when precipitation falls on vegetation, and some of it is captured and stored on the leaves, stems, or branches, reducing the amount of water that reaches the soil surface. Bouaziz et al. (2020) reported that the fluctuations caused by interception are insignificant when compared to the magnitude of storage deficits. Consequently, it is believed that the absence of interception in the water balance method is unlikely to have a substantial impact on the results of this research. Furthermore, the method assumes that all precipitation immediately infiltrates the root zone, thereby neglecting other processes, such as Infiltration Excess Overland Flow and Saturation Excess Overland Flow. Infiltration Excess Overland Flow occurs when the water input exceeds the soil's infiltration rate during periods of extreme precipitation. Saturation Excess Overland Flow occurs when the soil pores are entirely filled, causing saturation and resulting in overland flow. Both processes indicate high water volumes that have entered or want to enter the system. However, since such processes are unlikely to occur during periods of water deficits, their absence in the water balance method is again unlikely to have a significant impact on the estimation of root zone storage capacities (Bouaziz et al., 2022).

6.1.3 Statistical analysis

The Wilcoxon rank-sum test was used to analyze the trend in ΔEI, as discussed in Section 5.1. Some of the distributions of ΔEI were found to be normally distributed. And some of the distributions had equal sizes, but not all of them. This made it possible in some cases to use either the t-test or the Wilcoxon signed rank test instead of the Wilcoxon

rank-sum test. We chose to use only the Wilcoxon rank-sum test for all datasets to be consistent. The Wilcoxon rank-sum test is generally less powerful than the Wilcoxon signed-rank test or t-test. This is because the Wilcoxon rank-sum test makes use of less information in the data, as it only considers the ranks of the observations rather than their actual values. In contrast, the Wilcoxon signed-rank test and t-test make use of the actual data values.

We employed a multiple linear regression model to investigate the relationship between ΔEI and a set of climate indicators variables. However, this approach has limitations. Firstly, linear regression may not have been the most appropriate technique for the data, given the potential non-linearity and complexity of the relationship between our dependent and independent variables. Secondly, we included all of our explanatory variables in the model, even though some of them, such as potential evaporation and temperature, are known to be highly correlated.

6.1.4 Modelling process

The model has been calibrated by Bouaziz et al. (2022) for a range of possible parameters, and for this study, one of those sets has been used. However, the model has not been re-calibrated to obtain the best parameter set. The performance indicators for the model are reasonably good, but they could have been better if an additional calibration had been conducted. This is not a major concern since the aim of the analysis is to test the sensitivity of the model to changes in evaporation, specifically ΔEI, for which the current calibration should suffice.

The values of the root zone storage capacity were calculated for the areas including the nested subcatchments, so including all upstream areas. Therefore a correction is needed to adjust for those upstream areas and their value for $S_{\mathrm{r,max}}$. To make this correction, the geometric mean should be used instead of the arithmetic mean. However, when calculating both the geometric and arithmetic means, unrealistically large and small values of the

root zone storage capacity were obtained because the correction places too much weight on the subcatchment in question if its value is higher or lower than the nested subcatchments. This means that data issues, but also changes in evaporation, are given an extra high weighting due to the correction. For this reason, it was decided to use the uncorrected values for the root zone storage capacity in the model, so that the value for the subcatchment in the model actually represents the value for the entire upstream area. The decision to use the uncorrected values of root zone storage capacity in the model is not entirely realistic in closing the water balance. The aim was to investigate the effect of changes in evaporation on the hydrological response of the catchment, and using uncorrected values provided a better option for achieving this objective. While the use of uncorrected values may introduce some bias into the analysis, the potential benefits in terms of improved understanding of the hydrological response outweighed this concern.

6.2 Implications

6.2.1 Changes in root zone storage capacity

In this study, we used the Fu-method to assess its suitability for estimating root zone storage capacity in a changing climate. Specifically, we tested the assumption that the relationship between the aridity index and evaporative index, as represented in the Budyko framework, remains applicable in the future. To test this assumption, we analyzed catchment-specific omega values and examined whether the omega value for a given decade could be used to predict the evaporative index (EI) value for the subsequent decade, indicating that the relationship between the aridity index and evaporative index remains stable over time. By using this approach, we were able to assess the suitability of the Fu-method for estimating root zone storage capacity in a changing climate, as well as to investigate how catchment-specific characteristics affect the relationship between the aridity index and

evaporative index.For both CAMELS datasets, we confirm that the Fu method can be used with the same omega parameter when transitioning from one decade to the next. In the case of CAMELS GB, the median of the distribution in ΔEI for successive time steps is 0.00, +0.01, and 0.00. Meanwhile, in CAMELS USA, the median of the distribution in ΔEI for the decades is -0.01 and +0.04. The Meuse dataset displays a distinct pattern compared to the CAMELS datasets. For the initial time step, the median is 0.00, but there are fewer data points (n=9) due to the use of exclusively French data. For the second time step, which covers the entire study area, the median of ΔEI is -0.06, indicating a decrease in evaporation.

One possible explanation for the downward deviation in EI for the Meuse basin is the standing age of trees as the research by Fenicia et al. (2009) hypothesises that forest rotation has had a significant impact on the evaporation of the catchment. Specifically, the shift from deciduous to coniferous forest, and the increase in average forest age during the last decades of the 20th century, may have influenced the evaporation patterns observed in the Meuse dataset. While the relationship between stand age and evaporation is still under investigation, evidence suggests that young forests tend to evaporate more than mature forests. In the latter part of the 20th century, forest management practices underwent changes that led to an increase in the average age of standing forests in the Meuse basin area. Specifically, Dirkse and Daamen (2004) noted that in the Netherlands, the adoption of practices such as reduced clear-cutting and increased thinning resulted in a 10-year increase in the average age of trees between 1980 and 2001, from 43.3 to 53.3 years (Dirkse and Daamen, 2004; Fenicia et al., 2009). There are some studies that have shown that young forests tend to evaporate considerably more water than mature forests. Although the results of these studies may vary by climate and forest type, they suggest that forest age significantly affects the catchment water balance (Brown et al., 2005). Vertessy et al. (2001) estimated that annual transpiration declines by 66% when tree age increases from 15 to 240 years.

Scott and Lesch (1997) found that afforestation of a catchment with an average runoff of 236 mm/a led to the stream drying up completely after 12 years.

6.2.2 Climate indicators

The analysis reveals that the errors in EI (ΔEI) for the CAMELS GB dataset cannot be explained by climate indicators. For CAMELS USA, we see that a greater or lesser increase in error in EI can be linked to an increase or decrease in certain climate indicators. An increase in ΔEI can be linked to an increase in aridity index (ΔAI) and seasonality timing index (ΔST). A decrease in ΔEI can be linked to an increase in seasonality index (ΔSI) and temperature (ΔT). A decrease is also more likely to occur for catchments with a higher aridity index (AI). Nevertheless, these variables have low explanatory power together in the regression model (27%). For the Meuse, we see that catchments with a higher aridity index (AI) can be linked to an increase (or less negative decrease) in ΔEI. The most important variables that can be linked to a decrease in ΔEI are an increase in aridity index (ΔAI) and seasonality index (ΔSI). Also, catchments with a higher seasonality timing index (ST) can be linked to a more negative ΔEI. Together the indicators have very high explanatory power in the multiple linear regression model (97%). High explanatory power means that the regression model explains a large proportion of the variability in the data, but it does not guarantee that the model is accurate. With a small sample size (n = 45), the model may be overfitting to the data, meaning it is fitting the noise rather than the underlying pattern.

The study conducted by Van Noppen (2022) identified the most significant climate variables for explaining root zone storage capacities for the catchments in the Meuse basin upstream of Borgharen. The found variables include the Holdridge aridity index, phase shift of precipitation, and seasonal amplitude for potential evaporation. In contrast to the calculated root zone storage capacities used for the multiple linear regression model of Van Noppen, in this research there is already an account for the

aridity index when extrapolating the omega value and moving along the line within the Budyko framework. Moreover, both the phase shift of precipitation and the seasonal amplitude for potential evaporation are factors linked to the seasonality timing index and the seasonality index. From the analysis, the variables related to seasonality and aridity index appeared to be the most important explanatory variables, which is consistent with the findings of Van Noppen (2022).

6.2.3 Effect on the streamflow

When examining the impact on streamflow, four scenarios were considered. The A-scenarios were formed by considering the historical trends observed in the Meuse hydro-meteorological data. The scenarios based on the evaporation trends observed in the Meuse data result in less evaporation during the summer months (May, June, July) in a range of 0 to -22% with medians of -4% and -6%, and an increase in streamflow during the autumn months (September, October, November) in a range of 0 to +48%, with medians of +7% and +12%. These findings contrast with those of Bouaziz et al. (2022), who found that a more pronounced climatic seasonality with warmer summers under 2K global warming resulted in a streamflow decrease of up to 15% in autumn, associated with up to 14% higher summer evaporation. For comparison with the global warming simulation studies, we find that the period over which this study was conducted is relatively short, and thus, the effects of the temperature changes may not have fully manifested. Furthermore, the model results indicating lower summer evaporation and higher autumn streamflow are driven by the ΔEI derived from historical data. It is possible that the increasing standing age of the trees, as discussed in Fenicia et al. (2009), is responsible for this observed decrease in the evaporative index. The short-term effects of tree standing age may mask long-term global warming impacts, making it difficult to assess climate change consequences.

On the other hand, the scenarios based on evaporation trends observed in all combined data (Meuse, CAMELS GB, CAMELS USA) result in relatively symmetric changes around zero for both the evaporation during summer months of between -7% and +5% with medians of 0%, and in streamflow in autumn months between -11% and +10% with medians of -1%. Timing plays an important role in the changes in streamflow as the effects on maximum (Q_{max}) and minimum flow (Q_{min}) were not equally substantial (approximately 1% compared to the reference run for the B-scenarios). The largest changes in streamflow occurred in September, October, November, and December. The maximum flow typically occurred slightly later in the year, which means that the potential increase in maximum flow is smaller than the change in streamflow. The potential decrease in streamflow occurs during the relatively dry months of May, June, and July, but slightly earlier than the driest months, namely July, August, and September.

6.3 Recommendations

Based on our findings, we recommend taking certain measures to improve the accuracy and reliability of predictions for the Meuse river basin. While the Fu-method can be utilised with the same omega parameter for large sample datasets when transitioning from one decade to the next, caution is advised when applying this method to the Meuse river basin due to the potential for a deviation in the evaporative index of -0.06. To address this issue, we propose several approaches that can help to increase confidence in the predictions for this region. Firstly, we suggest monitoring changes in land use using satellite imagery, which can help to identify any differences in vegetation cover that could affect the prediction accuracy. Secondly, it is important to take into account the standing age of trees, as this can also impact evaporation. It is worth noting that the average standing age of trees can be influenced by policy decisions, such as forest management practices and reforestation efforts. By implementing these recommendations, we believe that the accuracy and reliability of predictions for the Meuse river basin can be improved, thereby providing the Fu-method as a valuable tool for water management.

7　Conclusions

The non-stationarity of hydrological systems in response to a changing climate is a well-recognised challenge in hydrology (Blöschl et al., 2017; Bouaziz et al., 2020; Ponds, 2022; Van Noppen, 2022). Of particular concern is the impact of changing vegetation and root zone storage capacity, which is difficult to quantify and model in hydrological models. To address this challenge, the use of non-stationary root zone storage capacities has been identified as an important step towards more accurate hydrological models. This study examines the effects of long-term climate variability on root zone storage capacity and its resulting consequences on hydrological response. By utilizing the method of Fu (1981), we determine whether the root zone storage capacity has significantly changed and evaluate the sensitivity of hydrological model predictions to these changes. We explain the changes in root zone storage capacity and evaporation using various climate indicators. Four model scenarios are identified, and for each scenario, historical changes in root zone storage capacity are compared to a reference scenario without changes.

For both CAMELS datasets, we confirm that the Fu method can be utilised with the same omega parameter when transitioning from one decade to the next, indicating small differences in root zone storage capacity. However, for the Meuse data, we observe a downward trend where actual evaporation is smaller than expected based on the Fu method, indicating that the root zone storage capacity has changed. The downward trend in actual evaporation compared to the expected evaporation suggests that caution should be exercised when applying the Fu method, with consideration given to a deviation in the evaporative index of approximately -0.06. A possible explanation for this trend of decreasing evaporation is the standing age of the trees, according to the hypothesis put forward by Fenicia et al. (2009). In the latter part of the 20th century, forest management practices underwent changes that resulted in an increase in the average age of standing forests. The relationship between stand age and evaporation is still being studied, but current evidence suggests that young forests generally have a higher rate of evaporation compared to mature forests.

We have implemented historical changes in evaporation as altered root zone storage capacity in the wflow_flextopo model in four different scenarios. The A-scenarios are based on the evaporation trends observed in the Meuse data, with model results indicating less evaporation during the summer months (May, June, July) with a range of 0 to -22%, and an increase in streamflow during the autumn months (September, October, November) with a range of 0 to +48%. On the other hand, the B-scenarios are based on evaporation trends observed in all combined datasets, including Meuse, CAMELS GB, and CAMELS USA. Implementing these trends in the model results in a change in evaporation during summer months with a range of -7% to +5%, and a change in autumn flow with a range of -11% to +10%. The greatest increases and decreases in flow occur during the period preceding the annual high and low flow periods.

The results of this study have important implications for water management, as they shed light on the observed trends in global water balance data and anticipated changes in future evaporation rates. Specifically, we have identified a trend in the Meuse river over the past two decades and examined its potential impact on the hydrological response if it were to persist in the future. The trend we observed differs from what is predicted by global warming scenarios. This could be due to the effect of changes in standing age of trees, which may outweigh the effects of temperature increase on a short-term basis. Furthermore, our study provides valuable insights into the potential effects of trends seen in other large sample datasets, which reflect global trends in evaporation rates. However, it is important to acknowledge that while these trends may be primarily associated with climate variability, human activities such as land use changes and deforestation can also significantly impact evaporation rates.

The effect of climate variability on the root zone storage capacity

References

N. Addor, A. J. Newman, N. Mizukami, and M. P. Clark. The camels data set: catchment attributes and meteorology for large-sample studies. Hydrology and Earth System Sciences, 21(10): 5293–5313, 2017.

R. G. Allen, L. S. Pereira, D. Raes, M. Smith, et al. Crop evapotranspiration-guidelines for computing crop water requirements-fao irrigation and drainage paper 56. Fao, Rome, 300(9):D05109, 1998.

W. R. Berghuijs and R. A. Woods. A simple framework to quantitatively describe monthly precipitation and temperature climatology. International Journal of Climatology, 36(9):3161–3174, 2016.

W. R. Berghuijs, M. Sivapalan, R. A. Woods, and H. H. Savenije. Patterns of similarity of seasonal water balances: A window into streamflow variability over a range of time scales. Water Resources Research, 50(7):5638–5661, 2014.

G. Blöschl, J. Hall, J. Parajka, R. A. Perdigão, B. Merz, B. Arheimer, G. T. Aronica, A. Bilibashi, O. Bonacci, M. Borga, et al. Changing climate shifts timing of european floods. Science, 357 (6351):588–590, 2017.

L. Bouaziz, A. Weerts, J. Schellekens, E. Sprokkereef, J. Stam, H. Savenije, and M. Hrachowitz. Redressing the balance: quantifying net intercatchment groundwater flows. Hydrology and Earth System Sciences, 22(12):6415–6434, 2018.

L. J. Bouaziz, S. C. Steele-Dunne, J. Schellekens, A. H. Weerts, J. Stam, E. Sprokkereef, H. H. Winsemius, H. H. Savenije, and M. Hrachowitz. Improved understanding of the link between catchment-scale vegetation accessible storage and satellite-derived soil water index. Water Resources Research, 56(3):e2019WR026365, 2020.

L. J. Bouaziz, E. E. Aalbers, A. H. Weerts, M. Hegnauer, H. Buiteveld, R. Lammersen, J. Stam, E. Sprokkereef, H. H. Savenije, and M. Hrachowitz. The importance of ecosystem adaptation on hydrological model predictions in response to climate change. Hydrology and Earth System Sciences Discussions, 2021:1–39, 2021.

L. J. Bouaziz, E. E. Aalbers, A. H. Weerts, M. Hegnauer, H. Buiteveld, R. Lammersen, J. Stam, E. Sprokkereef, H. H. Savenije, and M. Hrachowitz. Ecosystem adaptation to climate change: the sensitivity of hydrological predictions to time-dynamic model parameters. Hydrology and Earth System Sciences, 26(5):1295–1318, 2022.

A. E. Brown, L. Zhang, T. A. McMahon, A. W. Western, and R. A. Vertessy. A review of paired catchment studies for determining changes in water yield resulting from alterations in vegetation. Journal of hydrology, 310(1-4):28–61, 2005.

M. I. Budyko. The heat balance of the earth's surface. Soviet Geography, 2(4):3–13, 1961.

R. C. Cornes, G. van der Schrier, E. J. van den Besselaar, and P. D. Jones. An ensemble version of the e-obs temperature and precipitation data sets. Journal of Geophysical Research: Atmospheres, 123(17):9391–9409, 2018.

G. Coxon, N. Addor, J. P. Bloomfield, J. Freer, M. Fry, J. Hannaford, N. J. Howden, R. Lane, M. Lewis, E. L. Robinson, et al. Camels-gb: hydrometeorological time series and landscape attributes for 671 catchments in great britain. Earth System Science Data, 12(4):2459–2483, 2020.

T. de Boer-Euser. Added value of distribution in rainfall-runoff models for the meuse basin. 2017.

T. de Boer-Euser, H. K. McMillan, M. Hrachowitz, H. C. Winsemius, and H. H. Savenije. Influence of soil and climate on root zone storage capacity. Water Resources Research, 52(3):2009–2024, 2016.

M. De Wit, B. Van Den Hurk, P. Warmerdam, P. Torfs, E. Roulin, and W. Van Deursen. Impact of climate change on low-flows in the river meuse. Climatic change, 82:351–372, 2007.

G. Dirkse and W. Daamen. Dutch forest monitoring network, design and results. Community Ecology, 5(1):115–120, 2004.

H. Dixon, J. Hannaford, and M. J. Fry. The effective management of national hydrometric data: experiences from the united kingdom. Hydrological Sciences Journal, 58(7):1383–1399, 2013.

D. Eilander, W. Van Verseveld, D. Yamazaki, A. Weerts, H. C. Winsemius, and P. J. Ward. A hydrography upscaling method for scale-invariant parametrization of distributed hydrological models. Hydrology and Earth System Sciences, 25(9): 5287–5313, 2021.

European Environment Agency. Corine land cover (clc) 2018, version 2020 20u1, 2018. URL https://land.copernicus.eu/pan-european/\corine-land-cover/.

J. A. Falcone. Gages-ii: Geospatial attributes of gages for evaluating streamflow. Technical report, US Geological Survey, 2011.

J. A. Falcone, D. M. Carlisle, D. M. Wolock, and M. R. Meador. Gages: A stream gage database for evaluating natural and altered flow conditions in the conterminous united states: Ecological archives e091-045. Ecology, 91(2):621–621, 2010.

Y. Fan, G. Miguez-Macho, E. G. Jobbágy, R. B. Jackson, and C. Otero-Casal. Hydrologic regulation of plant rooting depth. Proceedings of the National Academy of Sciences, 114(40):10572–10577, 2017.

F. Fenicia, H. Savenije, and Y. Avdeeva. Anomaly in the rainfall-runoff behaviour of the meuse catchment. climate, land-use, or land-use management? Hydrology and Earth System Sciences, 13(9):1727–1737, 2009.

B. Fu. On the calculation of the evaporation from land surface. Sci. Atmos. Sin, 5(1):23–31, 1981.

H. Gao, M. Hrachowitz, S. Schymanski, F. Fenicia, N. Sriwongsitanon, and H. Savenije. Climate controls how ecosystems size the root zone storage capacity at catchment scale. Geophysical Research Letters, 41(22):7916–7923, 2014.

S. Gharari, M. Hrachowitz, F. Fenicia, and H. Savenije. Hydrological landscape classification: investigating the performance of hand based landscape classifications in a central european meso-scale catchment. Hydrology and Earth System Sciences, 15(11):3275–3291, 2011.

P. Guhathakurta and E. Saji. Detecting changes in rainfall pattern and seasonality index vis-à-vis increasing water scarcity in maharashtra. Journal of Earth System Science, 122(3):639–649, 2013.

J. Hannaford. Development of a strategic data management system for a national hydrological database, the uk national river flow archive. In Hydroinformatics: (In 2 Volumes, with CD-ROM), pages 637–644. World Scientific, 2004.

D. R. Helsel and R. M. Hirsch. Statistical methods in water resources, volume 49. Elsevier, 1992.

P. Hiemstra and R. Sluiter. Interpolation of makkink evaporation in the netherlands. 2011.

J. Hooghart and W. Lablans. Van penman naar makkink: een nieuwe berekeningswijze voor de klimatologische verdampingsgetallen. De Bilt, Royal Netherlands Meteorological Institute (KNMI), De Bilt, the Netherlands, 745, 1988.

M. N. Hough and R. J. A. Jones. The united kingdom meteorological office rainfall and evaporation calculation system: Morecs version 2.0-an overview. Hydrology and Earth System Sciences, 1(2):227–239, 1997. doi: 10.5194/hess-1-227-1997.

M. Hrachowitz, M. Stockinger, M. Coenders-Gerrits, R. van der Ent, H. Bogena, A. Lücke, and C. Stumpp. Reduction of vegetation-accessible water storage capacity after deforestation affects catchment travel time distributions and increases young water fractions in a headwater catchment. Hydrology and earth system sciences, 25(9):4887–4915, 2021.

F. Jaramillo, N. Cory, B. Arheimer, H. Laudon, Y. Van Der Velde, T. B. Hasper, C. Teutschbein, and J. Uddling. Dominant effect of increasing forest biomass on evapotranspiration: interpretations

of movement in budyko space. Hydrology and Earth System Sciences, 22(1):567–580, 2018.

S. Jin, L. Yang, P. Danielson, C. Homer, J. Fry, and G. Xian. A comprehensive change detection method for updating the national land cover database to circa 2011. Remote sensing of environment, 132:159–175, 2013.

V. Keller, M. Tanguy, I. Prosdocimi, J. Terry, O. Hitt, S. Cole, M. Fry, D. Morris, and H. Dixon. Ceh-gear: 1 km resolution daily and monthly areal rainfall estimates for the uk for hydrological and other applications. Earth System Science Data, 7(1):143–155, 2015.

H. K. McMillan, I. K. Westerberg, and T. Krueger. Hydrological data uncertainty and its implications. Wiley Interdisciplinary Reviews: Water, 5(6):e1319, 2018.

R. Merz, J. Parajka, and G. Blöschl. Time stability of catchment model parameters: Implications for climate impact analyses. Water resources research, 47(2), 2011.

Ministère de l'Ecologie, du Développement Durable et de l'Energie, Banque Hydro. Banque Hydro. URL http://hydro.eaufrance.fr/.

A. Newman, M. Clark, K. Sampson, A. Wood, L. Hay, A. Bock, R. Viger, D. Blodgett, L. Brekke, J. Arnold, et al. Development of a large-sample watershed-scale hydrometeorological data set for the contiguous usa: data set characteristics and assessment of regional variability in hydrologic model performance. Hydrology and Earth System Sciences, 19(1):209–223, 2015.

R. Nijzink, C. Hutton, I. Pechlivanidis, R. Capell, B. Arheimer, J. Freer, D. Han, T. Wagener, K. McGuire, H. Savenije, et al. The evolution of root-zone moisture capacities after deforestation: a step towards hydrological predictions under change? Hydrology and Earth System Sciences, 20(12):4775–4799, 2016.

J. Parajka, A. Blaschke, G. Blöschl, K. Haslinger, G. Hepp, G. Laaha, W. Schöner, H. Trautvetter, A. Viglione, and M. Zessner. Uncertainty contributions to low flow projections in austria. Hydrol Earth Syst Sci Discuss, 12:12395–12431, 2015.

M. Ponds. The effects of future climate-induced adaptation of root zone storage capacity on modelled streamflow dynamics. 2022.

C. D. Rennó, A. D. Nobre, L. A. Cuartas, J. V. Soares, M. G. Hodnett, and J. Tomasella. Hand, a new terrain descriptor using srtm-dem: Mapping terra-firme rainforest environments in amazonia. Remote Sensing of Environment, 112(9): 3469–3481, 2008.

Rijkswaterstaat. Water flow data at Albert canal. Online, 2022. URL https://waterinfo.rws.nl/.

E. L. Robinson, E. M. Blyth, D. B. Clark, J. Finch, and A. C. Rudd. Trends in atmospheric evaporative demand in great britain using high-resolution meteorological data. Hydrology and Earth System Sciences, 21(2):1189–1224, 2017.

H. H. Savenije and M. Hrachowitz. Hess opinions catchments as meta-organisms–a new blueprint for hydrological modelling. Hydrology and Earth System Sciences, 21(2):1107–1116, 2017.

D. F. Scott and W. Lesch. Streamflow responses to afforestation with eucalyptus grandis and pinus patula and to felling in the mokobulaan experimental catchments, south africa. Journal of Hydrology, 199(3-4):360–377, 1997.

Service Public de Wallonie. Bld du Nord 8-5000 Namur, Belgium, 2018.

Service Public de Wallonie: Direction générale opérationnelle de la Mobilité et des Voies hydrauliques, Département des Etudes et de l'Appui à la Gestion, Direction de la Gestion hydrologique. Rapport annuel 2018. Technical report, Service Public de Wallonie, Bld du Nord 8-5000 Namur, Belgium, 2018.

S. S. Shapiro and M. B. Wilk. An analysis of variance test for normality (complete samples). Biometrika, 52(3/4):591–611, 1965.

M. Tanguy, H. Dixon, I. Prosdocimi, D. Morris, and V. Keller. Gridded estimates of daily and monthly areal rainfall for the united kingdom (1890–2015)[ceh-gear]. NERC Environmental Information Data Centre, 10, 2016.

R. S. Teegavarapu. Changes and trends in precipitation extremes and characteristics: Links to climate variability and change. In Trends and changes in hydroclimatic variables, pages 91–148. Elsevier, 2019.

N. Thomson, L. Barrie, and M. Ayles. The meteorological office's rainfall and evaporation calculation system; morecs. met. Technical report, Office Hydrological Memorandum, 1981.

P. A. Troch, G. Carrillo, M. Sivapalan, T. Wagener, and K. Sawicz. Climate-vegetation-soil interactions and long-term hydrologic partitioning: signatures of catchment co-evolution. Hydrology and Earth System Sciences, 17(6):2209–2217, 2013.

M. Tu, M. J. Hall, P. J. de Laat, and M. J. de Wit. Extreme floods in the meuse river over the past century: aggravated by land-use changes? Physics and Chemistry of the Earth, Parts A/B/C, 30(4-5): 267–276, 2005.

E. Van Noppen. Climate-analogy mapping as a tool to develop a temporally-adaptive hydrological model of the meuse basin for more reliable predictions under change. 2022.

L. Van Voorst. Descriptor variables of the root zone storage capacity in canada. 2020.

W. v. Verseveld, M. Visser, H. Boisgontier, H. Bootsma, L. Bouaziz, J. Buitink, D. Eilander, and M. Hegnauer. Wflow.jl, 2022. URL https://doi.org/10.5281/zenodo.7040513.

R. A. Vertessy, F. G. Watson, K. Sharon, et al. Factors determining relations between stand age and catchment water balance in mountain ash forests. Forest Ecology and Management, 143(1-3):13–26, 2001.

D. Yamazaki, D. Ikeshima, J. Sosa, P. D. Bates, G. H. Allen, and T. M. Pavelsky. Merit hydro: a high-resolution global hydrography map based on latest topography dataset. Water Resources Research, 55 (6):5053–5073, 2019.

L. Zhang, K. Hickel, W. Dawes, F. H. Chiew, A. Western, and P. Briggs. A rational function approach for estimating mean annual evapotranspiration. Water resources research, 40(2), 2004.

Acknowlegdements

Completing this thesis has been an incredible journey, and all seven years at TU Delft have been enriching and fulfilling, providing me with unforgettable experiences and opportunities for personal and professional growth. During the first five years of my time at TU Delft, I lived on the Oudraadtweg, where I had the pleasure of meeting many wonderful people and forming lifelong friendships. I was a member of the Integrand and Debating boards, which gave me valuable experience and the opportunity to work with talented individuals. I worked in the communication department of TU Delft, where I gained skills and knowledge that have been beneficial to me throughout my academic and professional pursuits. During my minor in Madrid, I took a course on Environmental Engineering at the Universidad Pontificia Comillas, which helped me realize my passion for this field. As a result, I decided to switch from studying Technology Policy and Management to Civil Engineering, a decision that I am happy with.

I would like to express my gratitude to the following individuals for their support and guidance during the course of my thesis:

Firstly, I want to express my sincere gratitude to my thesis supervisor, Markus, who not only provided insightful feedback and enthusiasm but also motivated me to stay on track throughout the process. I am grateful for the many in-depth discussions we had. Markus was always available to answer my questions and provide guidance, and he never failed to encourage me to keep moving forward. I want to thank Eric and Jasper for their input from Rijkswaterstaat, their hospitality during our meetings at their office, and their explanations of the organization's operations. I also want to thank Laurène for her assistance with the model, her substantive comments, and her prompt help when I got stuck. And I want to thank Riccardo for his insightful comments and in-depth discussions during our thesis progress meetings, which greatly contributed to the scientific basis of my research.

A big thanks to the individuals who shared the Afstudeerhok with me - Rens, Charlie, David, Miek, Jan, Helena, Guus and Sjoerd. Our fun and sometimes long days working together were marked by insightful discussions. Special thanks to Mike for his valuable contributions to my thesis through thought-provoking discussions and helpful feedback.

My parents have been a constant source of support and encouragement, celebrating the milestones with me, sometimes with dinner at my favourite Italian restaurant. My father, Wubbo, was a great help with my thesis. He carefully proofread my work, making sure that not a single misplaced comma went unnoticed. My mother, Conny, provided valuable feedback on my presentation. Her attentive listening and attention to detail helped me improve the clarity of my story. I would like to thank my brothers and sister, Kasper, Joska, and Auke, for their support throughout my entire studies.

A big thanks to Karlijn and Pien, my roommates, for their support and friendship during the most challenging parts of my thesis journey. Our cozy dinners together provided a much-needed break from work, and their willingness to listen to my experiences, as well as celebrate important moments with me, meant a lot to me. Also, thanks to my former housemates Renske, Jolien, Geerte, and Elisa for their support and fun "Rotterdampas-uitjes" during the initial stage of my thesis. A special thanks to Zori for her encouragement during the busy periods and to Joris for providing me with comments on the final document.

I want to thank Daan for always being there for me, planning fun activities and supporting me in everything I do. I am also grateful for the support and kind messages of Daan's parents, Wendy and Marcel, and his grandparents, Willem and Sylvia.

Completing this thesis has been both challenging and rewarding, and I am happy with the outcome. Enjoy reading!

SUPPLEMENTARY MATERIAL TO:

The Effect of Climate Variability on the Root Zone Storage Capacity

BY

NIENKE TEMPEL

Appendix A: Calculation Potential Evaporation

The following correction is executed by Van Noppen (2022). For the CAMELS-USA data set the Makkink equation that has been used is given by Eq. 23 (Hiemstra and Sluiter, 2011).

$$ET_{ref} = 0.65 * \frac{s}{s + \gamma} \frac{K}{\lambda * \rho} \tag{23}$$

Where ET_{ref} = potential evaporation $[md^{-1}]$, γ = psychrometric constant (at sea level $0.066kPa°C^{-1}$), s = the slope of the curve of saturation water vapor pressure $[kPa°C^{-1}]$, K = daily incoming short-wave radiation $[Jm^{-2}day^{-1}]$, λ = Heat of vaporization of water $[Jkg^{-1}]$ and ρ = 1000 kg m^{-3} = bulk density of water. The slope of the curve of saturation water vapor pressure is calculated with Eq. 24 and e_s is the saturated vapor pressure is calculated with Eq. 25.

$$slope = \frac{7.5 * 237.3}{(237.3 + T)^2} * \log 10 * e_s \tag{24}$$

$$e_s = 0.6107 * 10^{\frac{7.5*T_{Day}}{237.3+T_{Day}}} \tag{25}$$

The heat of vaporization is calculated with Eq. 26 and the psychrometric constant with Eq. 27.

$$\lambda = (2501 - 2.375 * T_{Day}) * 1000 \tag{26}$$

$$\gamma = 0.0646 + 0.00006 * T_{Day} \tag{27}$$

For CAMELS-GB the incoming short-wave radiation is provided in Wm^2 instead of in $Jm^{-2}day^{-1}$, therefore the previous method should be adjusted to these different units, as follows.

$$ET_{ref} = 0.65 * \frac{s}{s + \gamma} \frac{K}{\lambda} \tag{28}$$

Where ET_{ref} = potential evaporation $[md^{-1}]$, γ = psychrometric constant (at sea level 0.066 kPa°C^{-1}), s =the slope of the curve of saturation water vapor pressure $[kPa°C^{-1}]$, K =daily incoming short-wave radiation $[Jm^{-2}day^{-1}]$, and λ = Heat of vaporization of water $[Jkg^{-1}]$ The slope of the curve of saturation water vapor pressure is calculated with Eq. 29.

$$slope = \frac{abc}{(c + T)^2} * \exp \frac{bT}{c + T} \tag{29}$$

Where a = 6.1078 mbar, b = 17.294 $[-]$, c = 237.73°C, T = Temperature $[°C]$ The heat of vaporization and the psychrometric constant have been computed again with Eq. 26 and 27.

Appendix B: Overview of model structure
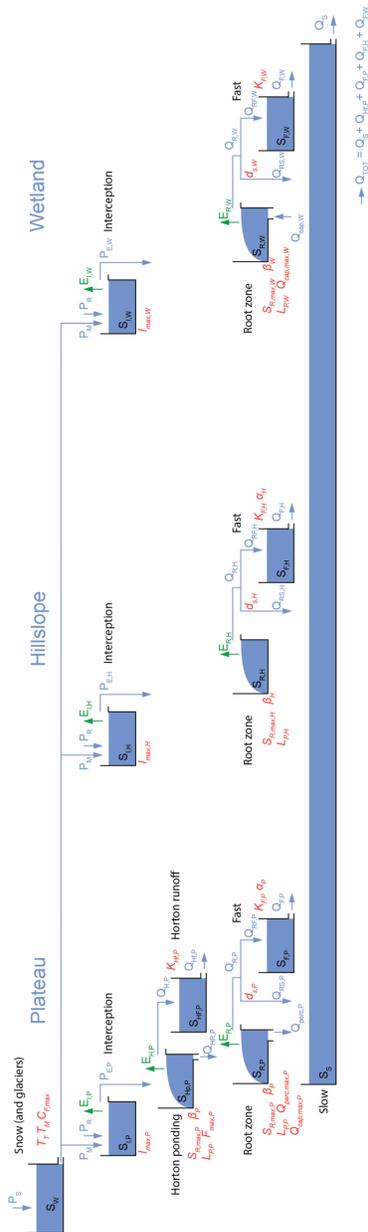
Figure 23: Overview of the wflow_flextopo model (Verseveld et al., 2022).

Appendix C. Normality plots
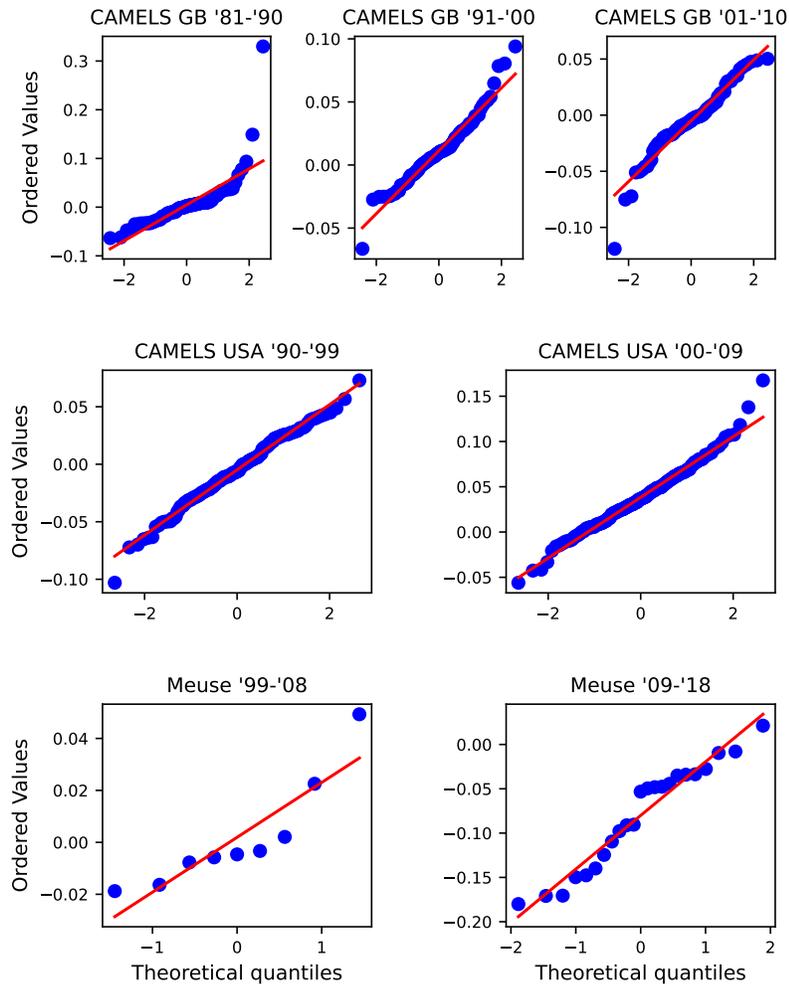
Figure 24: Test normality - QQ plots. If the data points fall along a straight line, the distribution is approximately normal. Deviations from a straight line indicate non-normality. Left-skewed data points suggest a left-skewed distribution, while right-skewed points suggest a right-skewed distribution.

Appendix D. Results Multiple Linear Regression

Table 6: The results of the multiple linear regression analysis. Each dataset indicates the significance and coefficient for each variable.

	Sign CAMELS GB	Coef CAMELS GB	Sign CAMELS USA	Coef CAMELS USA	Sign Meuse	Coef Meuse
ΔAI	0.047	0.199	0.153	0.089	0.0	-2.228
$\overline{P}_{annual}$	0.097	0.0	0.16	-0.0	0.991	0.0
$\Delta \overline{P}_{annual}$	0.079	0.0	0.812	-0.0	0.48	0.0
$\overline{E}_{p,annual}$	0.35	-0.0	0.872	0.0	0.335	-0.001
$\Delta \overline{E}_{p,annual}$	0.383	-0.0	0.771	0.0	0.563	-0.002
T	0.957	-0.0	0.81	-0.001	0.994	-0.0
ΔT	0.107	0.039	0.0	-0.052	0.008	0.34
SI	0.02	-0.247	0.513	0.036	0.0	3.375
ΔSI	0.121	0.144	0.002	-0.134	0.002	-1.257
ST	0.268	0.09	0.327	-0.023	0.173	-0.867
ΔST	0.544	-0.034	0.035	0.047	0.141	0.606
$Interstorm\ duration$	0.103	0.024	0.7	0.002	0.001	-0.41
$\Delta Interstorm\ duration$	0.195	-0.021	0.061	0.013	0.001	0.266

Appendix E. Histograms Error in EI grouped by climate indicators
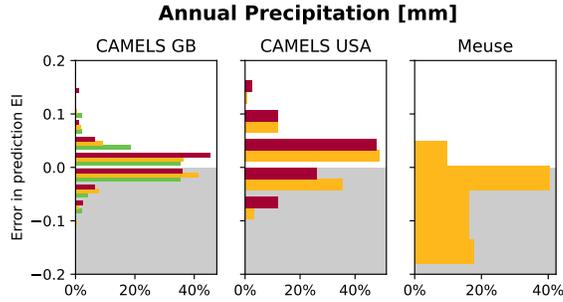
Figure 25: Error in prediction EI grouped by average annual precipitation. Green indicates low precipitation ($\overline{P}_{\mathrm{annual}} < 500$ mm), yellow indicates medium precipitation (500 mm $< \overline{P}_{\mathrm{annual}} <= 750$ mm), and red indicates high precipitation (750 mm $< \overline{P}_{\mathrm{annual}}$).
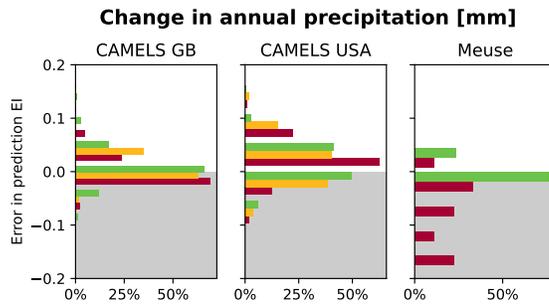
Figure 26: Error in prediction EI grouped by change in average annual precipitation, $\Delta\overline{P}_{\mathrm{annual}}$. Red indicates a decrease in average annual precipitation ($\Delta\overline{P}_{\mathrm{annual}} < -20$ mm), yellow indicates little or no change in average annual precipitation (-20 mm $< \Delta\overline{P}_{\mathrm{annual}} <= 20$ mm), and green indicates an increase in average mean precipitation (20 mm $< \Delta\overline{P}_{\mathrm{annual}}$).

Annual Potential Evaporation [mm]
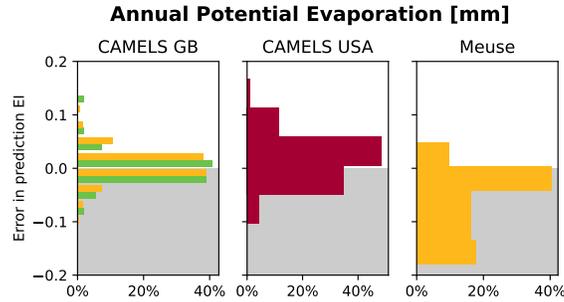
Figure 27: Error in prediction EI grouped by average annual potential evaporation. Green indicates low potential evaporation ($\overline{E}_{\mathrm{p,annual}} < 500$ mm), yellow indicates medium annual potential evaporation (500 mm $< \overline{E}_{\mathrm{p,annual}} <= 750$ mm), and red indicates high potential evaporation (750 mm $< \overline{E}_{\mathrm{p,annual}}$).

Change in annual evaporation [mm]
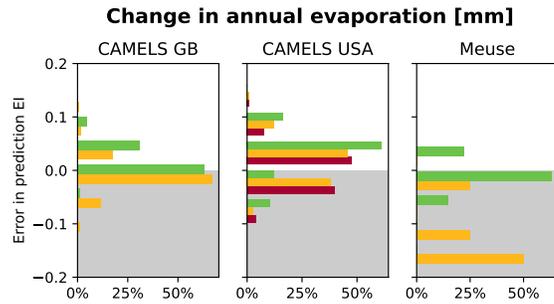
Figure 28: Error in prediction EI grouped by change in average annual potential evaporation, $\Delta\overline{E}_{\mathrm{p,annual}}$. Red indicates a decrease in average annual potential evaporation ($\Delta\overline{E}_{\mathrm{p,annual}} < -10$ mm), yellow indicates little or no change in average annual potential evaporation (-10 mm $< \Delta\overline{E}_{\mathrm{p,annual}} <= 10$ mm), and green indicates an increase in average annual potential evaporation (10 mm $< \Delta\overline{E}_{\mathrm{p,annual}}$).
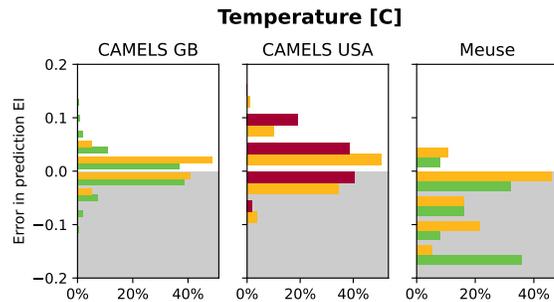
Temperature [C]

Figure 29: Error in prediction EI grouped by average temperature. Green indicates low temperature ($\overline{T} < 5$ C), yellow indicates medium temperature (5 C $< \overline{T} <= 10$ C), and red indicates high average temperature (5 C $< \overline{T}$).
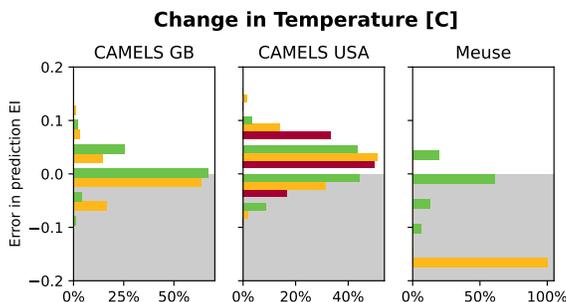
Figure 30: Error in prediction EI grouped by change in average temperature, $\Delta\overline{T}$. Red indicates a decrease in average temperature ($\Delta\overline{T}$ < -0.2 C), yellow indicates little or no change in average temperature (-0.2 C < $\Delta\overline{T}$ <= 0.2 C), and green indicates an increase in average temperature (0.2 C < $\Delta\overline{T}$).
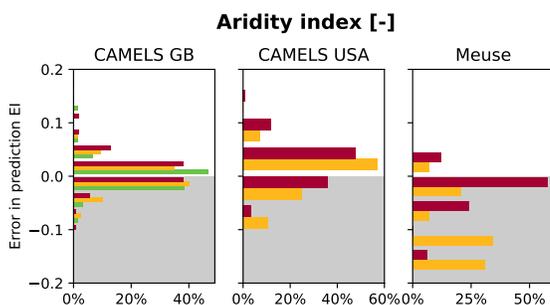
Figure 31: Error in prediction EI grouped by aridity index. Green indicates low aridity (AI < 0.33), yellow indicates medium aridity (0.33 < AI <= 0.66), and red indicates high level of aridity (0.66 < AI).
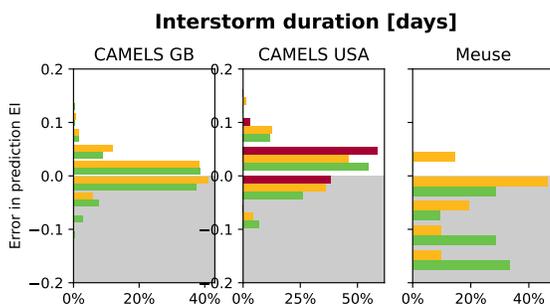
Figure 32: Error in prediction EI grouped by average interstorm duration. Green indicates short average interstorm duration (Interstorm duration < 4 days), yellow indicates medium average interstorm duration (4 days < Interstorm duration <= 6 days), and red indicates long interstorm duration (6 days < Interstorm duration).
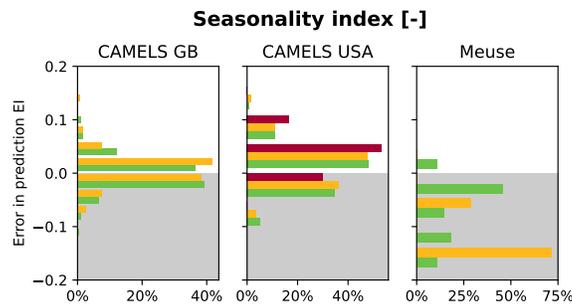
Figure 33: Error in prediction EI grouped by seasonality index. Green indicates low seasonality ($SI < 0.2$), yellow indicates medium seasonality ($0.2 < SI <= 0.4$), and red indicates high seasonality ($0.4 < SI$).
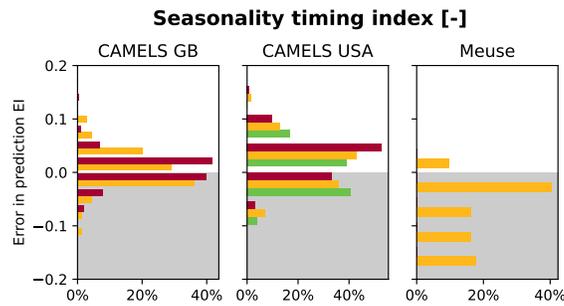
Figure 34: Error in prediction EI grouped by seasonality timing index. Green indicates negative seasonality timing ($ST < 0$), yellow indicates medium seasonality timing effects ($0 < ST <= 0.10$), and red indicates higher positive seasonality timing ($0.10 < ST$).
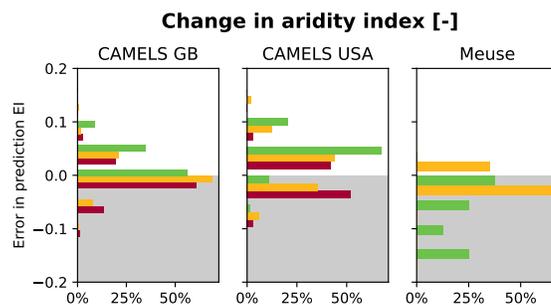
Figure 35: Error in prediction EI grouped by change in aridity index, ΔAI. Red indicates a decrease in aridity index ($\Delta AI < 0.05$), yellow indicates little or no change in aridity index ($0.05 < \Delta AI <= 0.05$), and green indicates an increase in aridity index ($0.05 < \Delta AI$).

Change in interstorm duration [days]
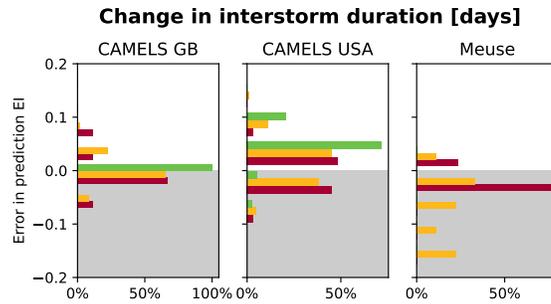
Figure 36: Error in prediction EI grouped by change in interstorm duration, ΔInterstorm duration. Red indicates a decrease in interstorm duration (ΔInterstorm duration < 0.5), yellow indicates little or no change in aridity index (0.5 < ΔInterstorm duration <= 0.5), and green indicates an increase in interstorm duration (0.5 < ΔInterstorm duration).

Change in seasonality index [-]
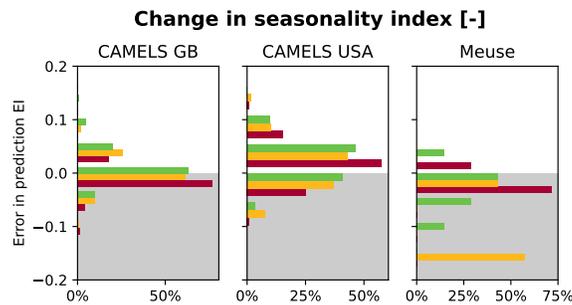
Figure 37: Error in prediction EI grouped by change in seasonality index, ΔSI. Red indicates a decrease in seasonality index (ΔSI < -0.02), yellow indicates little or no change in seasonality index (-0.02 < ΔSI <= 0.02), and green indicates an increase in seasonality index (0.02 < ΔSI).

Change in seasonality timing index [-]
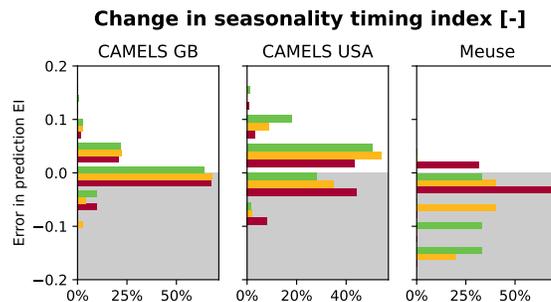
Figure 38: Error in prediction EI grouped by change in seasonality timing index, ΔST. Red indicates a decrease in seasonality timing index (ΔST < -0.02), yellow indicates little or no change in seasonality timing index (-0.02 < ΔST <= 0.02), and green indicates an increase in seasonality timing index (0.02 < ΔST).

Appendix F. Results Wilcoxon rank-sum tests

Table 7: Results wilxocon ranked sum test and descriptive statistics of ΔEI grouped per variable

Variable	Dataset	Group	n	mean	std	Sign level (1 vs 2)	Sign level (2 vs 3)
Annual precipitation [mm]	CAMELS GB	Pa ≤ 700	48	0.01	0.03	0.31	
		700 < Pa ≤ 1400	162	0.00	0.04		
		1400 < Pa	75	0.00	0.03		0.85
	CAMELS USA	Pa ≤ 700	10	0.00	0.01	0.11	
		700 < Pa ≤ 1400	286	0.02	0.04		
		1400 < Pa	42	0.01	0.05		0.32
	Meuse	700 < Pa ≤ 1400	32	-0.06	0.06		
Annual evaporation [mm]	CAMELS GB	Epa ≤ 500	54	0.01	0.05	0.66	
		500 < Epa ≤ 750	231	0.00	0.03		
	CAMELS USA	750 < Epa	338	0.02	0.04		
	Meuse	Epa < 500	32	-0.06	0.06		
Temperature [C]	CAMELS GB	T ≤ 10	246	0.00	0.04	0.54	
		10 < T ≤ 15	39	0.00	0.02		
	CAMELS USA	T ≤ 10	4	0.00	0.07	0.46	
		10 < T ≤ 15	282	0.02	0.04		
		15 < T	52	0.02	0.04		0.81
	Meuse	T ≤ 10	13	-0.07	0.07	0.11	
		10 < T ≤ 15	19	-0.04	0.05		
Aridity index [-]	CAMELS GB	AI ≤ 0.33	60	0.00	0.03	0.42	
		0.33 < AI ≤ 0.66	117	0.00	0.04		
		AI < 0.66	108	0.00	0.03		0.33
	CAMELS USA	0.33 < AI ≤ 0.66	28	0.01	0.04		0.30
		0.66 < AI	310	0.02	0.04		
	Meuse	0.33 < AI ≤ 0.66	15	-0.09	0.07		**0.00**
		0.66 < AI	17	-0.03	0.05		
Interstorm duration [days]	CAMELS GB	Is_dur ≤ 4	168	0.00	0.04	0.72	
		4 < is_dur ≤ 6	117	0.00	0.03		
	CAMELS USA	Is_dur ≤ 4	42	0.01	0.04	0.76	
		4 < is_dur ≤ 6	262	0.02	0.04		
		6 < is_dur	34	0.01	0.02		0.18
	Meuse	Is_dur ≤ 4	11	-0.09	0.06	**0.00**	
		4 < is_dur ≤ 6	21	-0.04	0.06		
Seasonality index [-]	CAMELS GB	SI ≤ 0.2	165	0.01	0.04	0.55	
		0.2 < SI ≤ 0.4	120	0.00	0.03		
	CAMELS USA	SI ≤ 0.2	170	0.02	0.04	0.88	
		0.2 < SI ≤ 0.4	138	0.02	0.04		
		0.4 < SI	30	0.02	0.03		0.25
	Meuse	SI ≤ 0.2	28	-0.05	0.06	**0.00**	
		0.2 < SI ≤ 0.4	4	-0.13	0.06		
Seasonality timing index [-]	CAMELS GB	0 < ST ≤ 0.1	69	0.01	0.04		0.09
		0.1 < ST	216	0.00	0.03		
	CAMELS USA	ST ≤ 0	54	0.01	0.04	0.80	
		0 < ST ≤ 0.1	70	0.02	0.04		
		0.1 < ST	214	0.02	0.04		0.70
	Meuse	0 < ST ≤ 0.1	32	-0.06	0.07		

Table 8: Results wilxocon ranked sum test and statistics of ΔEI grouped per change in variable

Variable	Dataset	Group	n	mean	std	Sign level (1 vs 2)	Sign level (2 vs 3)
Annual precipitation [mm]	CAMELS GB	$\Delta Pa \leq -20$	42	0.00	0.03	0.24	
		$-20 < \Delta Pa \leq 20$	57	0.01	0.02		
		$20 < \Delta Pa$	186	0.00	0.04		**0.01**
	CAMELS USA	$\Delta Pa \leq -20$	118	0.04	0.03	**0.01**	
		$-20 < \Delta Pa \leq 20$	52	0.02	0.05		
		$20 < \Delta Pa$	168	0.00	0.03		**0.01**
	Meuse	$\Delta Pa \leq -20$	18	-0.07	0.07		
		$20 < \Delta Pa$	17	0.00	0.02	**0.00**	
Annual evaporation [mm]	CAMELS GB	$\Delta Epa \leq -10$	1	-	-	0.21	
		$-10 < \Delta Epa \leq 10$	197	0.00	0.04		
		$10 < \Delta Epa$	87	0.01	0.03		**0.00**
	CAMELS USA	$Epa -10$	103	0.02	0.04	0.97	
		$-10 < \Delta Epa \leq 10$	186	0.02	0.04		
		$10 < \Delta Epa$	49	0.02	0.04		0.11
	Meuse	$-10 < \Delta Epa < 10$	8	-0.12	0.07		
		$10 < Epa$	27	-0.01	0.03		**0.00**
Temperature [C]	CAMELS GB	$-0.2 < \Delta T \leq 0.2$	97	0.00	0.05		0.15
		$0.2 < \Delta T$	188	0.00	0.03		
	CAMELS USA	$\Delta T \leq -0.2$	18	0.05	0.04	**0.02**	
		$-0.2 < \Delta T \leq 0.2$	205	0.02	0.04		
		$0.2 < \Delta T$	115	0.00	0.03		**0.00**
	Meuse	$-0.2 < \Delta T \leq 0.2$	4	-0.18	0.01		
		$0.2 < \Delta T$	32	-0.01	0.03		**0.00**
Aridity index [-]	CAMELS GB	$\Delta AI \leq -0.05$	66	0.00	0.05	0.24	
		$-0.05 < \Delta AI \leq 0.05$	196	0.00	0.03		
		$0.05 < \Delta AI$	23	0.02	0.03		0.09
	CAMELS USA	$AI \leq -0.05$	98	0.00	0.03	**0.00**	
		$-0.05 < \Delta AI \leq 0.05$	166	0.02	0.04		
		$0.05 < \Delta AI$	74	0.03	0.03		**0.00**
	Meuse	$\Delta AI < -0.05$	2	-0.02	0.00	0.05	
		$-0.05 < \Delta AI \leq 0.05$	17	0.01	0.02		
		$0.05 < \Delta is_d ur$	16	-0.08	0.06		**0.00**
Interstorm duration [days]	CAMELS GB	$\Delta Is\_dur \leq -0.5$	9	0.01	0.04	0.45	
		$-0.5 < \Delta is\_dur \leq 0.5$	274	0.00	0.03		
		$0.05 < \Delta is_d ur$	2	0.00	0.00		0.80
	CAMELS USA	$\Delta Is\_dur \leq -0.5$	31	0.00	0.03	**0.03**	
		$-0.5 < \Delta is\_dur \leq 0.5$	268	0.02	0.04		
		$0.05 < \Delta is_d ur$	39	0.03	0.03		**0.00**
	Meuse	$\Delta Is\_dur \leq -0.5$	17	0.00	0.02		
		$-0.5 < \Delta is\_dur \leq 0.5$	18	-0.07	0.07	**0.00**	
Seasonality index [-]	CAMELS GB	$\Delta SI \leq -0.02$	73	0.00	0.03	0.43	
		$-0.02 < \Delta SI \leq 0.02$	112	0.00	0.03		
		$0.02 < \Delta SI$	100	0.01	0.05		0.99
	CAMELS USA	$\Delta SI \leq -0.02$	99	0.03	0.03	**0.00**	
		$-0.02 < \Delta SI \leq 0.02$	116	0.01	0.04		
		$0.02 < \Delta SI$	123	0.01	0.03		0.55
	Meuse	$\Delta SI \leq -0.02$	14	0.01	0.02	**0.01**	
		$-0.02 < \Delta SI \leq 0.02$	7	-0.10	0.09		
		$0.02 < \Delta SI$	14	-0.03	0.03		0.26
Seasonality timing index [-]	CAMELS GB	$\Delta ST \leq -0.02$	62	0.00	0.03	0.50	
		$-0.02 < \Delta ST \leq 0.02$	72	0.00	0.03		
		$0.02 < \Delta ST$	151	0.01	0.04		0.43
	CAMELS USA	$\Delta ST \leq -0.02$	122	0.00	0.04	**0.01**	
		$-0.02 < \Delta ST \leq 0.02$	46	0.02	0.03		
		$0.02 < \Delta ST$	170	0.03	0.04		0.10
	Meuse	$\Delta ST \leq -0.02$	19	-0.01	0.02	**0.00**	
		$-0.02 < \Delta ST \leq 0.02$	10	-0.06	0.06		
		$0.02 < \Delta ST$	6	-0.10	0.07		0.28

The effect of climate variability on the root zone storage capacity

Appendix G. Change in flow per catchment

The following images show the outcomes of the model concerning alterations in evaporation and streamflow for each catchment. The changes in evaporation (EA) and streamflow (Q) are represented in units of [mm/d]. To calculate the change, the difference between evaporation or streamflow and the reference run ($\Delta EI = 0$) was determined for each run. The results for all years and runs were then aggregated. The 90th and 10th percentiles are depicted in the lightly shaded area, while the slightly darker shaded area represents the 25th to 75th percentiles. The median is denoted by the black line.
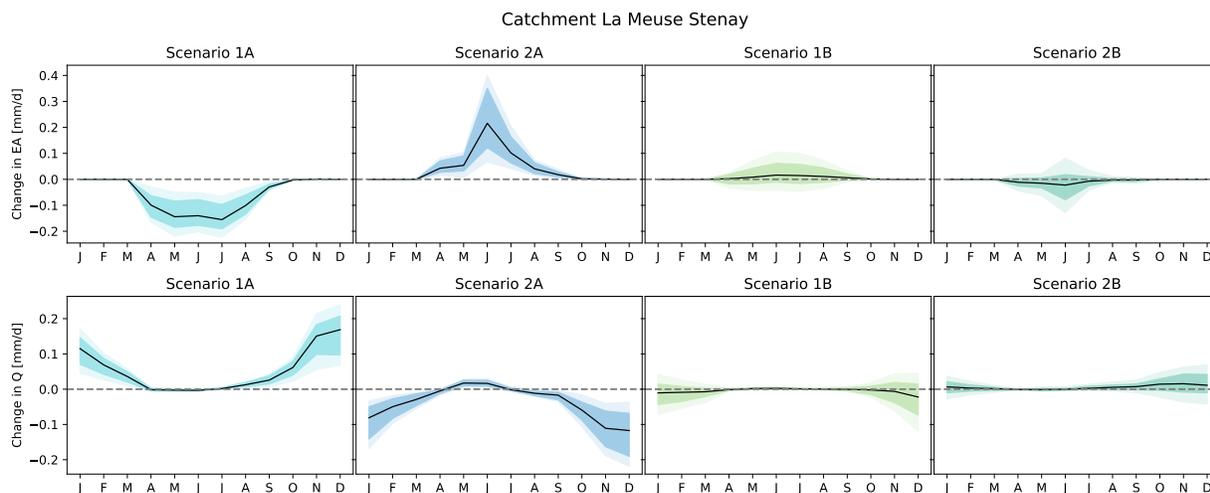
Figure 39: Change in evaporation (EA) and streamflow (Q), both in [mm/d] for La Meuse Stenay.
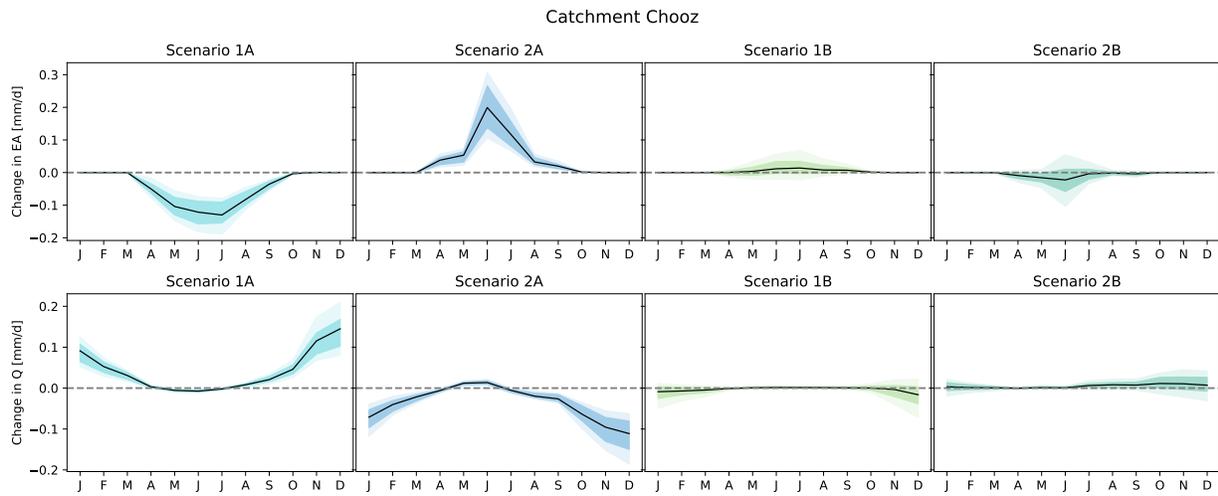
Figure 40: Change in evaporation (EA) and streamflow (Q), both in [mm/d] for Chooz.
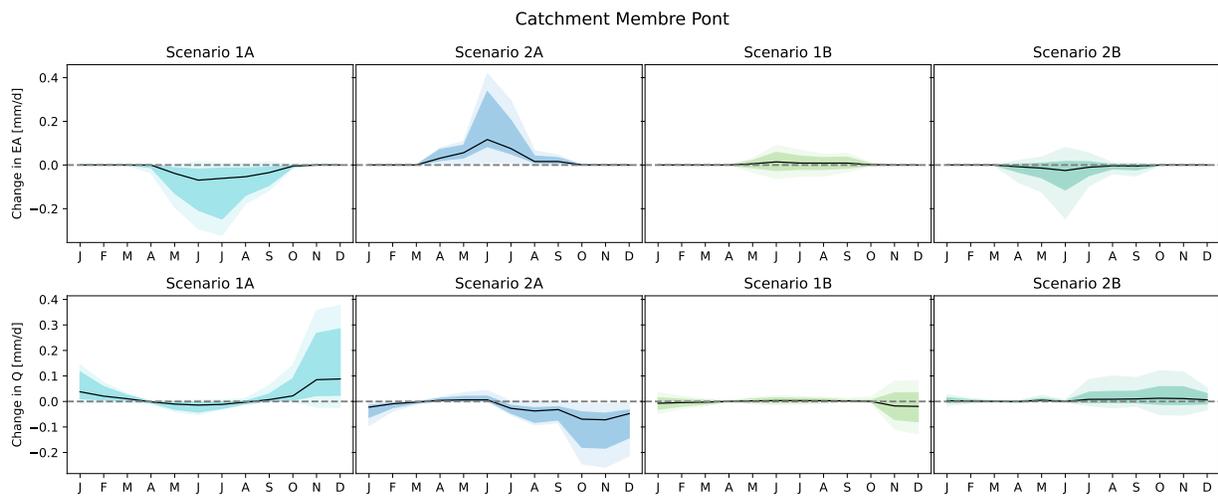
Figure 41: Change in evaporation (EA) and streamflow (Q), both in [mm/d] for Membre Pont.
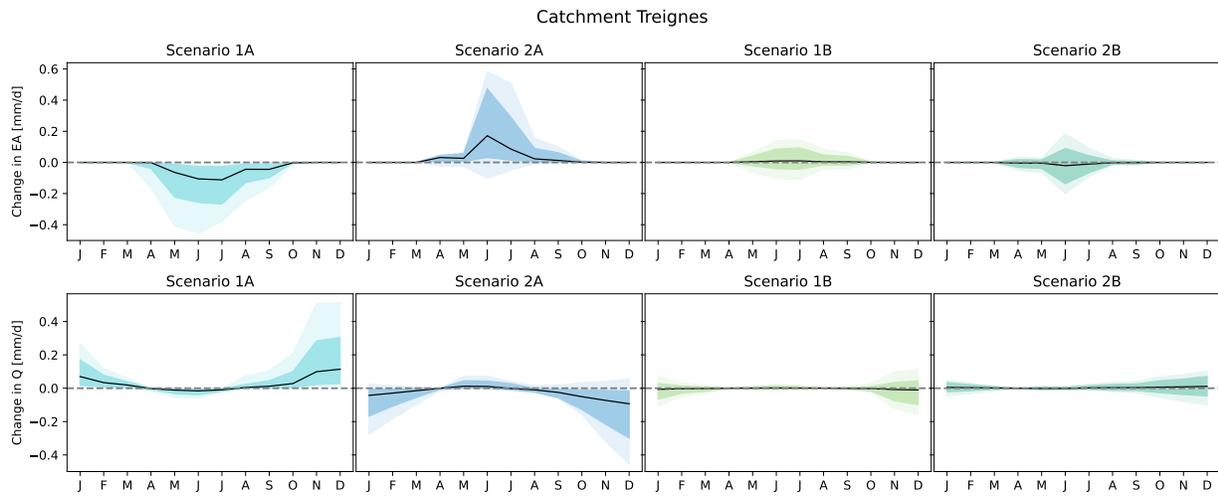
Figure 42: Change in evaporation (EA) and streamflow (Q), both in [mm/d] for Treignes.
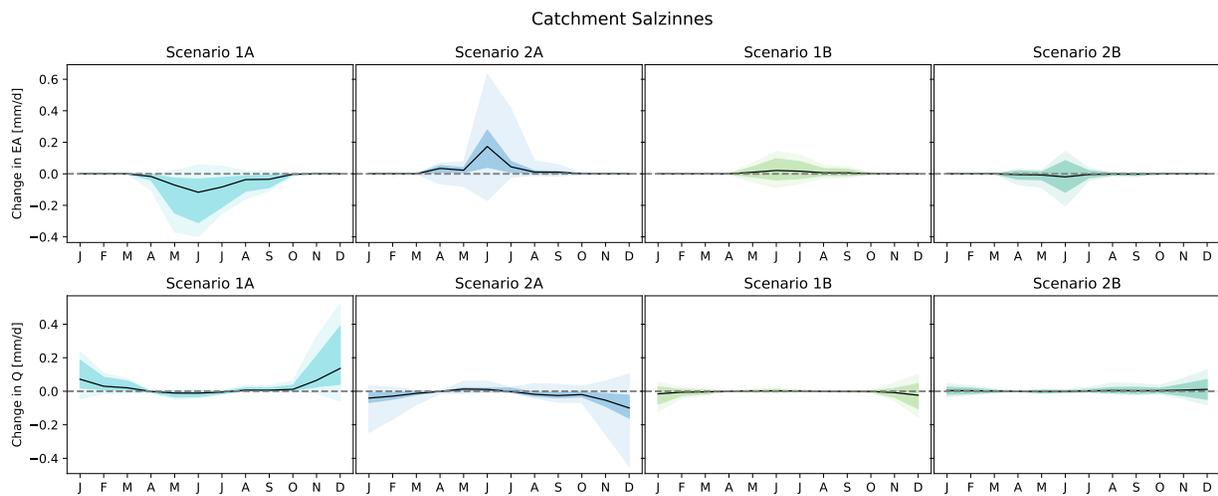
Figure 43: Change in evaporation (EA) and streamflow (Q), both in [mm/d] for Salzinnes.

Catchment Huccorgne
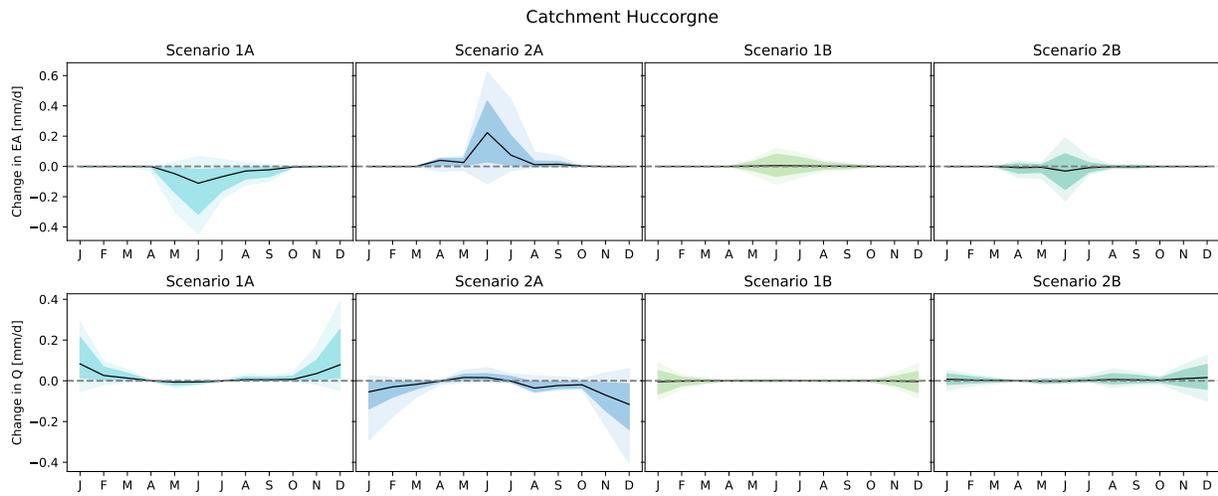
Figure 44: Change in evaporation (EA) and streamflow (Q), both in [mm/d] for Huccorgne.

Catchment Maastricht
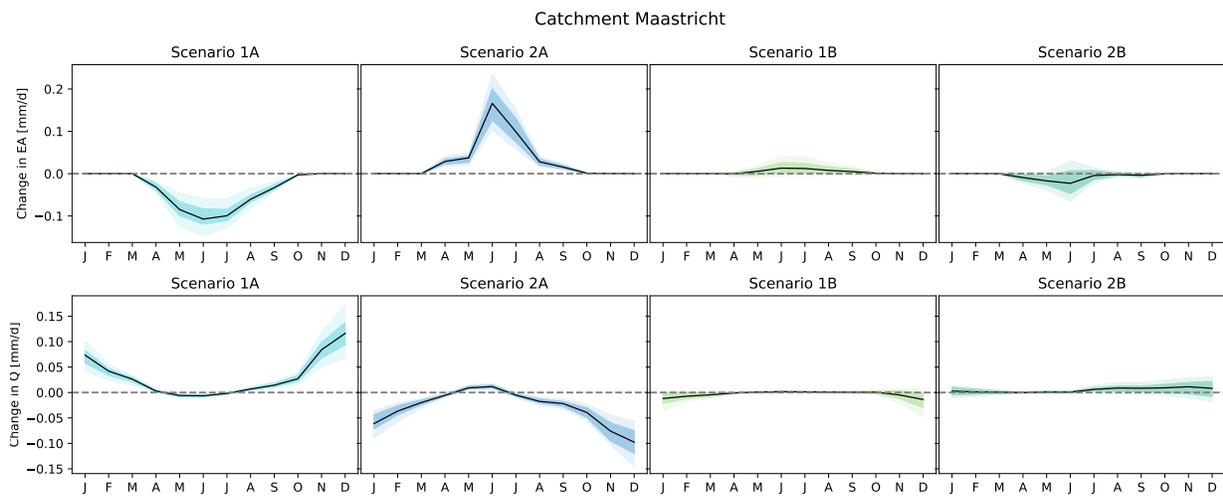
Figure 45: Change in evaporation (EA) and streamflow (Q), both in [mm/d] for Maastricht.

Catchment La Bar Cheveuges
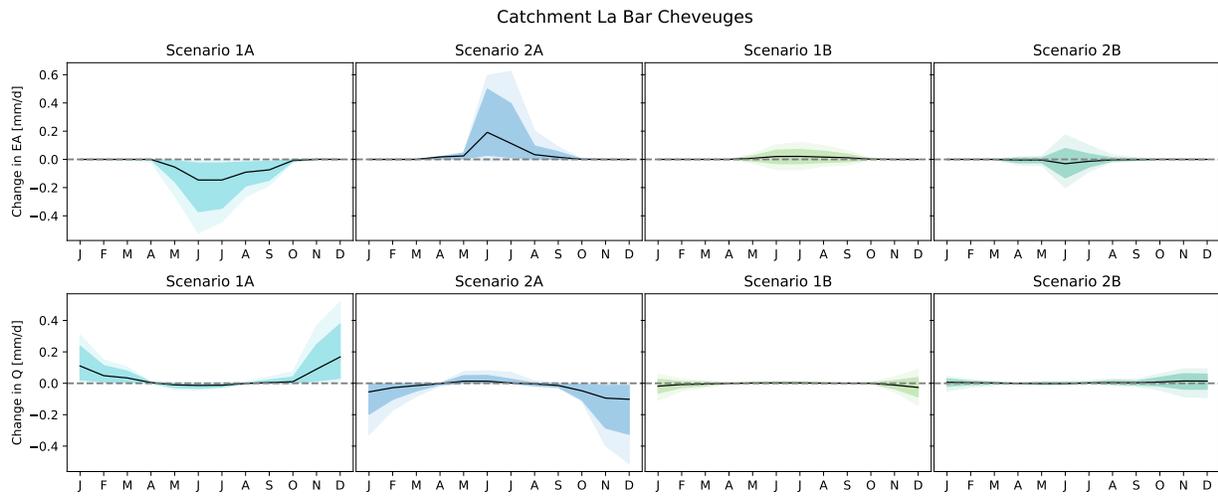
Figure 46: Change in evaporation (EA) and streamflow (Q), both in [mm/d] for La Bar Cheveuges.

Catchment La Vence la Francheville
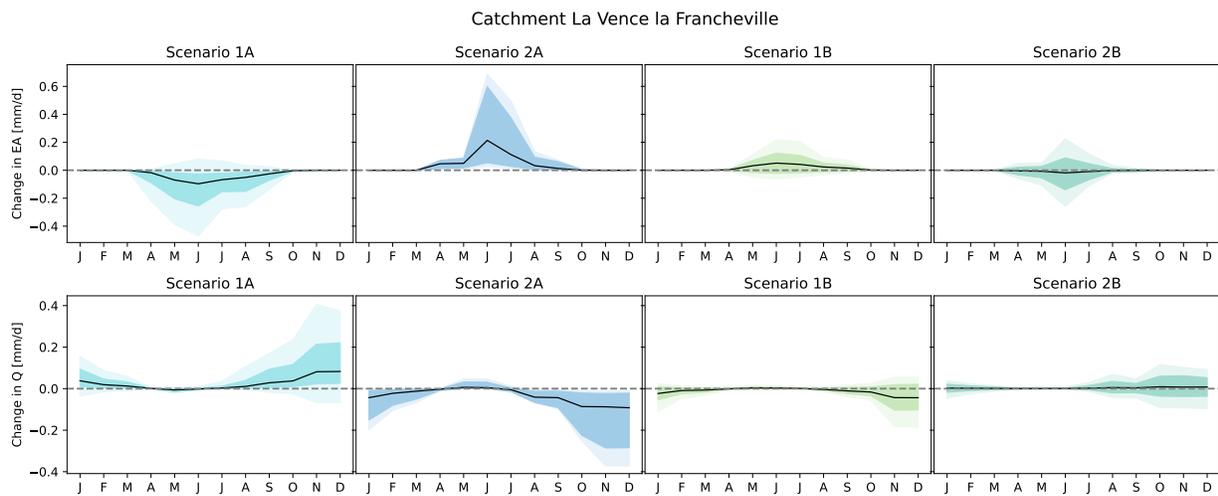
Figure 47: Change in evaporation (EA) and streamflow (Q), both in [mm/d] for La Vence la Francheville.

Catchment La Meuse Saint-Mihiel
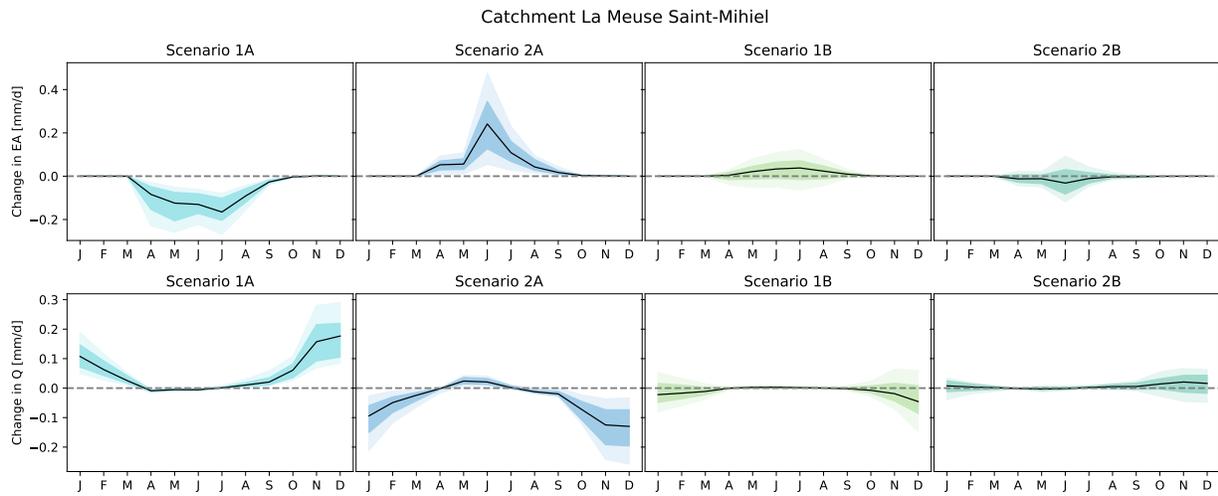
Figure 48: Change in evaporation (EA) and streamflow (Q), both in [mm/d] for La Meuse Saint Mihiel.

Catchment La Chiers Carignan
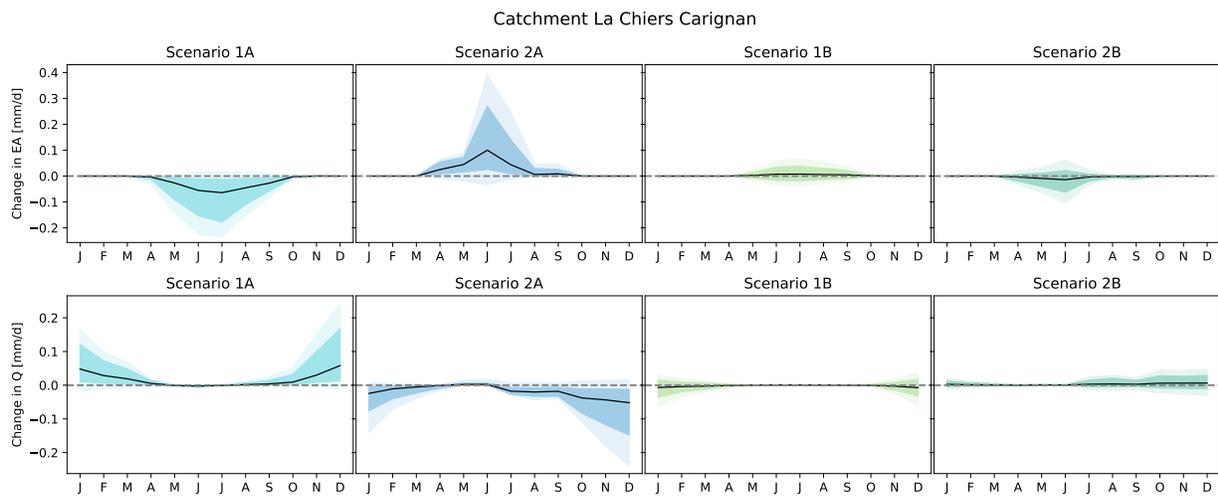
Figure 49: Change in evaporation (EA) and streamflow (Q), both in [mm/d] for La Chiers Carignan.
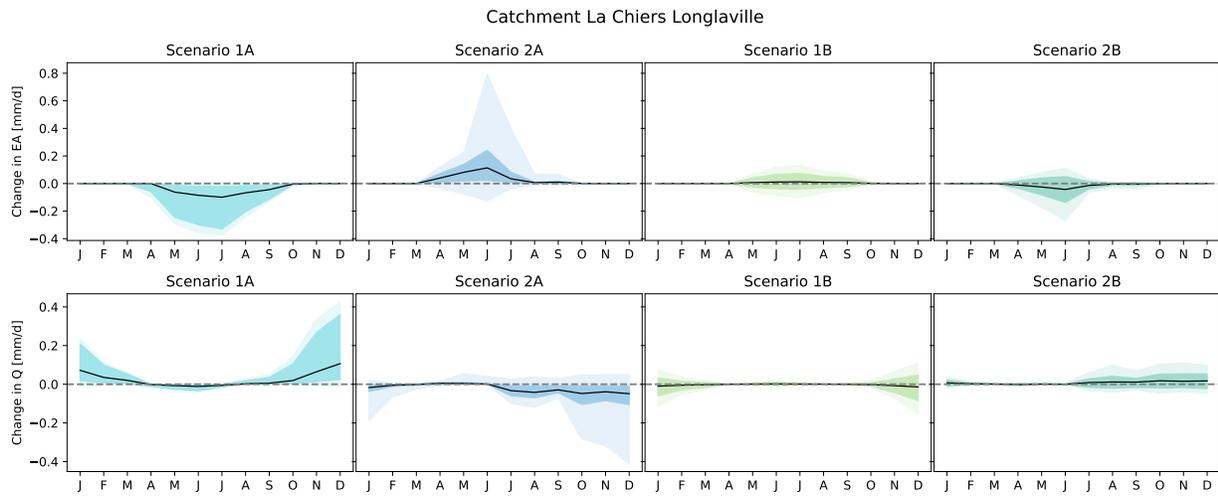
Figure 50: Change in evaporation (EA) and streamflow (Q), both in [mm/d] for La Chiers Longlaville.
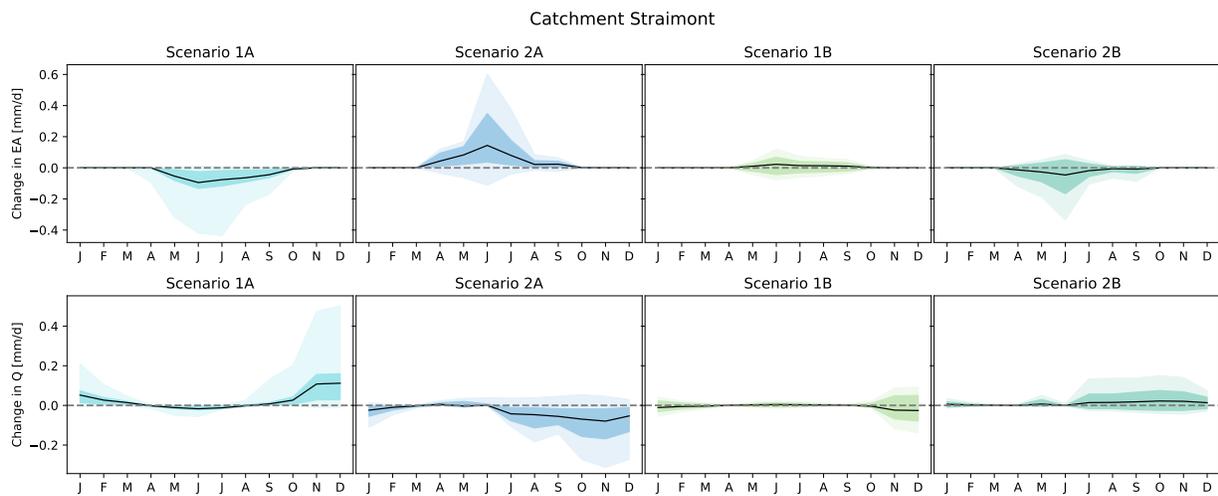
Figure 51: Change in evaporation (EA) and streamflow (Q), both in [mm/d] for Staimont.
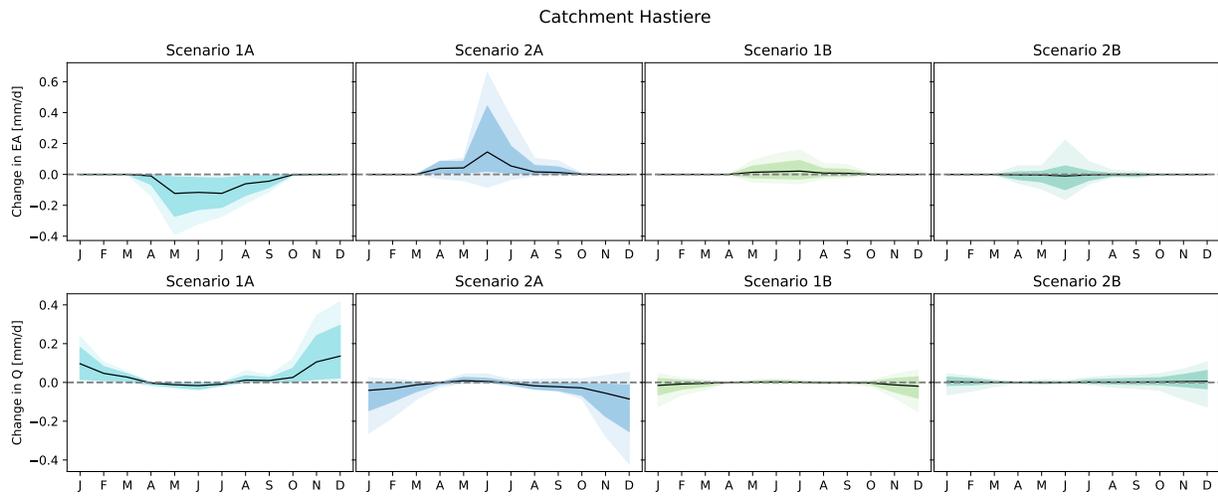
Figure 52: Change in evaporation (EA) and streamflow (Q), both in [mm/d] for Hastiere.
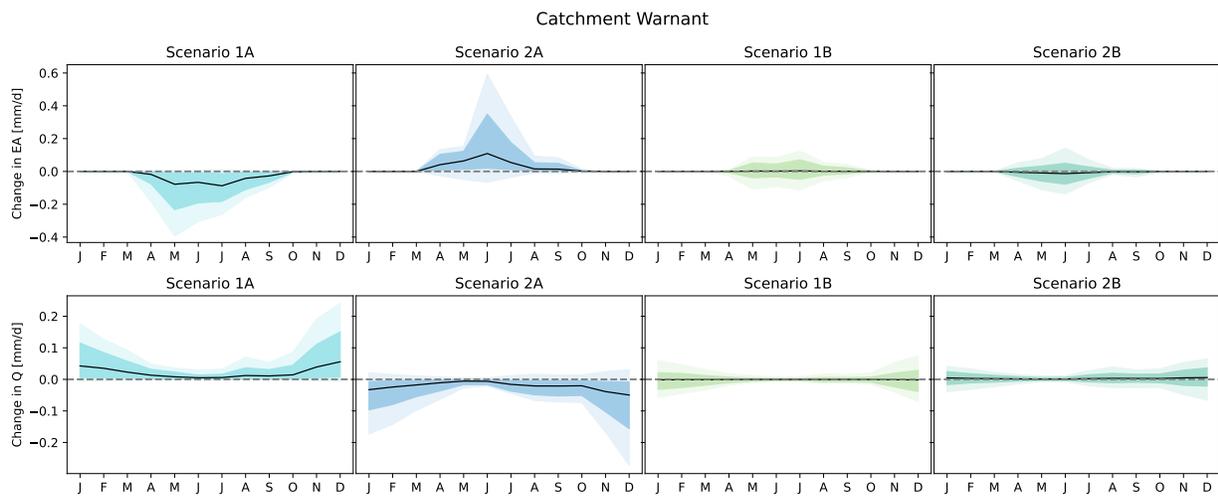
Figure 53: Change in evaporation (EA) and streamflow (Q), both in [mm/d] for Warnant.
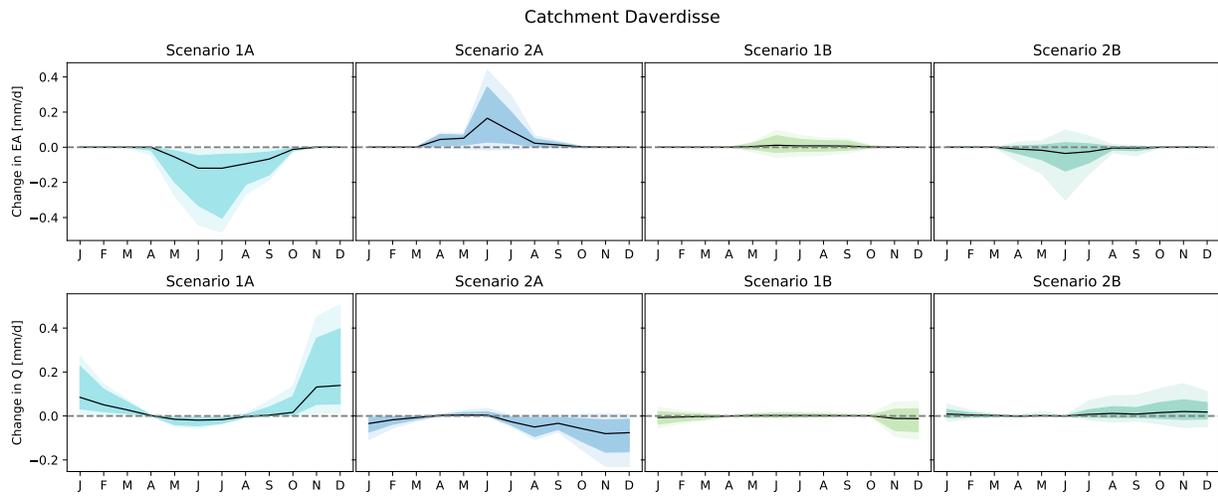
Figure 54: Change in evaporation (EA) and streamflow (Q), both in [mm/d] for Daverdisse.
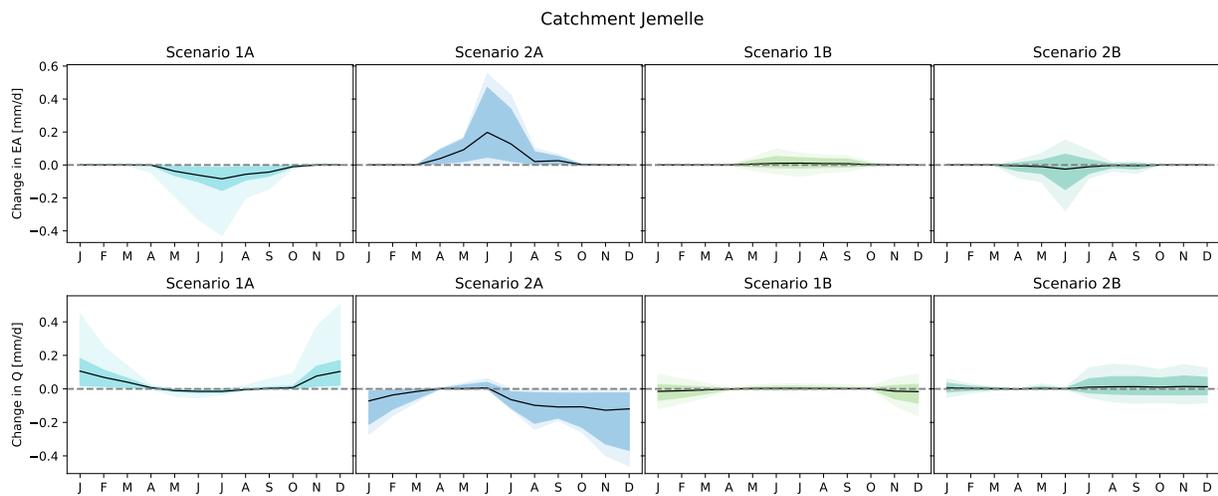
Figure 55: Change in evaporation (EA) and streamflow (Q), both in [mm/d] for Jemelle.
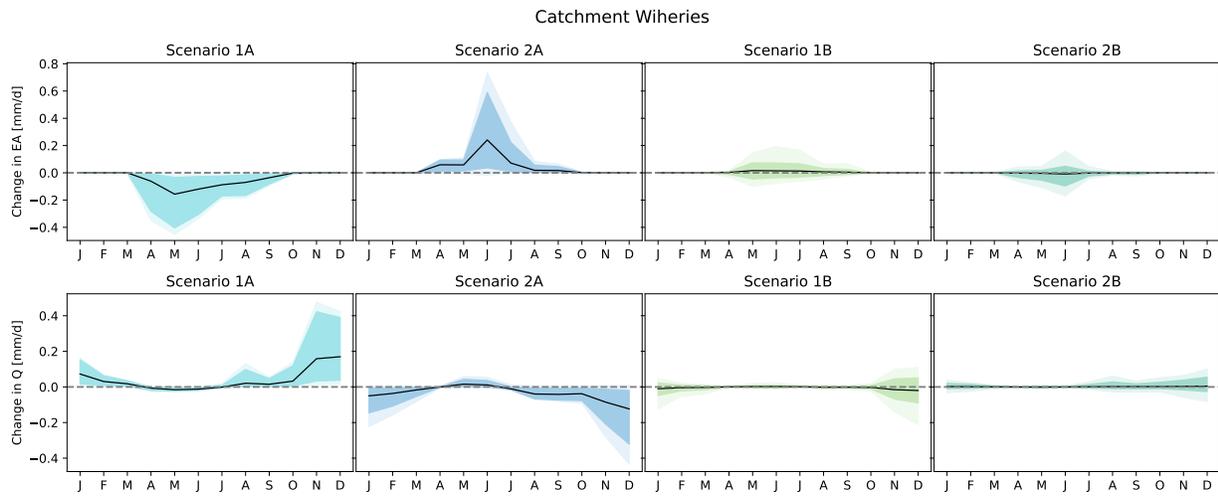
Figure 56: Change in evaporation (EA) and streamflow (Q), both in [mm/d] for Wiheries.
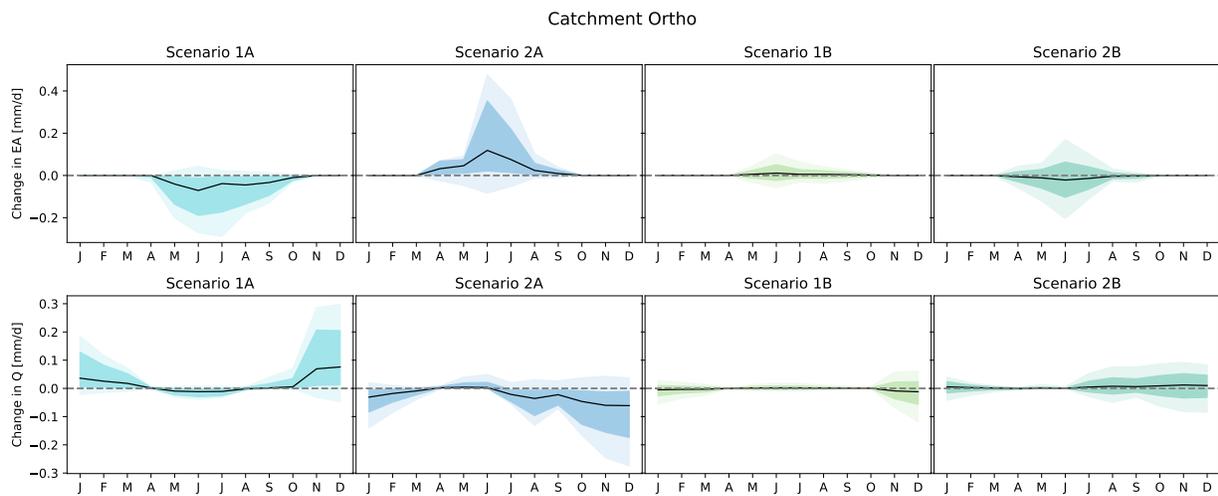
Figure 57: Change in evaporation (EA) and streamflow (Q), both in [mm/d] for Ortho.

Catchment La Meuse Goncourt
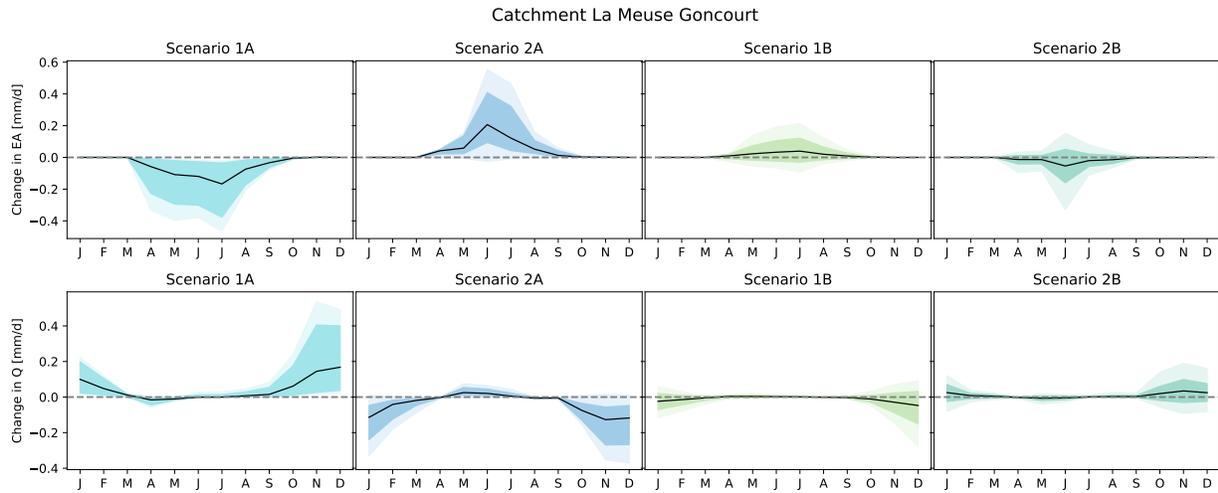
Figure 58: Change in evaporation (EA) and streamflow (Q), both in [mm/d] for La Meuse Goncourt.

Catchment Le Mouzon Circourt-sur-Mouzon [Villars]
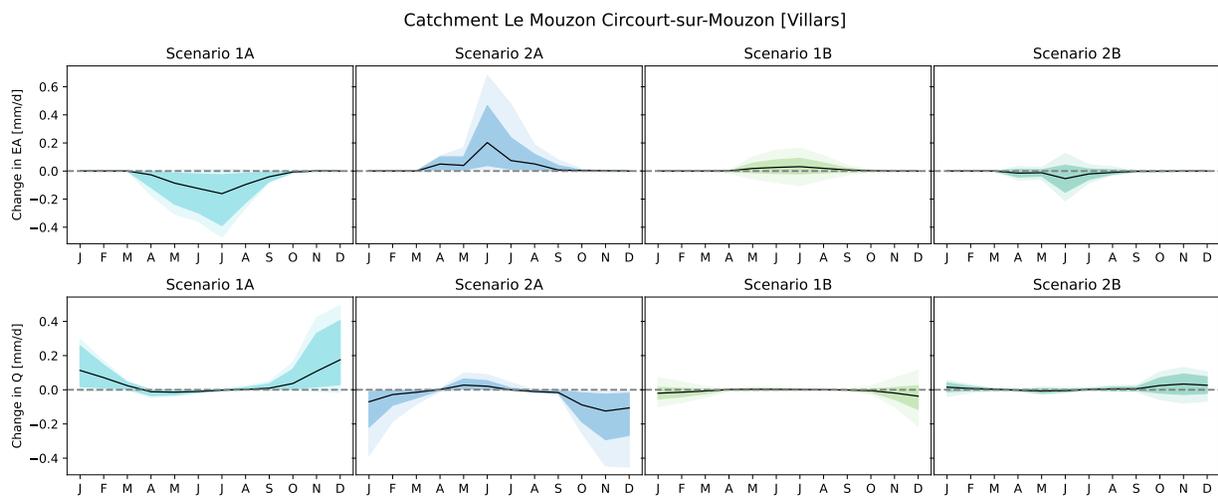
Figure 59: Change in evaporation (EA) and streamflow (Q), both in [mm/d] for La Mouzon Circourt-sur-Mouzon [Villars].
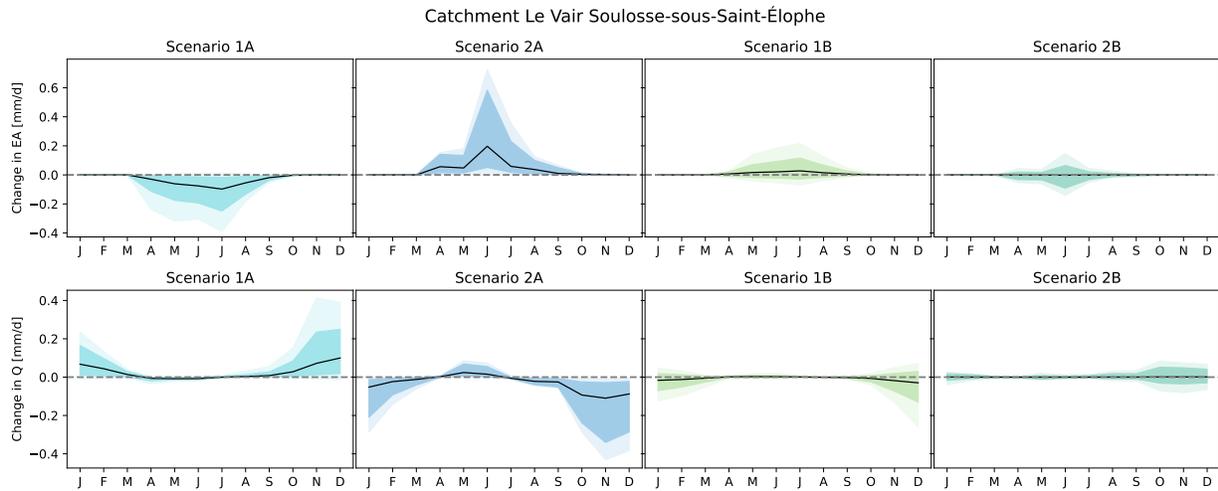
Figure 60: Change in evaporation (EA) and streamflow (Q), both in [mm/d] for Le Vair Soulosse-sous-Saint-Élophe.
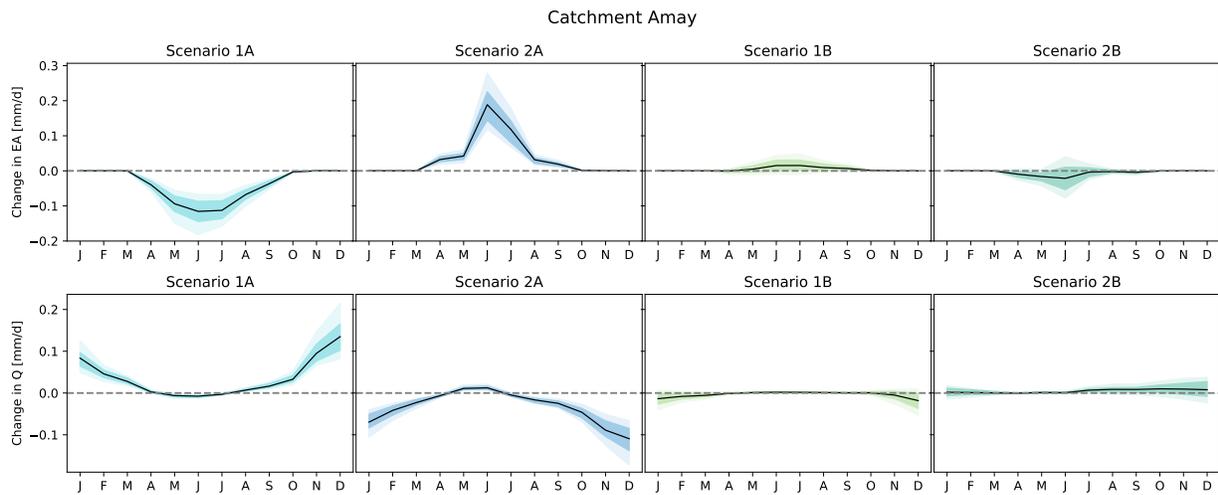
Figure 61: Change in evaporation (EA) and streamflow (Q), both in [mm/d] for Amay.
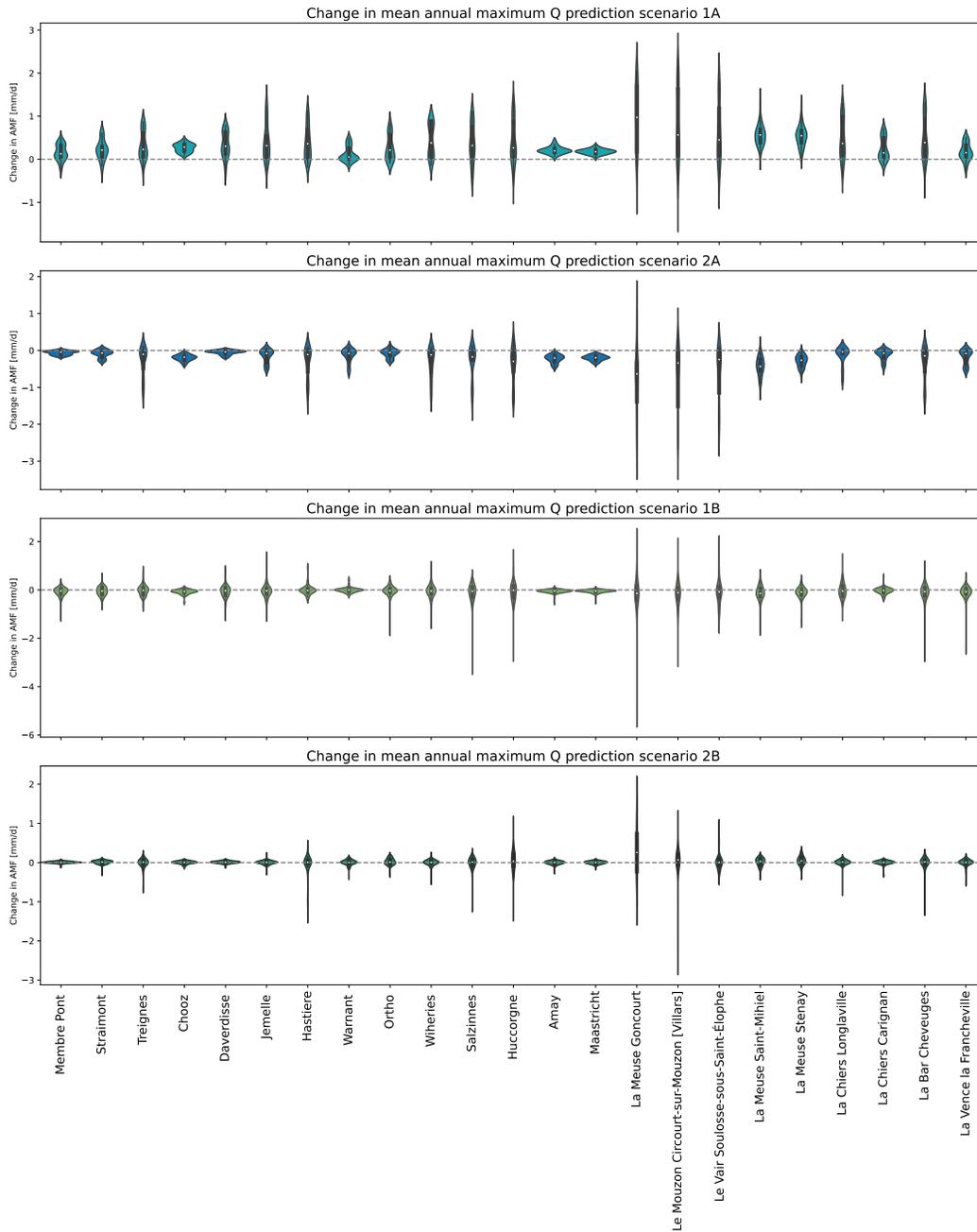
Figure 62: Change in maximum flow ($Q_{\max}$) for each catchment, compared to the reference run, where $\Delta EI = 0$.
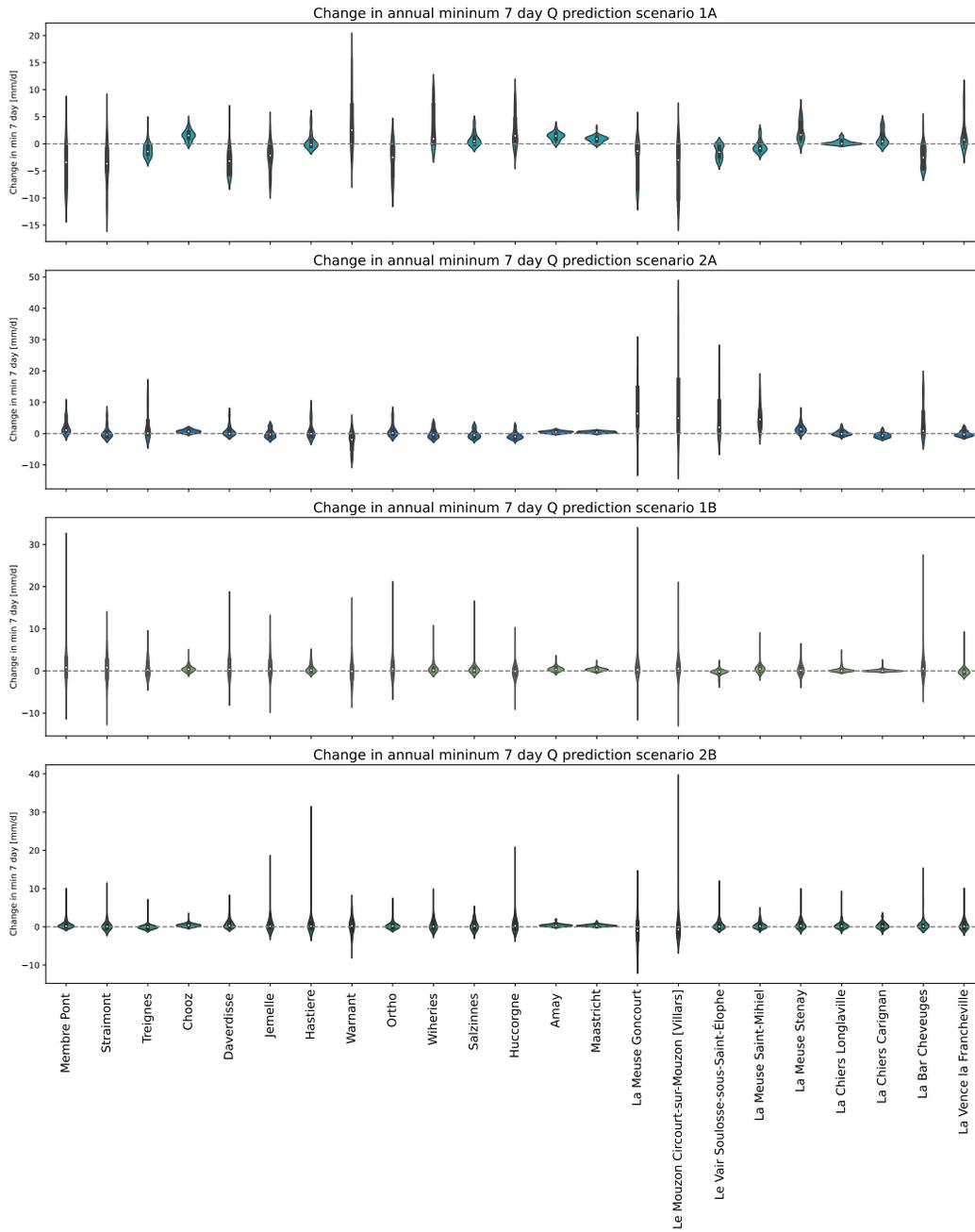
Figure 63: Change in minimum 7 day flow ($Q_{\min}$) for each catchment, compared to the reference run, where $\Delta EI = 0$.

Appendix H. Timing Maximum Flow

Table 9: Timing maximum flow (Q_{max}) for scenario 1. For every catchment the average timing of the reference run is indicated, with the standard deviation of that timing. Δt indicates the average change in timing [days] for the runs in comparison to the reference run. Also, the standard deviations are indicated [days].

Scenario 1	Reference run AMF timing	Reference run std	Δt A1	std A1	Δt B1	std B1
Membre Pont	30-11	44	+2	36	0	43
Straimont	29-11	44	+2	38	0	44
Treignes	29-11	44	+1	40	0	44
Chooz	30-11	43	+10	16	0	42
Daverdisse	29-11	44	+2	36	0	43
Jemelle	29-11	44	0	45	0	44
Hastiere	29-11	44	0	44	0	44
Warnant	30-11	44	0	44	0	44
Ortho	29-11	44	0	42	0	44
Wiheries	02-12	45	-1	43	0	45
Salzinnes	03-12	45	0	45	0	45
Huccorgne	03-12	42	0	42	0	42
Amay	02-12	44	+2	37	0	44
Maastricht	29-11	51	0	48	0	50
La Meuse Goncourt	04-12	16	0	16	0	17
Le Mouzon Circourt-sur-Mouzon [Villars]	06-12	18	-1	17	0	18
Le Vair Soulosse-sous-Saint-Élophe	06-12	18	0	18	0	18
La Meuse Saint-Mihiel	06-12	17	0	17	0	17
La Meuse Stenay	07-12	17	0	17	0	17
La Chiers Longlaville	28-11	44	0	40	0	44
La Chiers Carignan	29-11	44	0	44	0	44
La Bar Cheveuges	29-11	44	0	44	0	44
La Vence la Francheville	26-11	43	+4	33	0	43

Table 10: Timing maximum flow (Q_{max}) for scenario 2. For every catchment the average timing of the reference run is indicated, with the standard deviation of that timing. Δt indicates the average change in timing [days] for the runs in comparison to the reference run. Also, the standard deviations are indicated [days].

Scenario 2	Reference run AMF timing	Reference run std scenario 2	Δt A2	std A2	Δt B2	std B2
Membre Pont	03-12	17	0	17	0	17
Straimont	04-12	18	-1	20	-5	25
Treignes	05-12	16	0	19	0	16
Chooz	07-12	12	0	12	0	12
Daverdisse	07-12	17	0	17	0	17
Jemelle	17-11	44	+2	43	0	45
Hastiere	21-11	48	+1	48	0	48
Warnant	18-11	52	+4	49	+1	51
Ortho	16-11	43	+6	36	0	43
Wiheries	23-11	48	0	48	0	48
Salzinnes	24-11	48	+1	48	0	48
Huccorgne	30-11	42	0	46	-2	45
Amay	07-12	12	0	13	0	12
Maastricht	08-12	12	+1	13	0	12
La Meuse Goncourt	28-11	25	+1	26	0	26
Le Mouzon Circourt-sur-Mouzon [Villars]	02-12	26	0	25	-1	26
Le Vair Soulosse-sous-Saint-Élophe	29-11	25	+2	25	-1	26
La Meuse Saint-Mihiel	28-11	26	+4	25	0	27
La Meuse Stenay	04-12	25	+3	24	0	25
La Chiers Longlaville	17-11	46	+13	24	+5	36
La Chiers Carignan	14-12	12	0	12	-1	13
La Bar Cheveuges	09-12	14	+1	13	0	14
La Vence la Francheville	04-12	14	0	14	0	14

Appendix I. Precipitation trend analysis
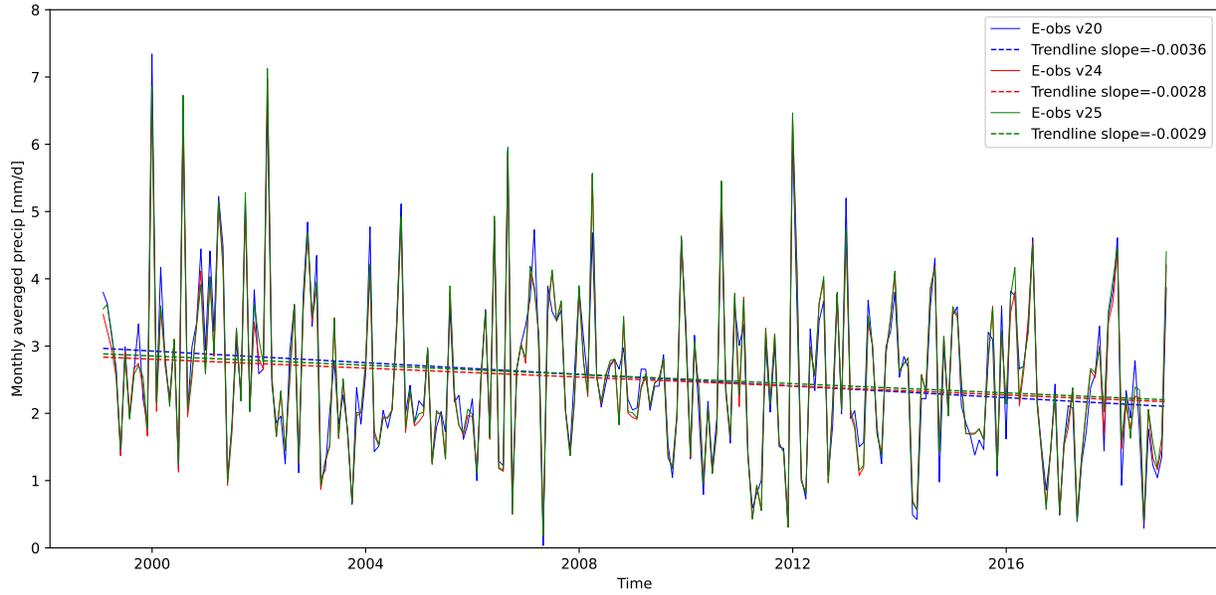
Figure 64: Trend analysis with trend lines for the model time period.
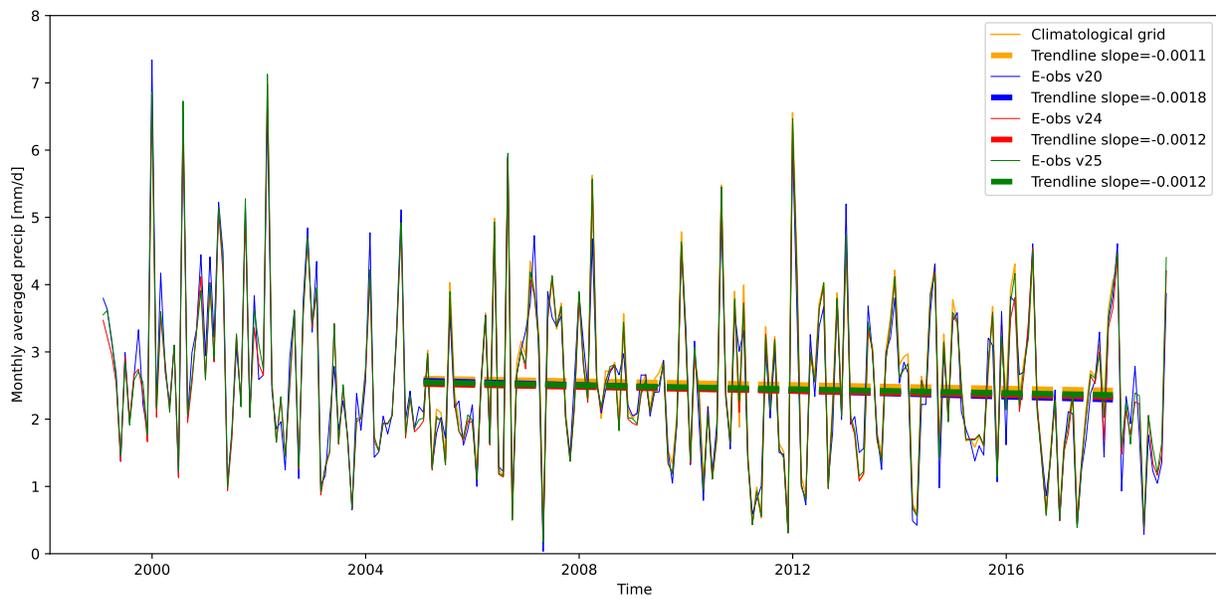
Figure 65: Trend analysis with trend lines for the timespan of the data from the climatological grid (Bouaziz et al., 2020; Service Public de Wallonie, 2018).